UNIVERSIDADE FEDERAL DE SANTA CATARINA
PROGRAMA DE PÓS-GRADUAÇÃO EM ENGENHARIA MECÂNICA

André Mateus Netto Spillere

TOWARDS OPTIMAL DESIGN OF ACOUSTIC LINERS IN TURBOFAN AERO-ENGINES

Florianópolis

2017

André Mateus Netto Spillere

TOWARDS OPTIMAL DESIGN OF ACOUSTIC LINERS IN TURBOFAN AERO-ENGINES

Dissertação submetida ao Programa de Pós-Graduação em Engenharia Mecânica da Universidade Federal de Santa Catarina para a obtenção do Grau de Mestre em Engenharia Mecânica.
Orientador: Prof. Julio Apolinário Cordioli, Dr. Eng.

Florianópolis
2017

Ficha de identificação da obra elaborada pelo autor,
através do Programa de Geração Automática da Biblioteca Universitária da UFSC.

Spillere, André Mateus Netto
Towards Optimal Design of Acoustic Liners in Turbofan Aero-Engines / André Mateus Netto Spillere ; orientador, Júlio Apolinário Cordioli, 2017.
160 p.

Dissertação (mestrado) - Universidade Federal de Santa Catarina, Centro Tecnológico, Programa de Pós Graduação em Engenharia Mecânica, Florianópolis, 2017.

Inclui referências.

1. Engenharia Mecânica. 2. Impedância acústica. 3. Liners acústicos. 4. Ruído aeronáutico. 5. Aeroacústica. I. Cordioli, Júlio Apolinário. II. Universidade Federal de Santa Catarina. Programa de Pós-Graduação em Engenharia Mecânica. III. Título.

André Mateus Netto Spillere

TOWARDS OPTIMAL DESIGN OF ACOUSTIC LINERS IN TURBOFAN AERO-ENGINES

Esta Dissertação foi julgada adequada para a obtenção do título de "Mestre em Engenharia Mecânica", e aprovada em sua forma final pelo Programa de Pós-Graduação em Engenharia Mecânica.

Florianópolis, 2 de Junho de 2017.

Prof. Jonny Carlos da Silva, Dr. Eng.
Coordenador do Curso

Banca Examinadora:

Prof. Julio Apolinário Cordioli, Dr. Eng. – Orientador
Universidade Federal de Santa Catarina, Brasil

Prof. Yves Aurégan, Ph.D.
Université du Maine, França

Prof. Andrey Ricardo da Silva, Ph.D.
Universidade Federal de Santa Catarina, Brasil

Prof. Arcanjo Lenzi, Ph.D.
Universidade Federal de Santa Catarina, Brasil

Aos meus pais e ao meu irmão.

ACKNOWLEDGEMENTS

I give special thanks to my parents, Glaucio and Maristela, for all the support and understanding of my decisions. After all, you are responsible for this work.

I am grateful to professor Julio Cordioli not only for the friendship and valuables advices, but also for the trust in my work. You made me feel confident to search and investigative independently and seek the truth when results made no sense. It has been a pleasure to learn and discuss with you, specially when accompanied by some coffee.

Thanks also to the SILENCE project team at the laboratory, Braga, Léo, Simas and Amanda, as well past team member, Augusto, Oscar and Pablo, for all the discussions and sharing of knowledge, and to the team at Embraer, Danillo and Lobão, for all the rich technical discussions.

I would like to thank my friends at the laboratory, Zargos (special thanks for the manuscript revision!), Eduardo, Loch, Zé Pedro, Murta, Gil, Lobato, Sérgio and Bonomo for the memorable moments over the past two years, like the ping-pong matches, coffees and "cuca" days.

Thanks to Embraer and FAPESC for the financial support.

Finally, a special and sincere thanks to Fernanda for comprehending my absences and all the support over the past months. My days have been happier with you.

Considerate la vostra semenza: fatti non foste a viver come bruti, ma per seguir virtute e canoscenza.

(Dante Alighieri)

RESUMO

Motores *turbofan* são largamente utilizados em aeronaves comerciais e são uma das principais fontes de ruído. O ruído desse motores pode ser dividido em diferentes componentes, sendo que o ruído proveniente do *fan* é de grande importância no processo de certificação da aeronave. Este é geralmente dominado pela presença de tons e suas harmônicas, tornando desejável utilizar um tratamento acústico com grande atenuação em uma faixa estreita de frequência. Isto é obtido por meio de *liners* acústicos, que podem ser interpretados como um arranjo de ressonadores de Helmholtz. Tradicionalmente, os *liners* são caracterizados por meio de sua impedância acústica. Esta abordagem possui várias vantagens: (i) a impedância acústica pode ser estimada por modelos semi-empíricos de baixo custo; (ii) várias técnicas experimentais são reportadas na literatura para extrair a impedância do *liner*, como os métodos inversos, diretos e técnicas *in situ*; (iii) o conceito de impedância ótima para dutos pode ser desenvolvida, e portanto o *liner* pode ser projetado para alcançar a impedância ótima; (iv) a previsão de atenuação sonora em dutos é baseada na impedância acústica do *liner*. Estes quatro itens são abordados neste trabalho. Primeiramente, modelos semi-empíricos preditivos de *liner* são analisados e comparados com resultados experimentais. Os modelos são baseados na soma de diversos efeitos e dão uma ideia de quais afetam a impedância acústica do *liner*. Na sequência, técnicas experimentais são investigadas. O método clássico de acoplamento modal é modificado para incluir um modelo de impedância, resultando em curvas contínuas. Além disso, efeitos de condição de contorno na edução de impedância são considerados, e alternativas à condição de contorno de Ingard-Myers são implementadas. A diferença entre resultados na impedância quando a fonte sonora está a montante ou a jusante da amostra também é discutida. Em seguida, o conceito de impedância ótima para dutos circulares na ausência e presença de escoamento uniforme é apresentado, assim como aplicações para geometria de motores aeronáuticos *turbofan*. Finalmente, a previsão de atenuação sonora baseada em escoamento uniforme e cisalhante é comparada.

Palavras-chave: Impedância acústica; *Liners* Acústicos; Ruído Aeronáutico; Aeroacústica.

UM ESTUDO DA OTIMIZAÇÃO DE LINERS ACÚSTICOS EM MOTORES TURBOFAN AERONÁUTICOS

Introdução

Motores *turbofan* aeronáuticos encontraram grande aceitação na aviação civil na década de 60. Devido às modificações em sua geometria e funcionamento ao longo dos anos, o ruído gerado pelo *fan* se tornou uma das principais fontes de ruído aeronáutico. A métrica *Effective Perceived Noise Level* (EPNL), criada para melhor representar o incômodo das pessoas ao ruído e utilizada para certificação de aeronaves, é rigorosa quanto à presença de tons. Portanto, materiais de tratamento acústico para motores aeronáuticos, chamados de *liners* acústicos, têm recebido grande atenção. Suas propriedades acústicas variam com as condições de voo e sua geometria, e consequentemente a atenuação sonora proporcionada.

Objetivos

Este trabalho tem como objetivo geral desenvolver e/ou aprimorar as ferramentas de projeto de *liners* acústicos. Para alcançar este objetivo, propõe-se: (i) investigar modelos preditivos e técnicas experimentais que correlacionem a geometria do *liner* e condições de operação com sua respectiva impedância acústica, (ii) desenvolver o equacionamento de impedância ótima para dutos circulares na presença de escoamento e (iii) implementar uma formulação analítica de predição da atenuação sonora com base na impedância do *liner*, geometria do duto e espessura de camada limite.

Modelos Preditivos

Os modelos preditivos de impedância acústica de *liners* são baseados na soma de diversos efeitos. Tradicionalmente, as impedâncias de viscosidade/massa, radiação e cavidade são derivadas analiticamente, enquanto efeitos não lineares são ajustados empiricamente. É possível observar uma grande diferença de impedância entre os modelos, bem como no comparativos com resultados experimentais obtidos no LVA/UFSC. Observa-se que os termos não lineares, relacionados a efeitos de escoamento e alto nível de pressão sonora, são dominantes nas condições de voo, e por isso devem ser melhor investigados.

Técnicas Experimentais

A medição da impedância acústica de *liners* não é uma tarefa trivial, já que as condições de voo devem ser reproduzidas. O LVA/UFSC conta com uma bancada experimental onde uma amostra de *liner* é sujeita a escoamento tangencial. Duas técnicas de edução de impedância propostas na literatura são investigadas. A técnica de acoplamento modal é baseada na minimização de uma função custo dada pela diferença entre pressão acústica medida na bancada e modelada por meio de uma formulação analítica de acústica de dutos na presença de escoamento e impedância de parede. Outra técnica é o método direto baseado no método Prony, de tal forma que nenhuma rotina de otimização é necessária, restando apenas a modelagem do campo acústico.

Primeiramente, problemas relacionados a medição, como por exemplo baixa relação sinal-ruído na bancada, são investigados, e uma abordagem alternativa para solução deste problema é proposta. Tradicionalmente, a edução da impedância é feita para cada frequência individualmente, de tal forma que frequências com baixa relação sinal-ruído não retornam valores de impedância físicos. Desta forma, um modelo de impedância é incorporado ao procedimento, resultando em uma curva contínua de impedância na frequência.

Na sequência, diferentes hipóteses relacionadas a condições de contorno na modelagem do campo acústico são investigadas. Em especial, as condições de contorno de Ingard/Myers e Brambley, relacionadas a escoamento uniforme, são analisadas para o método de acoplamento modal. Para o método direto, é possível incluir uma solução exata do perfil de velocidade por meio da equação de Pridmore-Brown. Observa-se que a edução de impedância é afetada pelas condições de contorno consideradas. Todavia, diferenças no resultado de impedância quando a onda acústica se propaga a montante ou a jusante do escoamento continuam presentes.

Impedância Ótima

A impedância ótima é definida com a impedância que proporciona o maior decaimento modal em um duto. As expressões de impedância ótima para dutos retangulares, presença de escoamento e modos de alta ordem são conhecidas, porém não são válidas para dutos circulares, e consequentemente para motores aeronáuticos. Portanto, estas expressões são desenvolvidas na presença de escoamento uniforme, e uma análise gráfica demonstra o comportamento do número de onda axial no plano complexo na presença de uma parede de impedância ótima.

Predição da Atenuação Sonora

A estimativa da atenuação sonora proporcionada pelo *liner* é a etapa final deste trabalho. Com base na equação de Pridmore-Brown, investiga-se os efeitos de velocidade de escoamento e espessura de camada limite em geometrias genéricas e típicas de motores *turbofan*. Ênfase é dada para atenuação de modos de alta ordem por serem as componentes dominantes do ruído de *fan* na condição de decolagem. Demonstra-se que a espessura de camada limite é de grande importância na correta predição da atenuação sonora, tal que a impedância ótima é modificada.

Conclusões

Todas as ferramentas de projeto de *liners* desenvolvidas neste trabalho possuem suas limitações que devem ser posteriormente investigadas. Os modelos preditivos ainda necessitam de aperfeiçoamento para que se aproximem dos resultados experimentais, principalmente em relação aos termos não lineares. A precisão das técnicas experimentais é melhorada quando condições de contorno mais apropriadas são utilizadas, porém não explicam a diferença entre resultados de impedância para ondas acústicas se propagando a montante e a jusante. A expressão de impedância ótima para dutos circulares está limitada a escoamentos uniformes, porém é de grande valia como uma primeira estimativa. Por fim, o modelo analítico de atenuação sonora demonstra a importância de incluir a espessura de camada limite no projeto do *liner*. Entretanto, a análise está limitada para dutos de seção constante sem transição de impedância nem reflexão na saída do duto, condições não representativas de motores aeronáuticos.

De forma geral, este trabalho engloba as ferramentas necessárias para o projeto de um *liner* acústico. Embora cada capítulo possua suas limitações, é possível utilizar estas ferramentas para encontrar a impedância ótima para um determinado motor e condições de voo, relacionar esta impedância com a geometria do *liner* por meio de modelos preditivos e/ou experimentais, e por fim estimar a atenuação sonora esperada.

ABSTRACT

Turbofan aero-engines are largely employed in commercial aircraft and are one of the main sources of noise. Engine noise can be divided into several components, and fan noise plays a major role in the aircraft certification process. It is generally dominated by the presence of a tone and its harmonics, making desirable to use an acoustic treatment with large attenuation at a narrow bandwidth. This is accomplished by means of acoustic liners, which can be seen as an array of Helmholtz resonators. Usually, the liner is characterized by its acoustic impedance. This approach has several advantages: (i) the acoustic impedance can be predicted by low-cost semi-empirical models; (ii) many experimental techniques are reported in the literature to extract the liner impedance, such as inverse methods, straightforward methods and in situ techniques; (iii) the concept of optimal impedance for ducts can be developed, and therefore the liner can be designed to achieve the optimal impedance; (iv) the sound attenuation prediction in ducts is based on the liner acoustic impedance. These four items are covered in this work. Firstly, liner prediction semi-empirical models are analysed and compared to experimental results. The models are based on the sum of several effects and give an insight into what alters the liner acoustic impedance. On the following, the experimental techniques are investigated. The classical mode matching method is modified to include an impedance model, resulting in smooth impedance curves. Also, the effect of boundary conditions in the educed impedance is considered, and alternatives to the Ingard-Myers boundary condition are implemented. The difference between upstream and downstream acoustic source positions in the educed impedance is also discussed. Next, the concept of optimal impedance for circular ducts in the absence and presence of mean flow is presented, as well some applications to turbofan aero-engine geometries. Finally, sound attenuation predictions based on uniform and shear flow are compared.

Keywords: Acoustic Impedance; Acoustic Liners; Aircraft Noise; Aeroacoustics

LIST OF FIGURES

LIST OF TABLES

LIST OF ACRONYMS

2DOF	Double degree of freedom
BPF	Blade passage frequency
CHE	Convected Helmholtz equation
HI	Hydrodynamic instability
HS	Hydrodynamic stable
IL	Insertion loss
LDA	Laser Doppler anemometry
LEE	Linearized Euler equation
LVA	Acoustics and Vibration Laboratory
MDOF	Multiple degree of freedom
MMM	Mode matching method
PIV	Particle image velocimetry
POA	Percentage of open area
PWL	Sound power level
SDOF	Single degree of freedom
SFM	Straightforward method
SL	Left-running surface wave
SNR	Signal-to-noise ratio
SPL	Sound pressure level
SR	Right-running surface wave
TPM	Two-port method
UFSC	Federal University of Santa Catarina

LIST OF SYMBOLS

Latin Symbols

(mn)	Mode index	
(q)	Mode index (impedance eduction)	
(r, ϕ, z)	Cylindrical coordinate system	
(x, y, z)	Cartesian coordinate system	
$\bar{P}$	Root-mean-squared acoustic pressure	Pa
$\mathbf{r}$	Rational function parameters	
$\mathbf{x}$	Impedance model parameters	
$\tilde{C}$	Complex parameter (Multipole model)	
A	Modal amplitude	Pa
a	Duct radius	m
B	Number of fan blades	
b	Duct width	m
C	Cost function	
c	Speed of sound	$\mathrm{m\,s^{-1}}$
C_D	Discharge coefficient	
$C_{1,2}$	Real positive coefficients (Multipole model)	
d	Hole diameter	m
E	Mean axial acoustic energy	J
f	Frequency	Hz
f_{int}	Interaction factor between holes	
f_c	Cut-on frequency	Hz
h	Duct height	m

i	Imaginary unit $\sqrt{-1}$	
J	Total number of microphones	
j	Microphone index	
J_m	m-th order Bessel function of first kind	
K	Optimal impedance constant	
k	Free-field wave number	m^{-1}
k_r	Radial wave number	m^{-1}
K_s	Stokes wave number	m^{-1}
k_x	Transverse wave number in x-direction	m^{-1}
k_y	Transverse wave number in y-direction	m^{-1}
k_z	Axial wave number	m^{-1}
L	Liner length	m
l	Cavity depth	m
L_d	Aero-engine duct length	
L_p	Sound pressure level	dB
L_W	Sound power level	dB
M	Mach number	
m	Mass reactance (EHR model)	s
M_{avg}	Average Mach number	
M_{max}	Maximum Mach number	
M_a	Acoustic particle velocity Mach number	
p	Acoustic pressure	Pa
Q	Total number of modes (impedance eduction)	
R	Face-sheet resistance (EHR model)	
R_e	Exit reflection coefficient	

s	Spacing between holes	m
t	Time	s
T_l	Cavity response time (EHR model)	s
U	Flow velocity	$\mathrm{m\,s^{-1}}$
u	Acoustic particle velocity	$\mathrm{m\,s^{-1}}$
U_*	Friction velocity	$\mathrm{m\,s^{-1}}$
U_{avg}	Average flow velocity	
U_{max}	Maximum flow velocity	
u_z	Axial acoustic particle velocity	$\mathrm{m\,s^{-1}}$
v	Turbulent velocity fluctuation	$\mathrm{m\,s^{-1}}$
Z	Liner impedance	$\mathrm{Pa\,s\,m^{-3}}$
Z_{eff}	Effective impedance	$\mathrm{Pa\,s\,m^{-3}}$
Z_{opt}	Normalized optimal impedance	

Greek Symbols

α	Dimensionless radial wave number	
β	Prandtl-Glauert factor $\sqrt{1-M^2}$	
β_c	Cavity reactance (EHR model)	
χ	Reactance	
$\delta I_{0,1}$	Brambley coefficients	m
Δz	Distance between consecutive microphones	
δ	Boundary layer thickness	m
δ_e	Orifice end correction	m
δ_e^*	Modified orifice end correction	m
ϵ_χ	Hole end correction (reactance)	m
ϵ_θ	Hole end correction (resistance)	m

γ	Scaled radial wave number	
κ	Dimensionless axial wave number	
λ	Wavelength	m
μ	Dynamic viscosity	$\mathrm{Pa\,s}$
ν	Kinematic viscosity	$\mathrm{m^2\,s^{-1}}$
Ω	Scaled free-field wave number	
ω	Angular frequency	$\mathrm{rad\,s^{-1}}$
ψ	Mode shape	
ρ	Air density	$\mathrm{kg\,m^{-3}}$
σ	Percentage of open area	
τ	Plate thickness	m
τ_w	Wall shear stress	Pa
θ	Resistance	
$\tilde{\xi}$	Complex parameter (Multipole model)	
υ	Auxiliary radial mode index	
ε	Damping in the cavity (EHR model)	
φ	Reduced wave number	
ϖ	Helmholtz number	
ζ	Axial wave number (straightforward method)	

Other Symbols

$\Im$	Imaginary part
∇^2	Laplace operator
$\Re$	Real part

CONTENTS

1 INTRODUCTION

The 1960s represents a milestone in history of civil aviation. The successful introduction of turbojet and low-bypass ratio turbofan aero-engines[1] in commercial aircraft boosted passenger and cargo transport. More powerful engines, greater number of flights and rise of communities around airports led to a problem previously ignored by authorities: the excessive aircraft noise. In answer to the negative public reaction, the authorities developed the concept of aircraft certification, which was implemented in the early 1970s.

In order to be certificated, the aircraft had to meet safety and noise requirements. The latter required a metric able to express human response to aircraft noise. Therefore, the Effective Perceived Noise Level (EPNL) metric was created to correct noise measurements by taking into account spectral content, presence of tones and duration of noise, leading to a more representative perception of annoyance by people [1]. Measurements had to be performed at specific locations close to the runaway [2], which can be seen in Figure 1.1: below the take-off and approach routes, and in a sideline parallel to the runaway (when the aircraft reaches maximum engine power).

The main source of noise in the first aero-engines was the exhaust jet noise. The development of engines with higher bypass ratio reduced the jet flow velocity, and consequently the jet noise. In order to keep same thrust, the duct radius was increased, and so was fan size. Therefore, fan noise became one of the predominant sources of noise in modern aero-engines. Figure 1.2 illustrates the contribution of each noise source in low- and high-bypass ratio aero-engines. Of course, the relative contribution may vary depending on aircraft condition (full-power, cutback or approach). In the next years, ultra-high-bypass engines are expected to be the norm in civil aviation [3], justifying further studies on fan noise reduction.

The main characteristic of fan noise is the presence of a fundamental tone, related to the blade passing frequency (BPF), and its harmonics [4]. Since the presence of tones is penalized in the EPNL calculation, the solution adopted by the manufacturers was to include a passive noise control treatment at the internal walls of the engine duct, according to Figure 1.3. This acoustic treatment panel, known as acoustic liner, is the main subject of study in this work.

[1] Bypass ratio is the ratio between mass flow through the bypass and engine core in a turbofan aero-engine. See Figure 1.3 for more details.

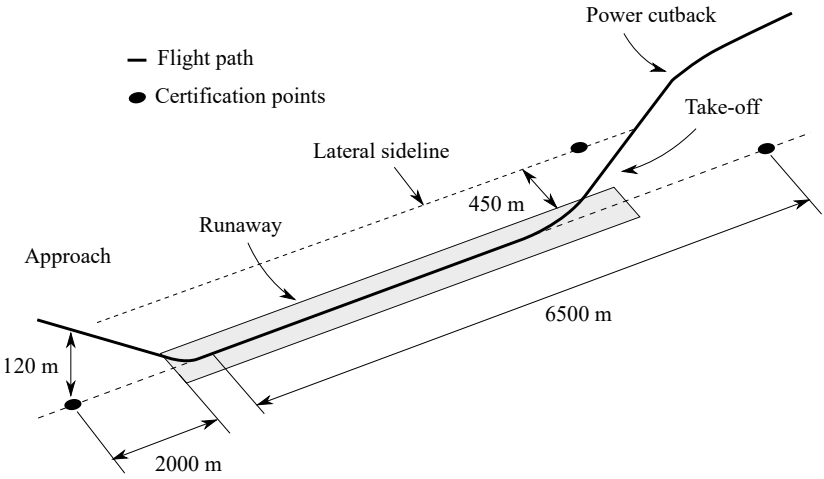

Figure 1.1 – Effective Perceived Noise Level (EPNL) certification points: below the take-off and approach routes, and in a sideline parallel to the runaway (not to scale).

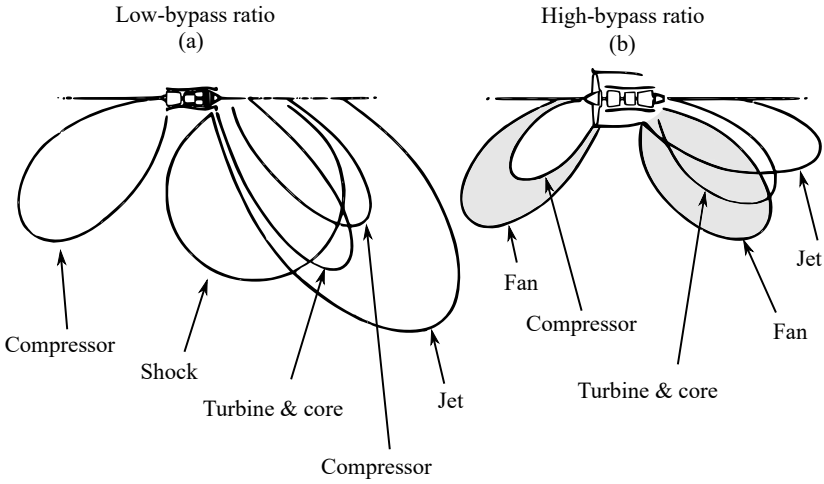

Figure 1.2 – Comparison between the main sources of noise in turbofan aero-engines with (a) low-bypass ratio, typical in the 1960s, and (b) modern aero-engines with high-bypass ratio. Adapted from Smith [1].

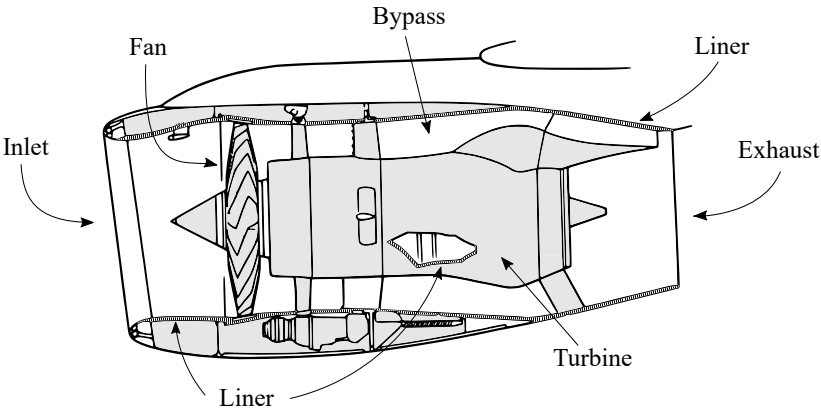

Figure 1.3 – Schematic view of a high-bypass turbofan aero-engine. Stripes represent the nacelle internal walls where acoustic liners are placed.

The liner is usually composed of three layers: (i) a perforated plate exposed to grazing flow, (ii) an intermediate structure in the form of honeycomb, and (iii) a backing rigid wall, as illustrated in Figure 1.4. This conception can be viewed as an array of Helmholtz resonators, where the holes and honeycomb cells represent the resonator neck and cavity, respectively. It is also commonly known as a single degree of freedom (SDOF) acoustic liner, since air oscillating at the neck acts as a mass, and air in the cavity acts as a spring. Therefore, its main characteristic is high acoustic attenuation over a narrow frequency bandwidth [5, 6]. The key idea is to match the frequency of maximum attenuation to the fan noise fundamental tone (which is usually the most energetic tone). Alternative conceptions are also possible and depend on the desired attenuation characteristics. A list of them is given is Chapter 2.

The project of new liners and the prediction of the liner efficacy remains a challenging task. For instance, liner performance is affected by operating conditions, namely grazing flow velocity and high sound pressure level (SPL). The usual approach is to characterize the liner by means of its acoustic impedance, which can be a function of liner geometry [7], air temperature [8], grazing flow velocity [6, 9–13], boundary layer thickness [14] and high SPL [15–17]. Consequently, frequency and level of maximum attenuation are modified. Although passive liners have a fixed geometrical arrangement, flow velocity and SPL vary

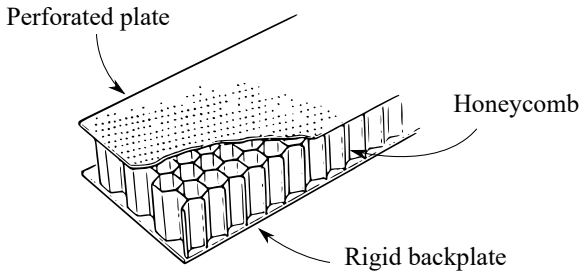

Figure 1.4 – Most common type of perforated plate liners

during take-off and approach, and hence different acoustic impedances must be taken into account in the project of an acoustic liner. Finally, wave propagation is affected by the presence of flow, and so it is the liner attenuation inside the engine duct and the fan far-field noise.

Ideally, tools for the project of acoustic liners consist of: (i) predictive models for liner acoustic impedance based on liner geometry and operating conditions (ii) experimental techniques for the characterization of liner samples, and (iii) sound attenuation modelling approaches. The first two are complementary tools to translate liner geometry into acoustic impedance. Sound attenuation may benefit from optimal impedance theory i.e. the impedance that gives the maximum in-duct attenuation. Most of these approaches share the same inputs, such as flow velocity, wave frequency and duct geometry. The project as a whole is regarded as an iterative process.

Each of these steps are far from a definitive modelling approach. There is a great discrepancy between predictive models, specially at typical flight conditions. Also, experimental techniques show different results depending on measurement conditions and method employed. Finally, sound attenuation modelling may be limited to its main assumptions, for instance infinite straight lined ducts.

In this work, each tool is further investigated and/or improved. Therefore, the outcome of this work is the development of tools for design optimization rather than a final liner design itself. Of course, this is part of the whole aero-engine design. Other analytical, numerical and experimental tools involve far-field noise propagation and fan noise generation. However, it is outside the scope of this work to investigate such techniques.

1.1 Aim and Objectives

The aim of this work is to investigate and improve low-cost analytical tools and experimental techniques in order to predict the efficacy of acoustic liners in turbofan aero-engines. This work has also immediate application to lined ducts in the presence of flow, for example in ventilation systems and automotive industry.

In order to achieve that, the following objectives are defined:

- Investigate the accuracy of semi-empirical models for impedance prediction available in the literature by comparing them with experimental results;
- Improve experimental procedures in order to obtain a more reliable acoustic impedance of liner samples;
- Extend the concept of optimal impedance in circular ducts in the presence of mean flow;
- Implement an analytical formulation of sound attenuation prediction for a given liner impedance, engine geometry and operating conditions.

1.2 Document structure

This document can be divided in two parts. The first is dedicated to predictive tools and experimental procedures regarding liner impedance. In other words, it relates physical parameters of the liner to its impedance by means of semi-empirical models and impedance eduction techniques. Both approaches are interrelated: experimental results are input to semi-empirical models. Thus, the key idea of this part is to predict/measure liner impedance when exposed to grazing flow.

The second part is related to in-duct acoustic propagation. The main input is liner impedance, which shows the importance of the previous part. The theory of optimal impedance for circular ducts in the absence of flow is well-known, so it is extended to the presence of flow. Then, sound attenuation prediction in a circular duct for a given liner length is investigated. Of special interest are boundary layer effects, so both uniform and shear flows are analysed. Different boundary layer thickness and liner impedances are also considered. Overall, this document is organized as follows.

Chapter 2 provides a literature review. First, further details are given about acoustic liners regarding geometry and design, acoustic characterization and test samples available at the Laboratory of Acoustics and Vibration (LVA/UFSC). On the following, the basic equations of duct acoustics are reviewed. This is important for two reasons: (i) the impedance eduction techniques available at LVA are based on the acoustics of rectangular ducts and (ii) the concept of optimal impedance for aero-engines and sound attenuation prediction are based on the acoustics of circular ducts. Finally, a brief explanation is given about the impedance eduction techniques.

Chapter 3 investigates predictive models for liner impedance. A total of four semi-empirical models based on typical perforated plate liners are examined in detail. Other predictive models are also briefly discussed regarding their limitations to the present work. The inputs to these models are: (i) air properties, (ii) liner geometry and (iii) operating conditions. In order to assess their accuracy, the predicted impedance is compared to experimental results of two different test samples available at LVA.

Chapter 4 analyses the current experimental procedures. Different impedance eduction techniques are discussed and implemented at the LVA/UFSC test rig. An alternative impedance eduction method based on an impedance model is proposed. Three models with different mathematical formulation are considered and included in one of the impedance eduction methods. Another area of concern is the different educed impedances when acoustic waves are propagating upstream or downstream. Different boundary conditions are investigated in order to better represent the acoustic field in the test rig, leading to different impedance results.

Chapter 5 is dedicated to the concept of optimal impedance applied to circular ducts. The aim of this chapter is to include the effects of uniform flow on the optimal impedance. This has been previously investigated for rectangular ducts, but an expression for circular ducts is not known by the author. Then, examples of optimal impedance for aero-engines are given.

Chapter 6 investigates sound attenuation prediction, specially in the presence of shear flow. Details about the numerical implementation based on the Pridmore-Brown equation are given. On the following, effects of flow velocity and boundary layer thickness are investigated for an arbitrary duct geometry and an example of application to a typical turbofan aero-engine is given, with emphasis on sideline and cutback conditions.

2 LITERATURE REVIEW

This chapter starts with a description of typical acoustic liners used in aeronautical applications, which provides a basic understanding for the semi-empirical models that will be presented in Chapter 3. Then, a review of duct acoustics in the presence of flow and a lined surface is given. This is important for two reasons: (i) it provides the basic equations for the impedance eduction techniques (explored in greater detail in Chapter 4) and (ii) it is also valid for in-duct propagation of fan noise in aero-engines, from which the concept of optimal impedance can be derived (Chapter 5), as well the sound attenuation prediction for a given liner impedance and flow characteristics (Chapter 6).

2.1 Acoustic liners

Acoustic liners are used as aero-engine noise treatments placed at the nacelle internal walls. Traditionally, acoustic liners have a fixed geometrical arrangement and are considered a passive acoustic treatment. More recently, novel concepts led to the development of active control systems in acoustic liners by using moveable parts or bias flow[1], for example [18, 19]. However, such concepts of liner are outside the scope of this work.

It is convenient to view acoustic liners as an array of Helmholtz resonators. A single cell is sketched in Figure 2.1 and the geometry is chosen to achieve the desired acoustic performance. The main parameters are hole diameter d, plate thickness τ and cavity depth l. Although not sketched, commonly more than one hole is present at each honeycomb cell, so the percentage of open area σ of the perforated plate is also considered a geometrical parameter.

Liner performance can be accounted by means of insertion loss or transmission and reflection coefficients, which are dependent on the duct geometry and treated area. Therefore, the usual approach is to characterize acoustic liners by its acoustic impedance, defined as the ratio between acoustic pressure p and acoustic particle velocity u,

$$Z(\omega) = \frac{p(\omega)}{u(\omega)} = \theta + i\chi. \tag{2.1}$$

[1] Differently from the grazing flow, which is parallel to the liner surface, bias flow is the flow through the perforates.

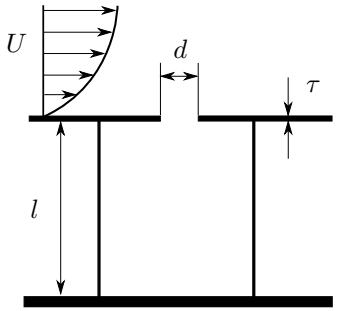

Figure 2.1 – Sketch of a single Helmholtz resonator. The main geometrical parameters are the hole diameter d, the plate thickness τ, the cavity depth l. The perforated plate is subject to a grazing flow and incident acoustic waves.

The acoustic impedance is a complex number and can be separated into real part θ, named resistance and related to energy dissipation at the perforated plate, and imaginary part χ, named reactance and related to inertia effects in the cavity. This approach has several advantages:

- the acoustic impedance can be predicted by low-cost predictive models based on geometry and operating conditions;
- many experimental techniques are reported in the literature to measure liner acoustic impedance, such as inverse and direct methods and in situ techniques;
- the liner can be designed to achieve the optimal impedance in circular and rectangular ducts;
- in-duct sound attenuation prediction is function of the wall impedance;

As it will be seen the acoustic impedance also depends on the acoustic wave frequency ω, as well on the liner geometry [7], temperature [8], grazing flow velocity [6, 9–13], boundary layer thickness [14] and high sound pressure level (SPL) [15–17]. This led to the development of predictive models, often called semi-empirical models, so that once the operating conditions and liner geometry are known, the acoustic impedance can be estimated. In reality, these models are not entirely predictive because some coefficients need to be adjusted based on experimental results. This is further discussed in Chapter 3.

2.1.1 Liner designs

Different liner designs result in different attenuation characteristics. On the following, some of the most common designs are presented. A sketch of each liner design is seen in Figure 2.2.

Single degree of freedom (SDOF) acoustic liners are largely employed in aero-engines and they are by far the most studied type of acoustic liner. Their main characteristic is the high attenuation over a narrow frequency band. The main dissipation mechanisms of SDOF acoustic liners are: (i) acoustic wave damping at the walls of the holes and (ii) one-quarter wavelength resonance at the cell [1]. If the acoustic wave is in the linear regime i.e. below approximately 130 dB, there is a laminar flow development at the hole, whereas in the non-linear regime, a turbulent jet formation can be seen, which results in an acoustic impedance sensitive to the SPL [17]. The presence of grazing flow results in a steady-state flow over the hole, which affects the in- and out-coming acoustic waves, and therefore the acoustic impedance [17]. Both high SPL and grazing flow are considered non-linear effects and have been studied since the 1970s. Experimental results have confirmed the acoustic impedance dependency on non-linear effects and they are included for instance in semi-empirical models [5, 14, 16, 20, 21].

In order to minimize non-linear effects, a wire mesh screen is bonded to the perforated plate, giving name to the so-called linear acoustic liners. The impedance is less dependent on grazing flow effects and high SPL because the mass of air in the hole is covered by the wire mesh. The resistance is also constant with frequency because of the low-Reynolds-number pressure drop for fine screens, although it shows a slight increase when the reactance is close to zero [5]. Therefore, an impedance with little variation is achieved over different engine power settings.

Two degree of freedom (2DOF) acoustic liners are an extension of SDOF by inclusion of a septum sheet, similar to a perforated plate, and an additional honeycomb structure. This concept of liner increases the frequency range of attenuation and is usually placed at the bypass [22]. As a drawback, the maximum attenuation is reduced. It is also classified as a linear liner because the septum sheet is free of non-linear effects, even though the perforated plate without wire mesh is exposed to grazing flow and high SPL. However, at high Mach numbers and SPL, the impedance may be affected, leading to a non-linear behaviour. Finally, an extension of this concept is the multiple degree of freedom (MDOF) acoustic liners, where several septum sheets and

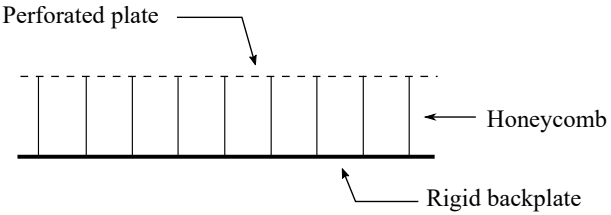

(a) Single degree of freedom (SDOF)

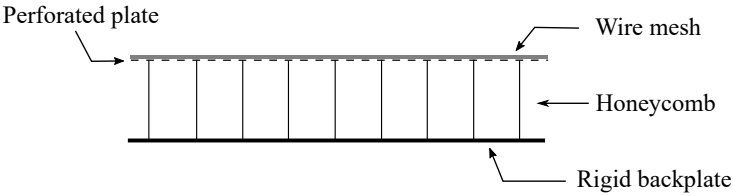

(b) Linear liner

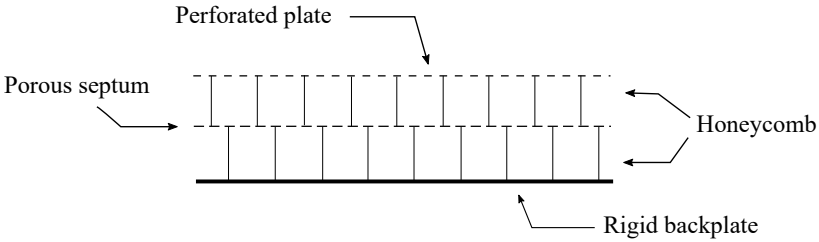

(c) Double degree of freedom (2DOF)

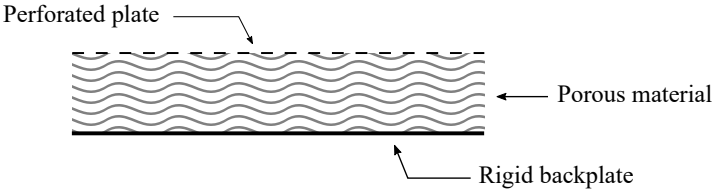

(d) Bulk absorber

Figure 2.2 – Conventional liner designs used in turbofan aero-engines.

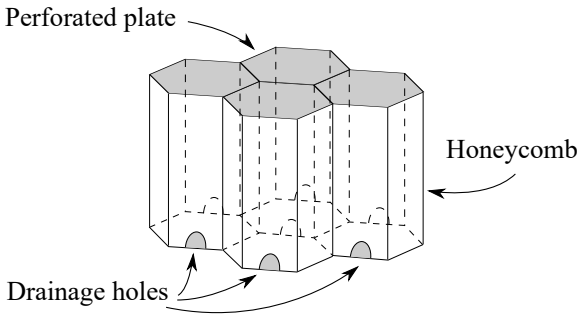

Figure 2.3 – Drainage holes located at the bottom of honeycomb cells. The liner becomes non-locally reacting due to axial wave propagation inside the honeycomb structure.

honeycomb structures are used in order to achieve the desired attenuation characteristics. However, due to space restrictions in the nacelle, this conception is seldom used in commercial aircraft.

Bulk absorbers make no use of honeycomb cells. Instead, a porous material is placed between the perforated plate and the rigid backplate. This results in a very large bandwidth of attenuation, even more than the 2DOF liner [5]. However, structural difficulties kept bulk absorber liners away from being employed in commercial aircraft.

2.1.2 Locally and non-locally reacting liners

Although subject of several studies, locally reacting[2] acoustic liners are not used in the entire nacelle. In fact, part of the engine treatment is composed by non-locally reacting acoustic liners. This is related to the presence of drainage holes: small connections between all honeycomb cells, as seen in Figure 2.3. It has the important function of avoiding the filling of cells by water or any liquid for safety reasons [6]. Thus, the acoustic wave is free to propagate inside the liner structure, parallel to the liner surface.

The acoustic response of the liner could benefit from the presence of drainage holes, therefore some studies have been conducted on non-

[2]It is worth to mention that the definition of locally reacting here is quite ambiguous. In classical acoustics, when the material properties are independent of the acoustic wave angle of incidence, it is defined as locally reacting. In this case, however, it is defined as locally reacting due to the fact that the liner local response is dependent only upon the local pressure.

Table 2.1 – Geometrical parameters of the tested liner samples

Test sample	Liner A	Liner B
Type	SDOF	SDOF
Hole diameter d [mm]	1.0	2.0
Face-sheet thickness τ [mm]	0.65	0.80
Cavity depth l [mm]	19.0	19.0
Percentage of open area σ [%]	5.18	8.63

locally reacting acoustic liners [23–26]. The increase in complexity in analytical formulations and experimental techniques led to a reduced number of works in this area, and therefore this type of liner is not considered in this work.

2.1.3 Test samples

Throughout the following chapters, two liner samples are considered for analysis. Both are typical SDOF locally reacting liners used in turbofan aero-engines.

Liner A is provided by a commercial manufacturer, whereas liner B is an in-house built sample. The main geometrical parameters of each sample, according to Figure 2.1 are summarized in Table 2.1. The percentage of open area is defined as the ratio between the area of the holes and total face-sheet area. It also accounts for partial honeycomb blockage of the holes in the assembly process.

2.2 Duct acoustics

This section will first introduce the basic equations for the acoustic field inside a duct in the presence of a lined wall. Then, the specific set of equations for the impedance eduction techniques are presented Section 2.3.

The convected wave equation in a duct with uniform mean flow in the axial direction z is given by

$$\nabla^2 p - \frac{1}{c^2}\frac{D^2 p}{Dt^2} = 0, \tag{2.2}$$

where $p = p(x, y, z, t)$ is acoustic pressure, c is the speed of sound in the fluid, D/Dt is the material derivative and ∇^2 is the Laplace operator.

Equation 2.2 possesses infinite solutions, each one representing a mode,

$$p^{(mn)} = A^{(mn)}\psi^{(mn)}e^{-ik_z^{(mn)}z}, \tag{2.3}$$

where (mn) represents the mode index and depends on the duct geometry, $A^{(mn)}$ is the modal amplitude, $k_z^{(mn)}$ is the axial wave number and $\psi^{(mn)} = \psi(x, y)$ is the mode shape. Notice that the harmonic time dependence $e^{i\omega t}$ is omitted. Of particular interest is the imaginary part of the axial wave number, which represents the wave decay rate along the duct. This is further discussed in Chapter 6. Equation 2.3 is a general solution valid for both circular and rectangular ducts. The modal amplitude is an arbitrary constant, but the mode shapes and axial wave numbers depend on the duct geometry, and are further discussed below.

2.2.1 Circular ducts

Figure 2.4 illustrates the reference geometry for an infinite circular duct with uniform mean flow in the $z+$ direction. The general solution to Equation 2.2, considering only downstream wave propagation[3] and assuming no reflections, is given by

$$p(r, \phi, z) = \sum_{m=0}^{\infty}\sum_{n=1}^{\infty} A^{(mn)}\psi^{(mn)}e^{-ik_z^{(mn)}z}, \tag{2.4}$$

the mode shape being

$$\psi^{(mn)}(r, \phi) = J_m\left(k_r^{(mn)}r\right)\cos\left(m\phi\right), \tag{2.5}$$

where J_m is the m-th order Bessel function of first kind and k_r is the radial wave number. By convention, the azimuthal mode order starts at $m = 0$, whereas the radial mode order starts at $n = 1$. The wave numbers are related by the dispersion relation,

$$k_r^2 + k_z^2 = \left(k + Mk_z\right)^2, \tag{2.6}$$

where $k = \omega/c$ is the free-field wave number, $M = U/c$ is the mean flow Mach number and U is the mean flow velocity in the $z+$ direction.

In order to illustrate the mode shapes, the case of a rigid-walled

[3] wave propagating in the same direction of the flow

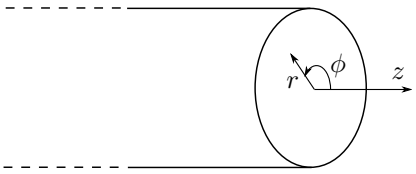

Figure 2.4 – Coordinate system for a circular duct.

circular duct of radius a and no-flow is considered. In this case, the radial acoustic particle velocity at the wall must vanish,

$$\left.\frac{\partial p}{\partial r}\right|_{r=a} = 0. \tag{2.7}$$

which reduces Equation 2.5 to

$$J'_m\left(ak_r^{(mn)}\right) = 0. \tag{2.8}$$

Notice that for each m, infinite solutions of $ak_r^{(mn)}$ are possible. Table 2.2 summarizes the first solutions to Equation 2.8. Substituting these values into Equation 2.5 gives the corresponding mode shapes, as illustrated in Figure 2.5. Although rigid-walled circular ducts are of little interest in this work, Equation 2.8 is particularly important. In the presence of a lined wall without flow, the boundary condition is given by

$$\rho\left.\frac{\partial p}{\partial r}\right|_{r=a} = -\frac{i\omega}{Z}p, \tag{2.9}$$

and yields the following eigenvalue equation,

$$\frac{J_m(ak_r^{(mn)})}{k_r^{(mn)}J'_m(ak_r^{(mn)})} = \frac{iZ}{k}. \tag{2.10}$$

A Newton-Raphson iteration scheme can be used to solve the equation. Since infinite solutions are possible, it is sensitive to initial guess[4]. The idea is to use a known and exact value of k_r, such as the solution to Equation 2.8, as initial guess. For high values of impedance,

[4]Of course Equation 2.8, if solved by means of a Newton-Raphson iteration scheme, is also sensitive to initial guess. However, it is a relatively easy task because smooth functions, such as Equation 2.8, can be expanded in Chebyshev polynomials [27], whose roots can be found, for instance, with Matlab `roots` function.

Table 2.2 – Values of $ak_r^{(mn)}$ that satisfy Equation 2.8 for each pair of modes (mn).

		m				
		0	1	2	3	4
n	1	0.000	1.841	3.054	4.201	5.318
	2	3.832	5.331	6.706	8.015	9.282
	3	7.016	8.5836	9.970	11.34	12.68

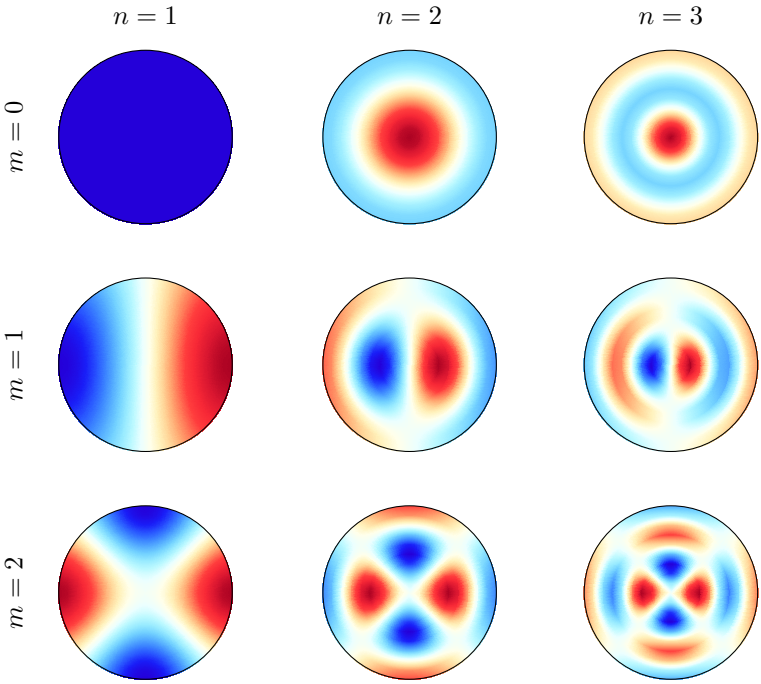

Figure 2.5 – Mode shapes $\psi^{(mn)}$ in a circular duct with rigid walls. Red regions represent positive pressure, whereas blue regions represent negative pressure.

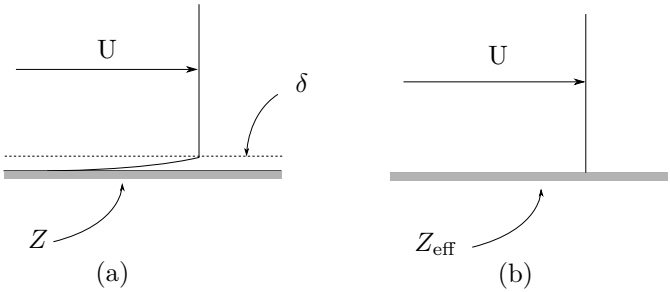

Figure 2.6 – Lined wall boundary condition representation in the presence of grazing flow. The wall impedance Z is subject to a uniform flow U. Above its surface, a boundary layer of thickness δ is present (a). Applying the Ingard-Myers boundary condition, an "effective" impedance Z_{eff} is obtained (b).

the radial wave number is close the hard-walled case. At sufficiently small values of impedance (in special the resistance), irregular modes appear, and the axial wave numbers are launched into the complex plane. These modes are called surface waves and their behaviour is further discussed in Chapters 5

In the presence of mean flow, the wall boundary condition has to be modified because the flow velocity is non-zero (slip condition). Ingard [28] assumed a vortex sheet of infinitesimal thickness and continuity of acoustic particle displacement across it, and later Myers [29] generalized it to curved surfaces, leading to the so-called Ingard-Myers boundary condition. This hypothesis is sketched in Figure 2.6. In fact, the Ingard-Myers boundary condition leads to an "effective" impedance Z_{eff} as seen by the acoustic field.

For aero-engine applications, where the boundary layer is very small compared to the duct radius, this seems to be a valid assumption. However, Gabard [30] has shown that, even for boundary layers of 1 % of the duct radius, the Ingard-Myers boundary condition may incorrectly predict the liner attenuation, specially for upstream propagating waves, which corresponds to engine intake. Nevertheless, the Ingard-Myers boundary condition, in the case of a straight circular duct[5], is given by

$$-u = \frac{1}{i\omega Z}\frac{Dp}{Dt}, \tag{2.11}$$

[5]This is also valid for a straight rectangular duct

leading to the eigenvalue equation

$$\frac{ik}{Z}\left(1-\frac{k_z^{(mn)}}{k}M\right)^2=\frac{k_r^{(mn)}J'_m(ak_r^{(mn)})}{J_m(ak_r^{(mn)})}. \tag{2.12}$$

Once again, the procedure is to start at a well-known value of axial wave number: the rigid-walled solution. It takes advantage of the fact that the solutions to Equation 2.8 are independent of the flow velocity (the wall is rigid regardless of the Mach number). As in the no-flow case, a similar analysis can be carried out regarding the appearance of irregular modes for certain impedances. In this case, besides the two possible acoustic surface waves, two hydrodynamic modes may appear, and this is also discussed in Chapter 5.

2.2.2 Rectangular ducts

Figure 2.7 shows the reference geometry for a rectangular duct, which is also valid for the impedance eduction techniques. Two hard-walled sections (1 and 3) and a lined section (2) compose the duct of dimensions b and h, respectively the width and height of the duct. The liner can be seen as a wall impedance Z of length L at $x=0$. Uniform mean flow is present in the $z+$ direction. It is convenient to write the general solution to Equation 2.2 considering downstream and upstream propagating waves because of the wall impedance transitions at $x=0$ and $x=L$ in this case,

$$p(x,y,z)=\sum_{m=0}^{\infty}\sum_{n=0}^{\infty}A_i^{(mn)}\psi_i^{(mn)}e^{-ik_{zi}^{(mn)}z} \tag{2.13}$$

$$+\sum_{m=0}^{\infty}\sum_{n=0}^{\infty}A_r^{(mn)}\psi_r^{(mn)}e^{ik_{zr}^{(mn)}z}, \tag{2.14}$$

where i and r denote the incident and reflected waves propagating respectively in the $z+$ and $z-$ directions and (mn) is the mode index in the x and y directions, respectively. The axial wave number k_z satisfies the dispersion relation

$$k_x^2+k_y^2+k_z^2=\left(k+Mk_z\right)^2, \tag{2.15}$$

where k_x and k_y are the transverse wave numbers in the x and y directions, respectively.

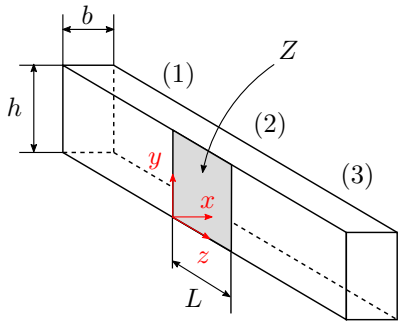

Figure 2.7 – Rectangular duct with width b and height h. At $x = 0$ in section (2) the wall has an impedance Z and length L.

Equation 2.13 is a general solution, so boundary conditions have to be applied. In the hard-walled section, the normal acoustic particle velocity must vanish,

$$\left.\frac{\partial p}{\partial x}\right|_{x=0} = \left.\frac{\partial p}{\partial x}\right|_{x=b} = \left.\frac{\partial p}{\partial y}\right|_{y=0} = \left.\frac{\partial p}{\partial y}\right|_{y=h} = 0, \tag{2.16}$$

leading to transverse wave numbers for the mn-th mode,

$$k_x^{(m)} = \frac{\pi m}{b}, \tag{2.17}$$

$$k_y^{(n)} = \frac{\pi n}{h}, \tag{2.18}$$

and mode shapes with cosine form,

$$\psi^{(mn)} = \cos\left(k_x^{(m)} x\right) \cos\left(k_y^{(n)} y\right), \tag{2.19}$$

as illustrated in Figure 2.8. Notice that red regions represent positive pressure, whereas blue regions represent negative pressure. The nodal lines i.e. the regions where pressure is always zero are represented in white.

An important assumption for the impedance eduction techniques is that, in the rigid-walled sections, only plane wave modes are propagating towards the lined section. In order to satisfy it, the wave frequency must be smaller than the first cross-section mode cut-on fre-

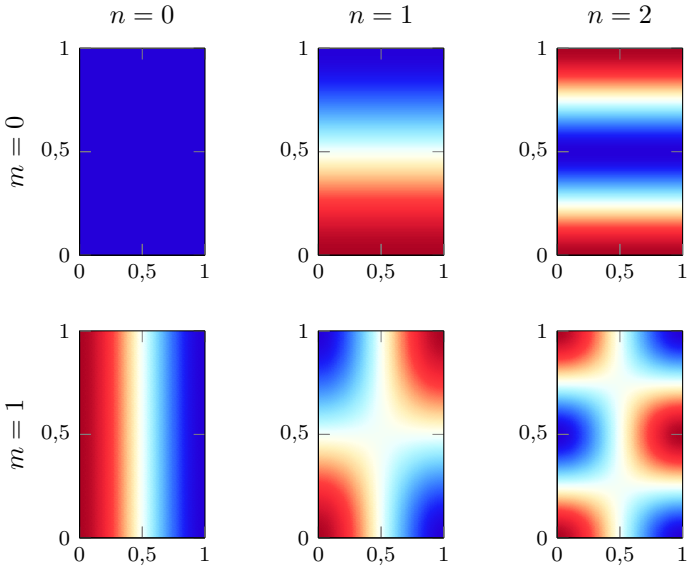

Figure 2.8 – Mode shapes $\psi^{(n)}$ in a dimensionless rectangular duct with rigid walls. Red regions represent positive pressure, whereas blue regions represent negative pressure.

quency, given by

$$f_c = \frac{c}{2h}\sqrt{1 - M^2}, \qquad \text{if } h > b, \tag{2.20}$$

or

$$f_c = \frac{c}{2b}\sqrt{1 - M^2}, \qquad \text{if } h < b. \tag{2.21}$$

In the lined section, the boundary conditions are symmetric in the y direction, thus the transverse wave number k_y can be calculated using Equation 2.18. At the lined surface, the flow velocity is non-zero (slip condition) so the wall impedance has to include uniform flow effects. As seen in the previous section, the usual approach is to assume the Ingard-Myers boundary condition at the lined wall. Together with the hard wall boundary condition at $x = b$, it leads to the eigenvalue

equation

$$\frac{ik}{Z}\left(1 - M\frac{k_z^{(mn)}}{k}\right)^2 = k_x^{(n)} \tan\left(k_x^{(n)} b\right). \tag{2.22}$$

A full derivation of this equation is given in Appendix A. Notice that Equation 2.22 relates axial and transverse wave numbers to the wall impedance for each mode (mn). This is a key equation for both impedance eduction techniques and sound attenuation prediction. If the wave numbers are known, Equation 2.22 can be solved for the liner impedance, and vice versa.

In the context of impedance eduction techniques, application of the Ingard-Myers boundary condition seems to be an oversimplification of the situation. In general, test rigs are rectangular ducts of small dimension, such that the flow is strongly sheared, if not fully developed at the lined section. Ideally, the exact flow profile should be included in the impedance eduction technique. This can be accomplished by solving the linearised Euler equations. Another approach is to modify the Ingard-Myers boundary condition by taking into account a small but finite boundary layer thickness, for example as proposed by Brambley [31] and Rienstra and Darau [32]. This is further discussed in Chapter 4 (and more specifically in Section 4.3).

2.3 Impedance eduction techniques

Liner impedance measurement in the presence of grazing flow is not a straightforward task. In recent years much attention has been paid to impedance eduction techniques. Differently from in situ methods [33], where the liner sample is instrumented, the impedance eduction techniques are non-destructive. The general procedure is described as follows. First, a liner sample of unknown impedance is placed in a duct with flow and acoustic field generated by loudspeaker. Microphones are positioned at the duct walls in order to measure the acoustic field. The sound pressure measured by the microphones is then compared to a simulated acoustic field for a given impedance guess, which can be achieved by means of an analytical formulation or numerical simulations. From that, a cost function can be defined, generally in the form of,

$$C(Z, f) = \sum_{j=1}^{J} \left(\frac{p_{j,\mathrm{exp}}(f) - p_{j,\mathrm{sim}}(Z, f)}{p_{j,\mathrm{exp}}(f)}\right)^2, \tag{2.23}$$

where j is the microphone index and J is the total number of microphones. Different cost functions are also possible, for example, by comparing transmission and reflection coefficients or insertion loss. Finally, the minimization of the cost function by means of an iterative routine leads to an estimation of the liner impedance. Such eduction techniques are also called inverse methods.

The acoustic field simulation is a key difference between eduction methods. For example, there are methods based on Finite Element Method simulations [11, 34–36], discontinuous Galerkin scheme [37], two-port formulation [38, 39] and mode matching methods[6] [40–42]. The acoustic propagation may satisfy either the convected Helmholtz equation (CHE), limited to uniform mean flow assumption, or the linearised Euler equations (LEE), which can account for shear flow profiles.

Another group of impedance eduction techniques requires no optimization routine: the direct (or also straightforward) methods. In these methods, the axial wave numbers k_z are extracted by means of Prony's method [43, 44] or the Kumaresan and Tufts approach [45]. If uniform flow is assumed, the transverse wave number k_x is found by the dispersion relation, leading to a direct solution of the impedance Z in Equation 2.22.

Most of the measurement techniques are based on microphones flush-mounted to the walls [11, 34, 35, 40–42, 45]. Other techniques include particle image velocimetry (PIV) [46] and laser Doppler anemometry (LDA) [37]. Despite potential advantages [46], the last two techniques have found little application in impedance eduction methods. These are most used to study the flow field close to the liner [47] and hydrodynamic instabilities over the lined surface [48, 49].

From the aforementioned eduction techniques, three have been implemented and validated at LVA/UFSC [50]: the mode matching method (MMM) [41], the two-port method (TPM) [39] and the straightforward method (SFM) [43]. The TPM requires a dual source technique [51] i.e. upstream and downstream measurements. However, as it will be shown later, different impedances are found by MMM and SFM when considering upstream or downstream propagating waves, whereas a basic assumption in TPM is that it remains the same in both cases. It is still not clear whether this is a failure of the Ingard-Myers boundary condition [45] or a physical characteristic of acoustic liners [52]. Therefore, the TPM is excluded from this work, and efforts are focused on the MMM and SFM.

On the following, the main equations for the MMM and SFM are

[6] Also called multi-modal methods

presented. A detailed derivation can be found on the original papers [41–44].

2.3.1 Mode matching method

In the MMM, it is assumed that only plane waves are propagating towards the lined section, depicted in Figure 2.9, which results in the following acoustic fields at each section:

$$p_1(x,y,z) = A_{1i}^{(1)} e^{-ik_{z1i}^{(1)} z} + \sum_{q=1}^{Q} A_{1r}^{(q)} \psi_{1r}^{(q)} e^{ik_{z1r}^{(q)} z}, \tag{2.24}$$

$$p_2(x,y,z) = \sum_{q=1}^{Q} A_{2i}^{(q)} \psi_{2i}^{(q)} e^{-ik_{z2i}^{(q)} z} + \sum_{q=1}^{Q} A_{2r}^{(q)} \psi_{2r}^{(q)} e^{ik_{z2r}^{(q)} (z-L)}, \tag{2.25}$$

$$p_3(x,y,z) = \sum_{q=1}^{Q} A_{3i}^{(q)} \psi_{3i}^{(q)} e^{-ik_{z3i}^{(q)} (z-L)} + A_{3r}^{(1)} e^{ik_{z3r}^{(1)} (z-L)}, \tag{2.26}$$

where the wave numbers $k_x^{(q)}$ and $k_y^{(q)}$ and mode shapes $\psi^{(q)}$ follow the derivation from Section 2.2.2. The mode index (mn) has been substituted by (q) for the sake of brevity. Notice that $q = 1$ corresponds to plane wave mode.

The next step is to satisfy the continuity of pressure and axial particle velocity at the interfaces, $z = 0$ and $z = L$,

$$p_1(x,y,0) = p_2(x,y,0), \tag{2.27}$$

$$p_2(x,y,L) = p_3(x,y,L), \tag{2.28}$$

$$u_{z1}(x,y,0) = u_{z2}(x,y,0), \tag{2.29}$$

$$u_{z2}(x,y,L) = u_{z3}(x,y,L). \tag{2.30}$$

By using the orthogonality between modes it is possible to end up with a system of $4Q$ equations and $4Q$ unknowns: the modal amplitudes $A_{1r}^{(q)}$, $A_{2i}^{(q)}$, $A_{2r}^{(q)}$ and $A_{3i}^{(q)}$. The required inputs are the incident plane-wave amplitude in section 1, $A_{1i}^{(1)}$, and the exit reflection coefficient $R_e^{(q)} = A_{3r}^{(q)}/A_{3i}^{(q)}$, which is zero for all $q > 1$ since the only reflected mode is the plane wave mode.

The system of equations is solved for an expected impedance value. Using the calculated modal amplitudes, the acoustic field is computed at positions which correspond to the microphones. The cost

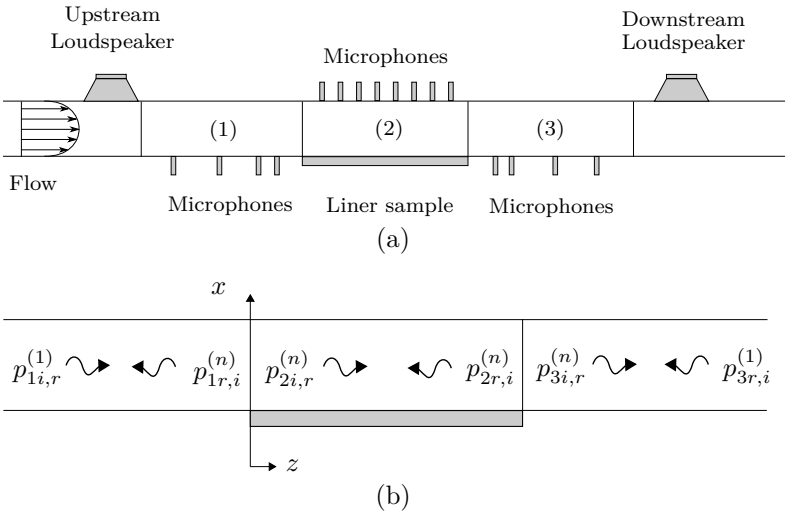

Figure 2.9 – Schematic top view of the test rig (a) and in-duct acoustic propagation (b).

function from Equation 2.23 is minimized to find the liner impedance. In the current work, the Matlab `fsolve` minimizer with the Levenberg-Marquardt algorithm is used [53], with mostly default options. Notice that the cost function is solved independently for each frequency f, thus a non-smooth impedance curve may be obtained. The fact that the optimization is repeated at each frequency step can also lead to a considerable computational cost, specially for noisy input data. Alternatively, an impedance model can be used in the optimization process to guarantee a smooth and physical behaviour, and to reduce processing time as well. This idea is further explored in Chapter 4.

2.3.2 Straightforward method

Differently from the MMM, the SFM is a direct impedance eduction technique i.e. no minimization is required. The pressure at the wall opposed to the liner can be rewritten from Equation 2.13 as the following sum of complex exponentials

$$p(x = b, y, z) = \sum_{q=1}^{2Q} A^{(q)} e^{\zeta^{(q)} z}, \tag{2.31}$$

where $\zeta^{(q)} = (-1)^q \, ik_z^{(q)}$. Since both upstream and downstream propagating waves are considered, the total number of modes is $2Q$. If the microphones are equally spaced, Prony's method can be employed to extract the axial wave numbers. Thus, Equation 2.31 is rewritten as

$$p_j = \sum_{q=1}^{2Q} A^{(q)} e^{\zeta^{(q)} j \Delta z}, \tag{2.32}$$

for $j = 1, ..., J$ and Δz the distance between consecutive microphones positioned according to Figure 2.9. The procedure is to convert such a non-linear problem into a linear least-square problem by means of Prony's method, which gives the mode amplitudes $A^{(q)}$ and axial wave numbers $\zeta^{(q)}$. Since spurious solutions may be obtained, a systematic procedure must be employed to eliminate non-physical results [43, 44].

Once the axial wave number k_z is known, it can be related to the transverse wave number k_x by the dispersion relation. If the wave frequency is below the first cut-on frequency in the y direction[7], $k_y^{(q)} = 0$ for any mode. Thus, the dispersion relation is simplified to

$$k_x^{(q)} = \sqrt{\left(k \mp M k_z^{(q)}\right)^2 - \left(k_z^{(q)}\right)^2}, \tag{2.33}$$

where $\mp$ follows downstream and upstream propagating waves, respectively. The final step is to find the wall impedance by means of the Ingard-Myers boundary condition [28, 29],

$$Z = \frac{ik}{k_x^{(q)}} \left(1 - M \frac{k_z^{(q)}}{k}\right)^2 \cot\left(k_x^{(q)} b\right). \tag{2.34}$$

Whereas the axial wave number calculation is independent of any flow assumption, the wall impedance calculation considers an uniform flow. Alternatively, a shear flow with zero velocity at the walls could be included, leading to solution of the Pridmore-Brown equation [54]

$$\frac{d^2 p}{dx^2} + \frac{2k_z}{k - M(x)k_z} \frac{dM}{dx} \frac{dp}{dx} + \left[(k - M(x)k_z)^2 - k_z^2\right] p = 0. \tag{2.35}$$

The flow profile $M(x)$ is chosen based on curve fitting to experimental data. The boundary conditions at the rigid wall are: a pressure constant of arbitrary value, and zero normal acoustic particle velocity,

[7] As described in Chapter 4, this is a valid assumption in the test rig

i.e.

$$p = 1, \tag{2.36}$$

and

$$\left.\frac{dp}{dx}\right|_{x=b} = 0. \tag{2.37}$$

From solving the pressure profile $p(x)$, the wall impedance can be calculated by the following boundary condition:

$$\rho \left.\frac{dp}{dx}\right|_{x=0} = \frac{i\omega}{Z} p. \tag{2.38}$$

The implementation of the aforementioned equations is discussed in Chapter 4, more specifically in Section 4.3. The derivation of the Pridmore-Brown equation can also be performed for circular ducts. Shear flow effects on the axial wave number (and therefore on the wave decay rate) is a key discussion in Chapter 6.

3 PREDICTIVE MODELS FOR LINER IMPEDANCE

The first predictive models for acoustic liners were developed in the 1970s alongside the introduction of liners in turbofan aero-engines. At the time, the characterization of liners was performed experimentally by means of the impedance tube method and in-situ techniques [33], while test rigs were fairly new. Since these options were expensive and time consuming, semi-empirical predictive models were developed as a low-cost prediction tool of liner impedance based on its geometrical parameters and operating conditions. Still today, predictive models are used to design new liners and as a first estimate of liner impedance in early project stages.

3.1 Semi-empirical models

In general, semi-empirical models are based on the sum of several effects, such as viscous and mass impedance Z_V, radiation impedance Z_R, non-linear effects Z_{NL} and backing impedance Z_B, which results in the normalized impedance

$$Z = Z_V + Z_R + Z_{\mathrm{NL}} + Z_B = \theta + i\chi. \tag{3.1}$$

The usual procedure is to derive analytically the viscous, radiation and backing impedances, and to model the non-linear effects, namely grazing flow and high SPL, based on experimental results. The final equation is a function of air properties (kinematic viscosity ν, air density ρ, speed of sound c), liner geometry (hole diameter d, plate thickness t, cavity depth L and percentage of open area (POA) σ) and operating conditions (source frequency f, mean Mach number M and acoustic particle velocity u_0),

$$Z = Z(\ \underbrace{\nu, \rho, c}_{\substack{\text{air}\\ \text{properties}}}\ ,\quad \underbrace{d, \tau, l, \sigma}_{\text{geometry}}\quad ,\quad \underbrace{f, M, u}_{\substack{\text{operating}\\ \text{conditions}}}\ ). \tag{3.2}$$

Most of the semi-empirical models proposed in the last decades are valid for single degree of freedom and locally reacting acoustic liners with perforated plate [5, 14, 16, 20, 21].

In the following sections, some of the main models available in the literature are presented. In Section 3.2 the predictive values of im-

pedance are compared to experimental results. A careful examination of the under- and overpredicted values regarding the dominating terms in the equations is also performed.

3.1.1 Guess model

One of the earliest works on semi-empirical models was published by Guess [20]. The main objective was to calculate the geometrical parameters of a perforated plate acoustic liner given a desired impedance, but the reverse path can also be used. The analysis is limited to a single-frequency excitation in order to avoid non-linear effects of interaction between multiple tones. Another constraint is the liner geometry, which has to comply with $\tau, d, s \ll \lambda$, where s is the spacing between holes and $\lambda = c/f$ is the acoustic wavelength.

The viscous and mass effects are derived by Kinsler and Frey [55] for a single tube of diameter d and short length τ, and it is given in the non-dimensional form by

$$Z_V = -\frac{i\omega\tau}{\sigma c}\left[\frac{4}{K_s d}\frac{J_1(K_s d/2)}{J_0(K_s d/2)} - 1\right], \qquad K_s = \sqrt{-\frac{i\omega}{\nu}}, \tag{3.3}$$

where J_1 and J_0 are the first and zeroth order Bessel functions of the first kind, K_s is the Stokes wave number and $\omega = 2\pi f$. Assuming $|K_s d/2| > 10$, which is valid for the typical frequency range of interest and liner geometry under analysis in this work, and accounting for end effects [56], the impedance can be approximated by

$$Z_V \simeq \frac{\sqrt{8\nu\omega}}{\sigma c}\left(1 + \frac{\tau}{d}\right) + i\left(\frac{\sqrt{8\nu\omega}}{\sigma c}\left(1 + \frac{\tau}{d}\right) + \frac{\omega\tau}{\sigma c}\right). \tag{3.4}$$

The radiation impedance of an opening with diameter d is derived by Morse and Ingard [57] as

$$Z_R = \frac{1}{\sigma}\left\{\left[1 - \frac{2c}{\omega d}J_1(\omega d/c)\right] + i\frac{4}{\pi}\int_0^{\pi/2} \sin\left[\frac{\omega d}{c}\cos(\phi)\right]\sin^2\phi\, d\phi\right\}. \tag{3.5}$$

The same procedure used for the mass impedance is repeated. Assuming $\omega d/c < 1/2$, which is valid for all liners and frequency range under analysis in this work, and accounting for interaction effects between adjacent holes, sound amplitude level and grazing flow, the radiation

impedance can be approximated by

$$Z_R \simeq \frac{\pi^2}{2\sigma}\left(\frac{fd}{c}\right)^2 + i\frac{\omega\delta_e}{\sigma c}, \tag{3.6}$$

where δ_e can be interpreted as an orifice end correction [20], and is given by

$$\delta_e = \frac{0.85d(1-0.7\sqrt{\sigma})}{1+305M^3}\left(\frac{1+5000M_a^2}{1+10^4M_a^2}\right), \tag{3.7}$$

where $M_a = u/c$ is the acoustic particle velocity Mach number. The orifice interactions are given by $(1-0.7\sqrt{\sigma})$ as proposed by Ingard [56], the grazing flow effect is given by $1/(1+305M^3)$ [58], and the last term between parenthesis is an attempt from Guess to account for sound amplitude effects [20].

The grazing flow and high sound pressure level mostly affect the resistance, and Ingard [59] proposed the following expression to include non-linear effects

$$\theta_{\mathrm{NL}} = \frac{(1-\sigma^2)}{\sigma}\left[\frac{|u|+|v|}{c}\right], \tag{3.8}$$

where $|v|$ is the magnitude of the turbulent velocity fluctuation [20], which can be approximated by $|v|/c \simeq 0.3M$ for perforated plates, according to Feder and Dean [60]. It is worthwhile to mention that a single perforated test sample with 22 % of POA was used, and the test apparatus was a side branch duct i.e. the perforated plate was flush mounted to a duct with flow, and a side branch was connected to the perforated plate where acoustic drivers were placed on its extremity.

Finally, the backing impedance of a perforated plate with a perpendicular honeycomb and rigid backing wall is given by [20]

$$\chi_B = -\cot\left(\frac{\omega l}{c}\right). \tag{3.9}$$

The sum of all effects results in the normalized resistance and reactance, respectively,

$$\theta_{\mathrm{G}} = \underbrace{\frac{\sqrt{8\nu\omega}}{\sigma c}\left(1+\frac{\tau}{d}\right)}_{\text{viscous}} + \underbrace{\frac{\pi^2}{2\sigma}\left(\frac{fd}{c}\right)^2}_{\text{radiation}} + \underbrace{\frac{(1-\sigma^2)}{\sigma}0.3M}_{\text{grazing flow}} + \underbrace{\frac{(1-\sigma^2)}{\sigma}\frac{|u|}{c}}_{\text{high SPL}}, \tag{3.10}$$

$$\chi_{\mathrm{G}} = \underbrace{\frac{\sqrt{8\nu\omega}}{\sigma c}\left(1+\frac{\tau}{d}\right)+\frac{\omega\tau}{\sigma c}}_{\text{viscous}} + \underbrace{\frac{\omega\delta_e}{\sigma c}}_{\substack{\text{radiation +}\\ \text{non-linear}}} - \underbrace{\cot\left(\frac{\omega l}{c}\right)}_{\text{backing}}. \tag{3.11}$$

3.1.2 Kooi and Sarin model

Kooi and Sarin [14] focused on the effects of grazing flow on locally reacting perforated liners. Previous works had shown that friction velocity was a better parameter to describe the effect of the grazing flow [15]. Therefore, Kooi and Sarin controlled artificially the boundary layer thickness at mean Mach numbers up to 0.45 and measured the impedance using a two microphone in-situ technique [33]. The SPL was held constant between 130 and 140 dB to avoid non-linear losses due to high acoustic particle velocity, although this is already considered a non-linear regime by other authors [16, 17]. The noise source was placed downstream to the liner and five different test samples were measured. The following normalized resistance was proposed[1],

$$\theta_{\mathrm{KS}} = \underbrace{\frac{\sqrt{8\nu\omega}}{\sigma c}\left(\frac{\tau}{d}\right)}_{\text{viscous}} + \underbrace{\frac{(5-\tau/d)}{4\sigma c}(9.9U_* - 3.2fd)}_{\text{grazing flow}}, \tag{3.12}$$

where $U_* = \sqrt{\tau_w/\rho}$ is the friction velocity and τ_w is the wall shear stress. This equation is restricted to a certain range of geometric values [14],

$$0.4 < \tau/d < 1.6 \tag{3.13}$$

$$U_*/(fd) > 0.2 \tag{3.14}$$

$$u/U_* < 4.0 \tag{3.15}$$

For $U_*/(fd) < 0.2$ and/or $u/U_* > 4.0$ the resistance given by Guess [20] without the grazing flow term can be used. The ratio between acoustic particle velocity and friction velocity u/U_* indicates which term is dominating the non-linear losses and it is based on the work from Goldman [15].

The reactance is similar to the equation proposed by Guess [20],

[1] In the original paper the viscous term has opposite sign. This would lead to a negative resistance, which is a physical violation of acoustic liners. Also, all other models have positive viscous terms.

with a different radiation correction term, and is given by

$$\chi_{\mathrm{KS}} = \underbrace{\frac{\sqrt{8\nu\omega}}{\sigma c}\left(1+\frac{\tau}{d}\right)+\frac{\omega\tau}{\sigma c}}_{\text{viscous}} + \underbrace{\frac{\omega\delta_e^*}{\sigma c}}_{\substack{\text{radiation +}\\ \text{grazing flow}}} - \underbrace{\cot\left(\frac{\omega l}{c}\right)}_{\text{backing}}, \tag{3.16}$$

where

$$\delta_e^* = 0.85d(1-\sqrt{\sigma})\left[0.92 - 0.75\frac{U_*}{f\tau} + 0.11\left(\frac{U_*}{f\tau}\right)^2\right]. \tag{3.17}$$

3.1.3 Motsinger and Kraft model

Motsinger and Kraft [5] proposed modifications mainly in the resistive part of Guess model, so that

$$\theta_{\mathrm{MK}} = \underbrace{\frac{32\nu\tau}{c\sigma C_D d^2}}_{\text{viscous}} + \underbrace{\frac{|u|}{2\sigma^2 c C_D^2}}_{\text{grazing flow + high SPL}}, \tag{3.18}$$

where C_D is the discharge coefficient, and it can be interpreted as a hole diameter correction due to the formation of the *vena contracta*. Typically a value of 0.76 is used, although Elnady [61] concluded that the discharge coefficient is a function of hole diameter and plate thickness, and a more recent paper from Zhang and Bodony [17] showed that discharge coefficient changes during the inflow and outflow cycles. The viscous term comes from Equation 3.5 for $|K_s d/2| < 1$, which is not a valid assumption for the liners used in this work. The acoustic particle velocity u in Equation 3.18 includes an empirical correction to account for flow turbulence i.e. grazing flow. In practice, Equation 3.18 has to be solved iteratively together with

$$|u| = \frac{\sqrt{p^2 + (90\,000M^2)^2}}{\rho c\sqrt{\theta^2+\chi^2}}. \tag{3.19}$$

The aforementioned turbulence correction is included empirically in the total pressure by $90\,000M^2$.

The predicted impedance was compared to results from a two

microphone in-situ technique [33] with acoustic source upstream to the test sample. The reactance is similar to Guess model [20], except part of the viscous term was excluded, and is given by

$$\chi_{\mathrm{MK}} = \underbrace{\frac{\omega\tau}{\sigma c}}_{\text{viscous}} + \underbrace{\frac{\omega\delta_e}{\sigma c}}_{\substack{\text{radiation +} \\ \text{grazing flow}}} \underbrace{- \cot\left(\frac{\omega l}{c}\right)}_{\text{backing}}. \tag{3.20}$$

3.1.4 Elnady and Bodén model

Elnady and Bodén [21] do not use any asymptotic value to model the viscous and radiation impedances, so that the resistance is given by

$$\begin{aligned}\theta_{\mathrm{EB}} = & \underbrace{\Re\left\{\frac{i\omega}{\sigma c C_D}\left[\frac{\tau}{F(K_s d)} + \frac{\epsilon_\theta}{F(K_s d)} f_{\mathrm{int}}\right]\right\}}_{\text{viscous}} \\ & + \underbrace{\frac{1}{\sigma}\left[1 - \frac{2cJ_1(\omega d/c)}{\omega d}\right]}_{\text{radiation}} + \underbrace{\frac{0.5}{\sigma} M}_{\substack{\text{grazing} \\ \text{flow}}} + \underbrace{(1-\sigma^2)\frac{|u|}{2\sigma^2 c C_D^2}}_{\text{high SPL}},\end{aligned} \tag{3.21}$$

where

$$F(K_s d) = 1 - \frac{4}{K_s d}\frac{J_1(K_s d/2)}{J_0(K_s d/2)}, \tag{3.22}$$

$$\epsilon_\theta = 0.2d + 200d^2 + 16000d^3, \tag{3.23}$$

$$f_{\mathrm{int}} = 1 - 1.47\sqrt{\sigma} + 0.47\sqrt{\sigma^3}. \tag{3.24}$$

Physically, ϵ_θ accounts for hole end correction and f_{int} is the interaction factor between holes. The non-linear terms are similar to Guess model [20]. The grazing flow constant is set to 0.5 and the high SPL term includes the discharge coefficient, which is function of the hole diameter and plate thickness, as measured by Elnady and Bodén [61].

The reactance also accounts for the viscous impedance in its original form. The grazing flow and high SPL effects are independent

and the radiation term is left out. Therefore,

$$\chi_{\mathrm{EB}} = \underbrace{\Im\left\{\frac{i\omega}{\sigma c C_D}\left[\frac{\tau}{F(K_s d)} + \frac{\epsilon_\chi}{F(K_s d)} f_{\mathrm{int}}\right]\right\}}_{\text{viscous}} - \underbrace{\frac{0.3}{\sigma} M}_{\substack{\text{grazing}\\ \text{flow}}} - \underbrace{(1-\sigma^2)\frac{|u|}{6\sigma^2 c C_D^2}}_{\text{high SPL}} - \underbrace{\cot\left(\frac{\omega l}{c}\right)}_{\text{backing}}, \tag{3.25}$$

where $\epsilon_\chi = 0.5d$. The viscous, radiation and high SPL terms are adjusted based on no-flow in-situ measurements, whereas the grazing flow constant fits the results from measurements using a mode matching technique [42] and acoustic source downstream to the test sample.

3.1.5 Other semi-empirical models

A large number of other semi-empirical models are available in the literature, but in many cases they are not appropriate to this work due to: (i) empirical coefficients are not given; (ii) liners unalike in geometry; (iii) grazing flow effects are not included; etc. In order to illustrate some of these problems, other semi-empirical models are briefly discussed.

Murray [16] proposed a resistance model which accounts for viscous, grazing flow and high SPL effects, such that the final equation is similar to a sum of Kooi and Sarin and Motsinger and Kraft models [5, 14], so that

$$\theta_{\mathrm{M}} = k_1 \frac{\nu\tau}{c\sigma C_D d^2} + k_2 \frac{M\left[5 - \frac{\tau}{d}\right]}{4\sigma} - k_3 \frac{fd}{\sigma c} + k_4 (1-\sigma^2)\frac{|u|}{2\sigma^2 c C_D^2}. \tag{3.26}$$

The constants k_1, k_2, k_3 and k_4 are adjusted based on curve fitting to experimental results. The reactance follows the same model from Rice [58] and Motsinger and Kraft [5],

$$\chi_{\mathrm{M}} = \frac{\omega\tau}{\sigma c} + \frac{\omega\delta_e}{\sigma c} - \cot\left(\frac{\omega l}{c}\right), \tag{3.27}$$

with a small adjustment in the end-correction,

$$\delta_e = \frac{0.85d(1 - 0.7\sqrt{\sigma})}{1 + 200M^3}. \tag{3.28}$$

Since none of the coefficients are given by Murray, the set of available liner in this work would have to be divided into two subsets: (i) the curve fitting group and (ii) the cross-validation group. Unfortunately, a limited number of samples are available, and it was opted not to use this model.

Kirby and Cummings [62] also proposed a resistance model of perforated plates based on curve fitting to different grazing flow velocities,

$$\theta_{\mathrm{KC}} = \frac{\sqrt{8\nu\omega}}{\sigma c}\frac{\tau}{d} + \left[26.16\left(\frac{\tau}{d}\right)^{-0.169} - 20\right]\frac{U_*}{\sigma c} - 4.055\frac{f\tau}{\sigma c}. \qquad (3.29)$$

Notice that this equation is very similar to the model proposed by Kooi and Sarin (see Equation 3.12). The three tested samples used in this curve fitting had a relatively high percentage of open area (around 20 %) and hole diameter (approximately 3.0 mm). Also, the measurement apparatus was similar to the in situ technique used by Kooi and Sarin. However, the perforated plate was mounted on a single cavity i.e. no honeycomb structure was used, so the test samples were not actual liners. Thus, this model is not further investigated.

In summary, Table 3.1 lists the semi-empirical models and their attributes, such as measurement apparatus, source location in the test rig and included non-linear effects.

Table 3.1 – Semi-empirical models and their attributes, such as measurement apparatus, source location in the test rig and included effects.

Model	Measurement	Source	Grazing flow	High SPL
Guess	Side branch	-	x	x
Kooi/Sarin	In situ	Downstream	x	-
Motsinger/Kraft	In situ	Upstream	x	x
Elnady/Bodén	MMM	Downstream	x	-
Murray	In situ	Downstream	x	x
Kirby/Cummings	In situ	Upstream	x	-

3.2 Comparison to experimental results

Apart from Murray's model, which has to be tuned, all the others are fully predictive i.e. once the desired geometry and operating conditions are known, the resulting impedance is predicted by the model.

In order to check their accuracy, a comparison is carried out between the models and experimental results obtained using the MMM. More details about the experimental procedure are given in Chapter 4. The test sample geometrical properties are listed in Table 2.1. In the experiments, the maximum SPL was fixed in 130 dB to avoid non-linear effects due to high SPL, and the flow velocity varies between Mach 0.10, 0.20 and 0.25. Since there is evidence of different educed impedances for upstream and downstream acoustic sources [13, 45], both results are included in the analysis.

Figure 3.1 summarizes the results for liner A. At no flow condition, the resistance is well predicted above 1.5 kHz. However, at lower frequencies, there is a considerably different trend in the curves. Whereas the predicted resistance is close to zero, the experimental result indicates a much higher resistance. In any case, the reactance is far from zero, and any of these resistances would result in a very low liner attenuation. As flow velocity increases, it is possible to see a difference between the models regarding the resistance, whereas the reactance is well predicted by all of them apart from Elandy and Bodén model. From all measurements, a flow velocity of Mach 0.25 is the most representative of a typical aeronautical situation, for instance an approach condition, so it is analysed in greater detail, with a focus on the resistive part. Both Guess and Elnady and Bodén models are almost constant with frequency and overpredict the resistance. Kooi and Sarin model varies slightly with frequency, but it is not able to capture the trend from experimental results. Motsinger and Kraft model is very close to the educed impedance with upstream source, specially above 1.5 kHz. In fact, this is the frequency range considered by Motsinger and Kraft for the curve fitting [5]. The geometry of the test sample is also very similar to liner A ($\sigma = 6.7\,\%$, $d \approx 0.8\,\text{mm}$ and $\tau \approx 0.8\,\text{mm}$), and the acoustic source position is the same.

In order to check the consistency of these trends, the predictive models are compared to experimental results of the second test sample, named liner B, and summarized in Figure 3.2. This is a very high attenuating liner, and thus some oscillations are seen in the educed impedance around 2.0 kHz and 2.5 kHz.

Firstly, the resistance is analysed. As previously seen, Guess and Elnady and Bodén models are not able to the capture the trend from the experimental results. Motsinger and Kraft model underpredicts the result for most of the considered frequency range. Kooi and Sarin model is the closest one in this case, since it is able to capture the resistance curve slope, although with a small offset (see Mach 0.20 and 0.25, for

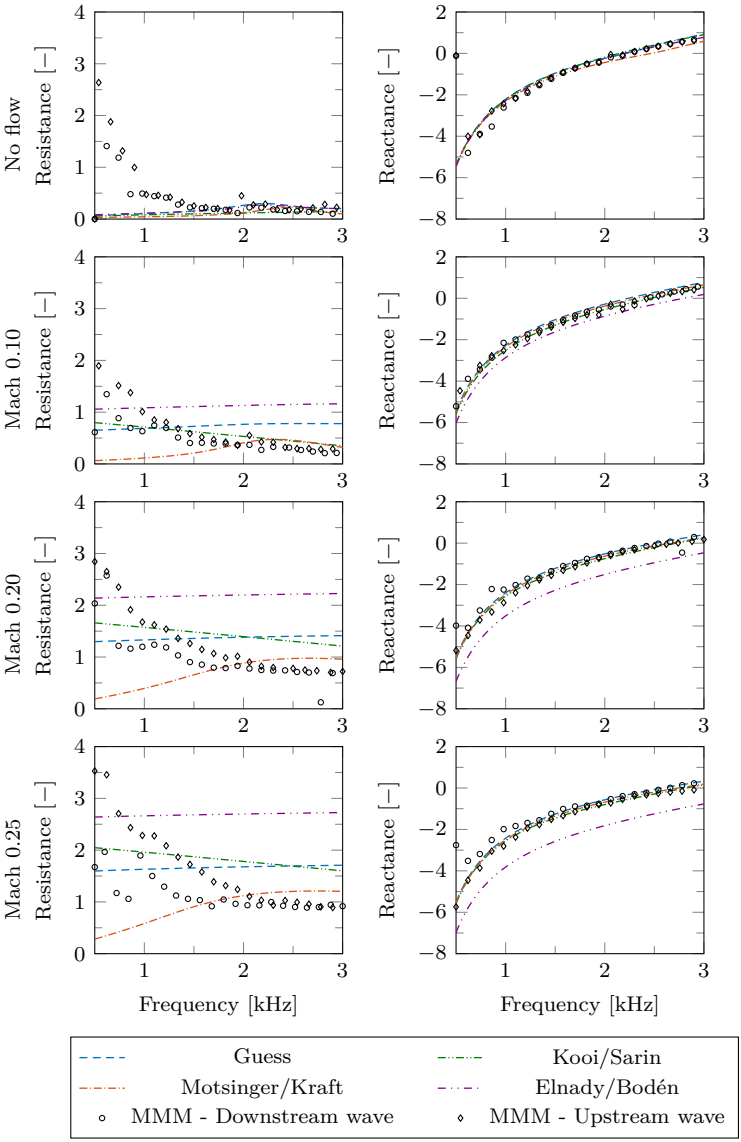

Figure 3.1 – Comparison between predictive models and experimental results for liner A at different flow velocities.

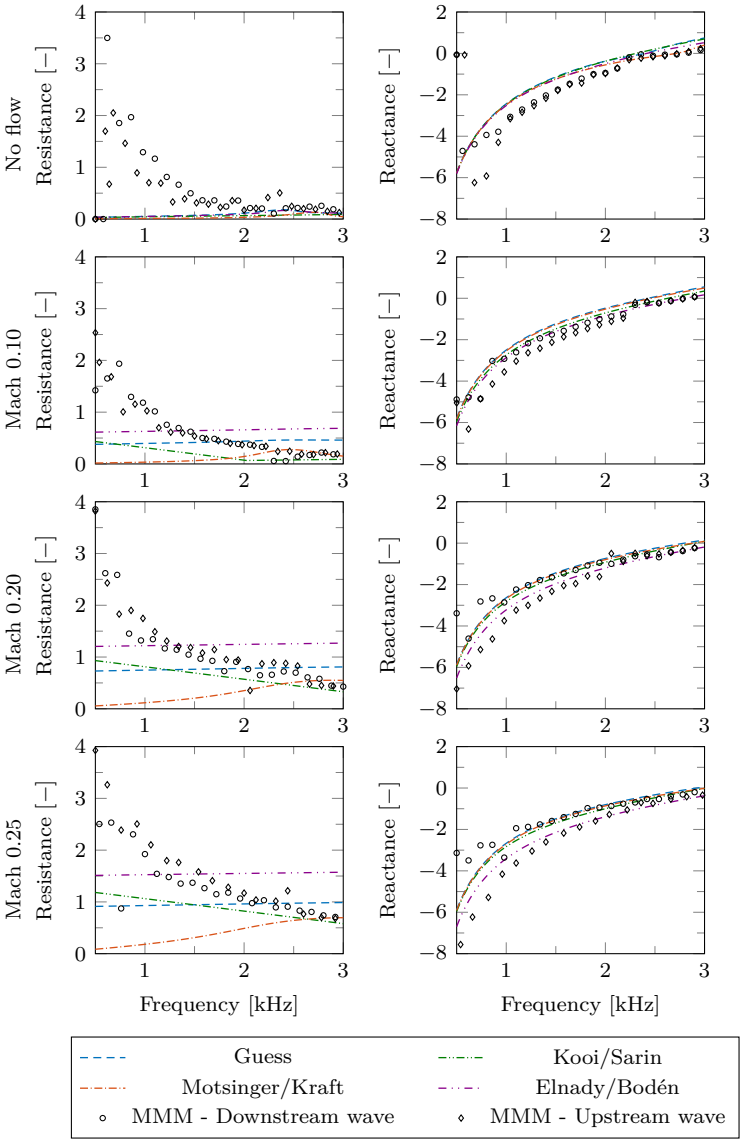

Figure 3.2 – Comparison between predictive models and experimental results for liner B at different flow velocities.

instance). The reactance results are not so smooth as compared to liner A. Most of the models are closer to the upstream source result, whereas Elnady and Bodén model is closer to the downstream source result. In fact, this model was adjusted based on measurements with downstream acoustic source, and it could explain the better agreement. The difference between upstream and downstream results is further discussed in Chapter 4.

3.3 Individual contributions of each physical effect

The individual contribution of each term in the semi-empirical models (associated with different physical effects) is analysed in this section. For the sake of brevity, only the results at $M = 0.25$ and maximum SPL of 130 dB are shown. Overall, it is very clear in Figure 3.3 that the grazing flow term is dominating the resistance values, with some contribution from the viscous term. The radiation term is negligible and the high SPL term accounts for a very small portion at 130 dB, as expected.

The constants chosen for the grazing flow term in Guess and Elnady and Bodén models are not sufficient to correctly represent the resistance since there is a considerable variation with frequency, mainly at lower frequencies, and therefore a term as function of frequency and geometry would be more suitable. This is well represented by Kooi and Sarin model, and a good agreement can be seen for liner B. However, it overpredicts the result for liner A, possibly as a consequence of the small number of test samples used to adjust this model. Motsinger and Kraft model shows a good agreement at higher frequencies, close to the liner resonance frequency, but fails to predict the resistance behavior at low frequencies. Elnady and Bodén model tries to improve the accuracy of the viscous and radiation terms, however the grazing flow is the dominant one.

Figure 3.4 summarizes the reactances from each model, except Elnady and Bodén model as it contains negative terms and would complicate the analysis. Compared to the resistance, the reactance is well predicted by all the models. Overall, liner A has a good agreement for both upstream and downstream results, and it is clear the importance to include the viscous and radiation effects to the backing impedance in order to correctly predict the reactance. Liner B shows a good agreement with the downstream wave results, and upstream wave results are correctly predicted only at higher frequencies.

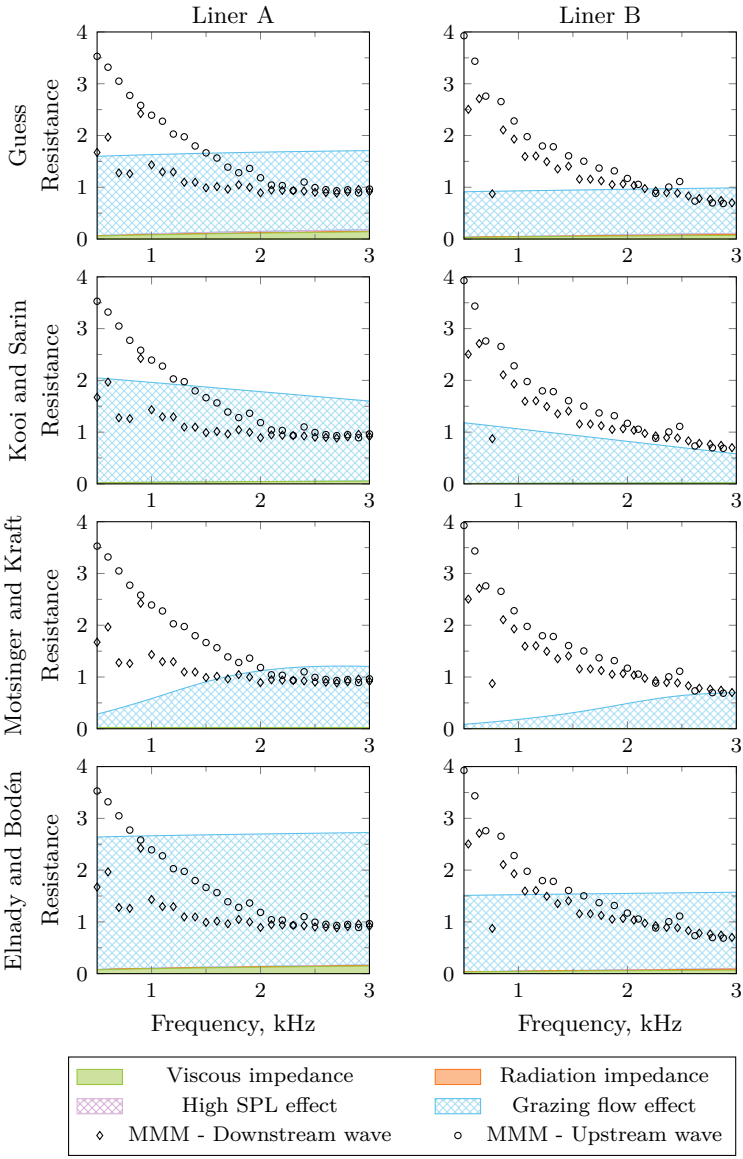

Figure 3.3 – Resistances from semi-empirical models and experimental results for two different test samples at Mach 0.25 and maximum SPL of 130 dB. Each area corresponds to a different effect. The sum of all these effects gives the total resistance.

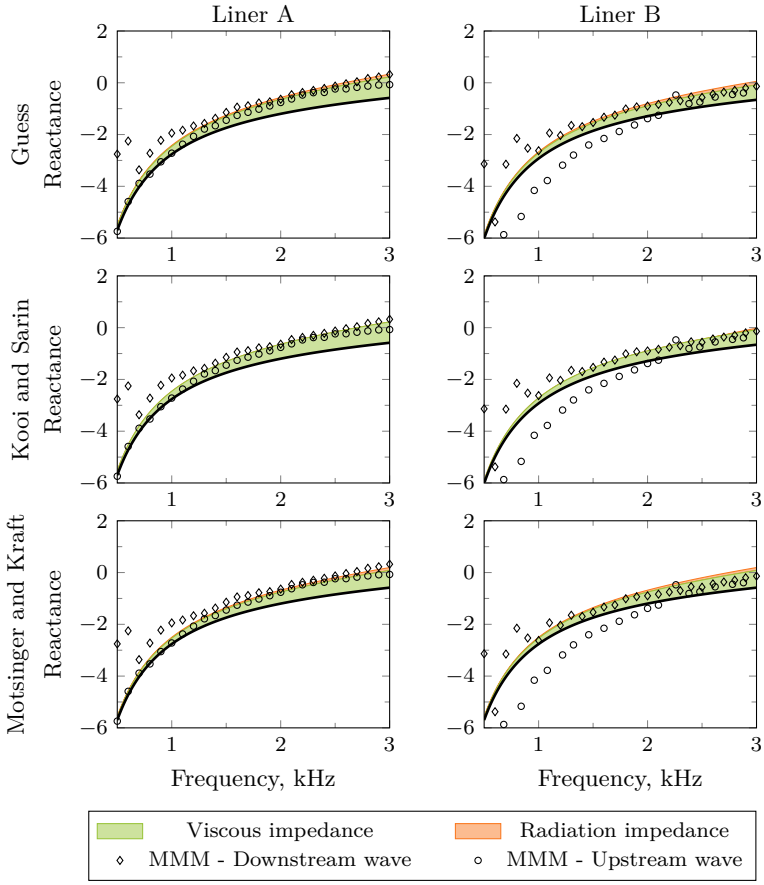

Figure 3.4 – Reactances from semi-empirical models and experimental results for two different test samples at Mach 0.25 and maximum SPL of 130 dB. Each area corresponds to a different effect. Black line (——) corresponds to the backing impedance. The sum of all these effects, starting at the backing impedance, gives the total reactance.

This demonstrates why efforts should be concentrated in the resistive part, especially in improving the non-linear terms. Most of them are simplistic and far from properly predicting the acoustic impedance. Models including the liner geometry and flow characteristics, as done by Kooi and Sarin, should be further investigated.

4 IMPEDANCE EDUCTION IMPROVEMENTS

This chapter addresses two different problems related to impedance eduction methods: (i) non-physical results in form of discontinuous curves and (ii) difference in the impedance eduction results regarding upstream and downstream propagating waves. Note that both parts are independent, although they could be investigated together.

As seen in Chapter 2, the problem of convergence to local minima in impedance eduction methods can be aggravated when using noisy experimental data, because experimental error can mask the minima or create other minima to which the optimization might converge. This issue is commonly observed in impedance curves obtained experimentally using impedance eduction methods, where the impedance curve display abrupt spikes or valleys that are not physical. In general, these problems are related to a low signal-to-noise ratio in the experimental data, as explained in Section 4.1. This is specially critical at frequencies close to the liner maximum attenuation, since the acoustic field is considerably attenuated by the liner but the flow noise is still present. Therefore, the inclusion of an impedance model in the optimization routine should correct this problem. More details are given in Section 4.2. Note that the so-called direct methods (such as the SFM) requires no optimization routine, and none of the impedance models can be included in the eduction method.

Even though, the educed impedance remains flow-direction sensitive. It is not clear whether this effect is related to the physics of acoustic liners, which could be affected by the flow direction, or erroneous assumptions in the mathematical modelling of the analytical acoustic field in the impedance eduction techniques. The latter is of main concern in Section 4.3. Usually, the main assumptions on these techniques are: (i) uniform flow and (ii) Ingard-Myers boundary condition [28, 29] at the lined wall. However, in general, test rigs have a small cross section, such that the flow profile is fully developed (or at least strongly sheared) at the lined section. Two different investigations are then proposed with the aim of better understanding the reasons behind the downstream/upstream discrepancies: (i) include an improved boundary condition under the assumption of uniform flow in the mode matching method, and (ii) include the flow profile in the straightforward method by means of the Pridmore-Brown equation.

This chapter is divided as follows. The impedance test rig at LVA/UFSC is first presented, as well the experimental procedure. On

the following, the mode matching method with impedance models is introduced. Finally, the effects of flow direction on the educed impedance are investigated by means of alternative boundary conditions.

4.1 LVA/UFSC impedance test rig

The experimental apparatus follows the geometrical specifications of the analytical formulation i.e. a rectangular duct, with a liner sample on one wall, and hard wall sections before and after the lined section. A total of 8 microphones are positioned in the hard wall sections (1) and (3), flush to the duct walls, according to the MMM formulation. The SFM requires the same 8 microphones positioned at the wall opposed to the liner. A list of the microphone positions for each impedance eduction technique is given in Table 4.1.

The acoustic sources can be placed upstream or downstream to the liner, leading to downstream and upstream propagating waves, respectively. An amplification system is responsible to achieve SPLs up to 130 dB. This level was chosen to avoid non-linear effects related to high SPL on the liner impedance. A ventilation system is used to generate a uniform flow at the duct inlet, which is able to achieve an average Mach number of 0.30. On the following, more details are given about the test rig, test samples and flow profile.

4.1.1 Test rig

The test rig built at LVA/UFSC is made of several modular, interchangeable sections, and follows the schematic view from Figure 4.1. The test section consists of 5 ducts, whose position can be switched to accommodate different test configurations. For instance, the source section, where the speakers are connected, can be positioned upstream or downstream to the liner sample in order to evaluate flow direction effects. There are 8 compression drivers for a single duct section in the test rig, which are able to generate sound pressure levels exceeding 140 dB at the test section. All results shown in this work were made using a single speaker with pure discrete tones never exceeding 130 dB in order to avoid non-linear effects.

The sections before and after the sample section are the two microphone sections. The liner sample is 0.20 m long, covering the entire duct height. The cross-section of the duct is 0.04 m by 0.10 m,

Table 4.1 – Microphone positions in the test rig. The coordinate system follows Figure 2.9.

Method	Location	Microphone	x [m]	y [m]	z [m]
MMM	Upstream	1	0.00	0.05	-0.59
		2	0.00	0.05	-0.42
		3	0.00	0.05	-0.33
		4	0.00	0.05	-0.28
	Downstream	5	0.00	0.05	0.48
		6	0.00	0.05	0.53
		7	0.00	0.05	0.62
		8	0.00	0.05	0.79
SFM	Along liner	1	0.04	0.05	0.03
		2	0.04	0.05	0.05
		3	0.04	0.05	0.07
		4	0.04	0.05	0.09
		5	0.04	0.05	0.11
		6	0.04	0.05	0.13
		7	0.04	0.05	0.15
		8	0.04	0.05	0.17

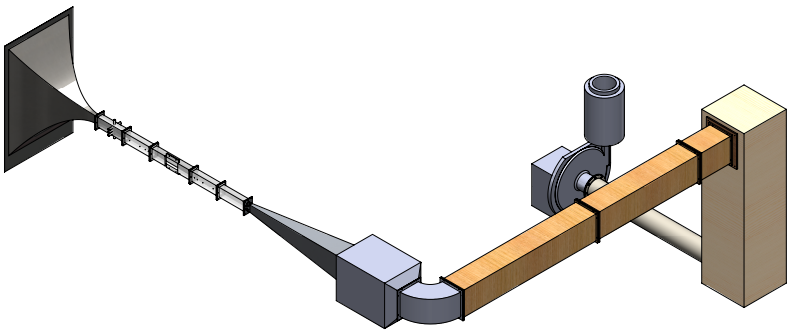

Figure 4.1 – Overview of the test rig.

which results in a no-flow cut-on frequency of 1700 Hz for the first transverse mode, as per Equation 2.20. Since the microphones are positioned on half of the duct height, which is exactly the nodal line of the first transverse mode (see Figure 2.8), the effect of high order modes is not captured until the excitation frequency reaches the second transverse mode at 3400 Hz. As a consequence, the frequency range under analysis is limited from 500 Hz to 3000 Hz.

Excitation signal generation, microphone signal acquisition, and controlling of the flow velocity, are executed by a custom software implemented in LabView. The average flow velocity used in the impedance eduction algorithms is calculated from the acoustic measurements at the microphones using a custom routine [12, 63] that was previously validated [12].

4.1.2 Flow profile

In order to correctly assess the effect of the boundary conditions, the flow profile in the test rig has to be further examined. Three arbitrary flow velocities are shown in Figure 4.2. The experimental results are based on measurements using a Pitot tube at half of the duct height i.e. at $y = 0.05\,\mathrm{m}$, and at half length of the liner i.e. $z = 0.10\,\mathrm{m}$. To perform the measurements, the lined section was replaced by a hard wall section with a small hole at the top to insert the Pitot tube. The uniform value is given by the average of the measurements points not only in the x-direction, but also in the y-direction, which results in a total of 29 measurement points. The experimental flow profile is compared to an analytical profile based on the following power law,

$$M(X) = M_{\max}\left[-4X\left(X-1\right)\right]^{(1/7)}, \tag{4.1}$$

where $0 \leq X \leq 1$. It has been observed that the ratio between the average and maximum Mach number $M_{\mathrm{avg}}/M_{\max}$ is approximately 0.9 at any flow velocity, as listed in Table 4.2. This analytical expression has been arbitrarily chosen due to the good agreement with experimental results, particularly at the first three measurement points. However, it is not a profile free of inconsistencies. For instance, its derivative to X is given by

$$\frac{dM}{dX} = \frac{M_{\max}}{7}\left[-4X\left(X-1\right)\right]^{(-6/7)}\left(-8X+4\right). \tag{4.2}$$

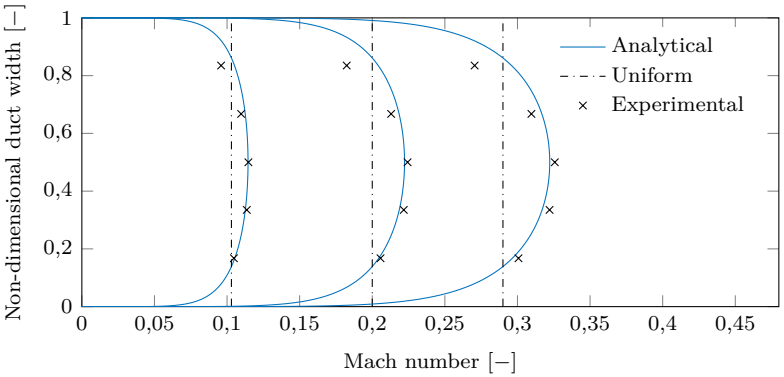

Figure 4.2 – Flow profiles at different flow velocities. The analytical profile (——) is given by Equation 4.1, the uniform profile (- · - · -) is an average value of the cross section and the experimental points (×) were measured using a Pitot tube.

Table 4.2 – Ratio between the average and maximum flow velocities.

Nominal flow velocity	$U_{\max}$ (m/s)	U_{avg} (m/s)	$U_{\text{avg}}/U_{\max}$
Mach 0.05	19.64	17.46	0.889
Mach 0.10	39.80	35.74	0.898
Mach 0.15	57.84	52.08	0.900
Mach 0.20	77.83	69.40	0.891
Mach 0.25	94.48	85.15	0.901

Thus, as X approaches zero, dM/dX tends to infinity. The wall shear stress τ_w, defined in Chapter 3 for Kooi and Sarin model, is function of this derivative, more specifically

$$\tau_w = \mu \left. \frac{dM}{dX} \right|_{X=0}, \tag{4.3}$$

where μ is the dynamic viscosity. Thus, the wall shear stress, and also the friction velocity would be infinite, a result incompatible with reality. In terms of numerical implementation, the Pridmore-Brown equation and its boundary conditions have to be evaluated at small but not zero distance. Chapter 6 explores in greater detail this implementation.

A more appropriate approach is to divide the profile in viscous

sublayer and outer turbulent layer. The former exhibits a linear profile at a distance very close to the wall. However, no information is available regarding the flow profile near the wall, and therefore any modelling assumption would find no experimental data for comparison. Nevertheless, the power law provides a good approximation of the actual flow and it is much more representative than uniform flow assumption.

4.1.3 Signal-to-noise ratio

In order to illustrate the problems related to the mode matching technique, the following test case is considered: test sample B, downstream acoustic source and Mach 0.20. The signal-to-noise ratio (SNR) is defined here as the difference between tonal excitation level and flow-induced noise. The latter is an effect of the turbulent boundary layer since the microphones are flush mounted to the wall. This results typically in a broadband noise level around 85 dB at Mach 0.20. An alternative conception is to recess the microphones and use a wire-mesh flush mounted to the wall, which results in a flow-induced noise reduction up to 5 dB [12]. Nonetheless this gain in SNR may be insufficient at frequencies close to the liner maximum attenuation frequency.

As seen in Figure 4.3, microphone 5 (downstream do the liner) shows a good SNR over all the frequency range. It is a section where the acoustic field is close to 130 dB and has not been affected by the liner sample. Microphone 4 (upstream to the liner) shows a large reduction in SNR due to liner attenuation specially in the frequency range of 2100 Hz and 2600 Hz. Microphone 5 has a slightly higher flow-induced noise level than microphone 4 because the boundary layer has been affected by the presence of the liner, resulting in a more turbulent boundary layer and a small reduction in SNR, which can be seen at low frequencies in Figure 4.3.

The problem of low SNR can be clearly seen in terms of insertion loss (IL) in the duct, defined as[1]:

$$\mathrm{IL} = 20 \log_{10} \left(\frac{A_{3i}^{(1)}}{A_{1i}^{(1)}} \right). \tag{4.4}$$

[1] Valid for upstream propagating wave. In the case of a downstream propagating wave, $\mathrm{IL} = 20 \log_{10} \left(A_{1i}^{(1)} / A_{3i}^{(1)} \right)$.

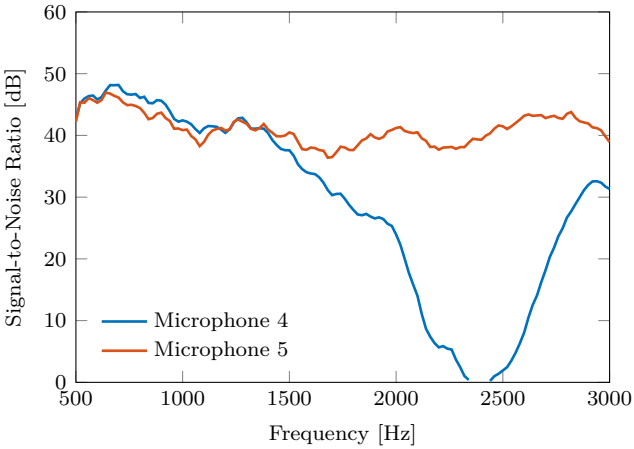

Figure 4.3 – Signal-to-noise ratio at microphones 4 (——) and 5 (——) for the following test case: test sample B, downstream acoustic source and Mach 0.20.

Typical SDOF liners exhibit a peak in insertion loss, which is not clearly defined in Figure 4.4. Therefore, it is not possible to quantify the maximum attenuation nor the frequency where it occurs. This analysis can be extended to the impedance eduction, as shown in Figure 4.5. The discontinuities and oscillations in the resistance and reactance between 2100 Hz and 2600 Hz are a non-physical behaviour of the liner and consequence of the poor SNR in this frequency range, justifying the use of an impedance model in the eduction method. Measurements with different test samples and acoustic source position exhibit the same trend, even at lower flow velocities, and therefore the use of an impedance model may be an important improvement.

In order to understand the discontinuities and oscillations in the impedance curve, a closer look at some frequencies is given by Figure 4.6, which show the contour plot of the cost function (Equation 2.23) at the frequencies of 1500 Hz and 2100 Hz, respectively. The former have a well defined region of minimum. The latter is a frequency with poor SNR, and the region of minimum is not well defined. Therefore, the educed impedance from the MMM may not represent the correct liner impedance.

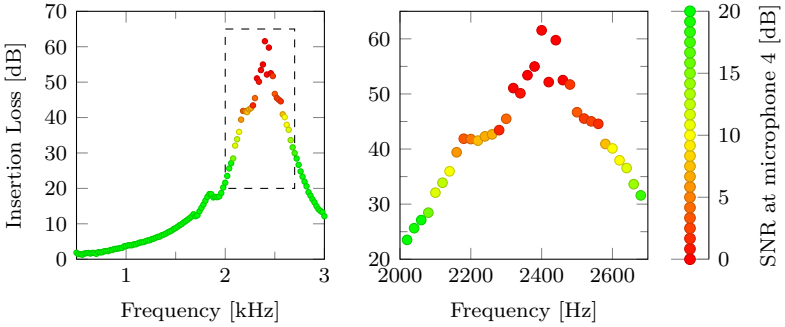

Figure 4.4 – Insertion loss of the test sample for the following test case: test sample B, downstream acoustic source and Mach 0.20. The coloured dots represent data quality based on the signal-to-noise ratio from microphone 4.

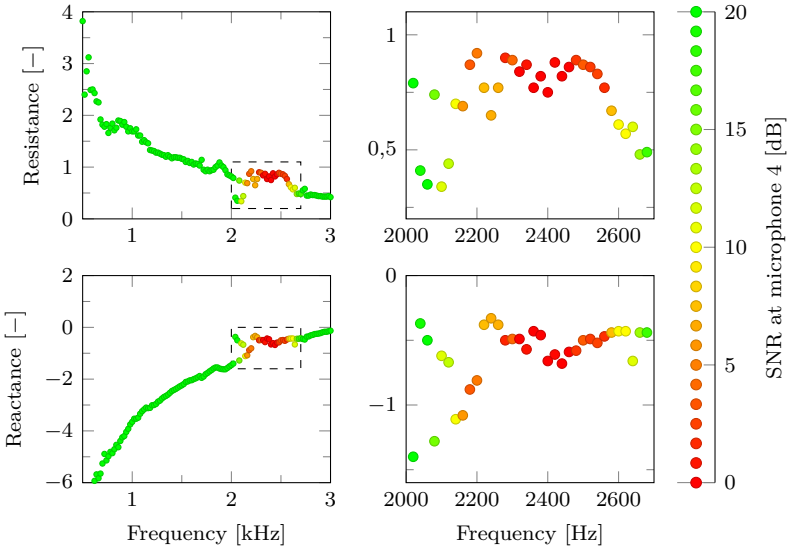

Figure 4.5 – Impedance eduction result based on the classical mode matching technique for the following test case: test sample B, downstream acoustic source and Mach 0.20. The coloured dots represent data quality based on the signal-to-noise ratio from microphone 4.

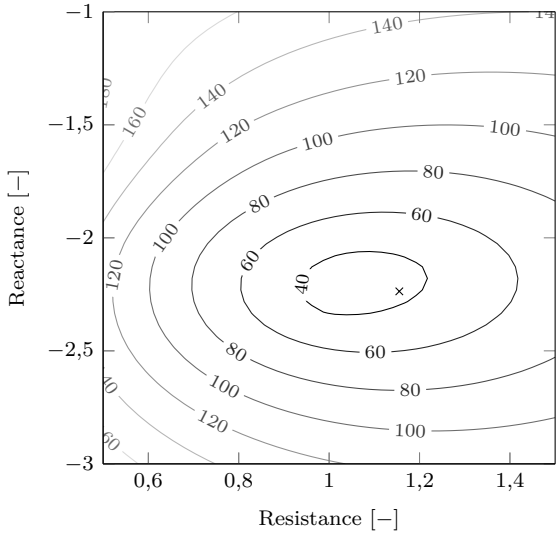

(a) 1500 Hz

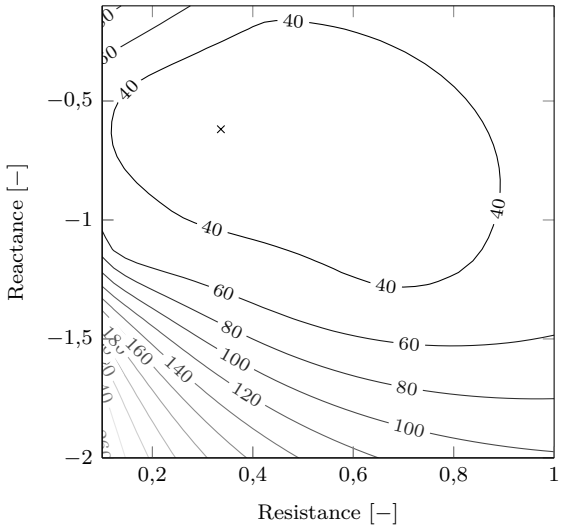

(b) 2100 Hz

Figure 4.6 – Contour plot of cost function at (a) 1500 Hz and (b) 2100 Hz given by the MMM for the following test case: test sample B, downstream acoustic source and Mach 0.20. Educed impedance given by the cross (×).

4.2 The Multiple-Frequency Mode Matching Method

In this section, a modification to the mode matching method is introduced. This idea was first proposed by Medeiros [63]. Following one of Medeiros' suggestions, different impedance models are investigated in order to evaluate which one better follows the experimental results.

In the original version, described in Section 2.3.1, the objective function is given by the sum of the squared percentage error between measured and calculated acoustic pressure at the j-th microphone position at each frequency and for a given impedance guess. The optimization problem can be rewritten considering a frequency-dependent impedance function $Z(\mathbf{x}, f)$, that gives the impedance for all frequencies for a given set of parameters $\mathbf{x}$. The acoustic field, then, is calculated using the impedance for each frequency, and the objective function, Equation 2.23, becomes a function of $\mathbf{x}$, and is summed over all frequencies to give the global error, according to:

$$C(\mathbf{x}) = \sum_{f=f_0}^{f_N} \left(\sum_{j=1}^{J} \left(\frac{p_{j,\exp}(f) - p_{j,\mathrm{MMM}}(Z(\mathbf{x}, f))}{p_{j,\exp}(f)} \right)^2 \right), \tag{4.5}$$

where J is the number os microphones used. The parameters in vector $\mathbf{x}$ are the new optimization variables, which are varied to minimize $C(\mathbf{x})$. By finding $\mathbf{x}$, the impedance is defined for all tested frequencies, solving a single, but larger, optimization problem. This new method requires the definition of a model for the impedance curve $Z(\mathbf{x}, f)$.

If a Mach dependent parameter is present in the model it could be included in the optimization process as well. Therefore, the acoustic field could be compared to the measurements at different flow velocities, and the objective function given by Equation 4.5 would be rewritten to include a sum over all the flow velocities. Such approach will not be considered here and the analysis will be restricted to results using Equation 4.5.

4.2.1 Impedance models

The impedance models presented here were developed for translating impedance values in frequency domain into an equivalent relation in time domain, mostly for use in numerical methods. This problem is

not trivial because of the necessity to guarantee that the resulting relation is physical, i.e., obeys causality, reality and passivity conditions. Violation of these conditions would manifest as non-physical results, like generation of energy at the wall or other non-physical instabilities.

Of particular interest are the Extended Helmholtz resonator [64] and the rational function models [65, 66], as they have shown good agreement with measured data [67, 68] and are further discussed in the next section. Other impedance models are available in the literature, such as the mass-springer-damper model[2] [69], but are not considered here. Semi-empirical models [5, 14, 20] were also analysed, but their expressions are, in general, too complicated or oversimplified to guarantee that the fundamental conditions are not violated [64]. Therefore, these models are not included in the multiple-frequency mode matching.

Any flow effect is accounted for by the Ingard-Myers boundary condition [29], but the parameters are allowed to vary with Mach number. This will be further discussed in Section 4.2.2.

4.2.1.1 Extended Helmholtz Resonator

The EHR, as the name suggests, is based on a simple Helmholtz resonator, whose impedance satisfies the fundamental conditions. More details on this matter and the derivation can be seen on the original paper [64]. The resulting frequency-dependent impedance expression is:

$$Z(\omega) = R + i\omega m - i\beta_c \cot\left(\frac{1}{2}\omega T_l - i\frac{1}{2}\varepsilon\right), \tag{4.6}$$

where R is the face-sheet resistance, m is the mass reactance of the air in the holes, β_c is a parameter to account for different cavity reactances, T_l is the response time, and ε is the damping in the cavity's fluid. In the original paper, advice is given on how to choose the parameters to generate curves that resemble liner impedance, i.e., without abrupt variations in the frequency range of interest and within coherent impedance values.

From Equation 4.6 it is straightforward to see that the vector $\mathbf{x}$, which define the impedance for a given frequency in the modified mode matching, is given by 5 parameters, so that

$$\mathbf{x} = \{R, m, \beta_c, T_l, \varepsilon\}. \tag{4.7}$$

[2] Also called the effective impedance model [68].

As previously discussed, all the parameters have physical interpretations. It is important therefore to limit the upper and lower possible values of the variables within feasible values. For instance, negative or too high resistances, oscillating curves, and other problems can be avoided. Some of these bounds were defined empirically while care was taken not to overly limit the possible curves that can be generated by Equation 4.6. The defined upper and lower bounds for all parameters are given in Table 4.3.

4.2.1.2 Rational functions

Özyörük and Long [65] proposed the use of rational functions to represent the impedance in the frequency domain. This can be easily translated into the time domain by means of the z-transform. Such an example of impedance function is given by

$$Z(\omega) = r_1 + \frac{r_2 - r_1}{1 + i\omega r_3} + \frac{i\omega r_4}{(1 - \omega^2/r_6^2) + i\omega r_5} + i\omega r_7, \tag{4.8}$$

which was used to curve fit the parameters $\mathbf{r} = r_{1,\ldots,7}$ to experimental data from a ceramic tubular liner [67]. There is no physical interpretation of the parameters, although some of them resemble terms from the EHR, e.g. r_1 and face sheet resistance R, and r_7 and mass reactance m. According to Özyörük et al. [67], although resistance and reactance can be accurately predicted when compared individually to experimental data, the model does not satisfy the stability criterion, and therefore both parts have to be simultaneously considered in the optimization routine. The vector of parameters is given by

$$\mathbf{x} = \{r_1, r_2, r_3, r_4, r_5, r_6, r_7\}. \tag{4.9}$$

and the upper and lower bounds are found in Table 4.3.

Notice that Equation 4.8 is not the only valid function. Özyörük et al. [67] combined filter type functions in such a way that it could fit the experimental results from a ceramic tubular liner. There is not guarantee that this function is still valid for the single degree of freedom liners investigated in this work (see Section 4.1). Nevertheless, this function is used in the multiple-frequency mode matching method.

Table 4.3 – Upper and lower bounds for the optimization variables using the EHR, rational function and multipole models.

Impedance model	Variable	Upper bound	Lower bound
EHR	R	1	0
	m	2×10^{-4}	0
	β_c	2	0
	T_l	2×10^{-4}	0
	ε	1	0
Rational function	r_1	1	0
	r_2	1×10^{3}	0
	r_3	1×10^{-2}	0
	r_4	1×10^{-2}	0
	r_5	1×10^{-2}	0
	r_6	1×10^{7}	0
	r_7	1×10^{-3}	0
Multipole	R	1	0
	m	1×10^{-3}	0
	C_1	1×10^{6}	0
	C_2	1×10^{6}	0
	$\Re(\tilde{C})$	0	-1×10^{6}
	$\Im(\tilde{C})$	0	-1×10^{6}
	$\Re(\tilde{\xi})$	1×10^{2}	0
	$\Im(\tilde{\xi})$	1×10^{3}	0

4.2.1.3 Multipole model

The multipole model was suggest by Reymen et al. [70] in order to use the recursive convolution for time domain simulations. However, the parameters had to be chosen carefully, otherwise passivity condition would not be satisfied [66]. Li et al. [66] improved the multipole model by rewriting it as a sum of residues and poles and adding the effective impedance model. Troian et al. [71] took a similar approach by including the resistance R from the effective impedance model to the multipole model. Still, the passivity condition can be violated and the coefficients must be checked.

The multipole model investigated here is given by a combination of Li et al. [66] and Troian et al. [71] models so that

$$Z(\omega) = R + i\omega m + \frac{C_1}{C_2 - i\omega} + \frac{\tilde{C}}{\tilde{\xi} - i\omega} + \frac{\tilde{C}^*}{\tilde{\xi}^* - i\omega}, \tag{4.10}$$

where $C_{1,2}$ are real positive coefficients, $\tilde{C}$ and $\tilde{\xi}$ are complex parameters and * denotes the complex conjugate. Therefore, the vector of parameters is given by

$$\mathbf{x} = \left\{R, m, C_1, C_2, \tilde{C}, \tilde{\xi}\right\}, \tag{4.11}$$

and the upper and lower bounds, defined empirically, are found in Table 4.3.

4.2.2 Results and Discussion

In this section, the results using both the classical (no impedance model used) and multiple-frequency mode matching methods are shown. Data for upstream and downstream acoustic sources are available, thus both results are shown independently.

Results for liner A are shown in Figure 4.7 for upstream source position. At no flow condition and Mach 0.10 the multiple-frequency mode matching method results in a smooth curve with same trend from the single-frequency mode matching. Therefore, it can be considered that the improved technique gives better results when the single-frequency mode matching method fails to find the correct impedance due to a bad initial guess, poor optimization at low frequencies or when the results start to deviate from the trend, as seen at frequencies around 2200 Hz for instance.

At higher Mach numbers the methods show good agreement above 1000 Hz between all impedance models and the single-frequency mode matching, but some discrepancies can be observed below this frequency, specially the reactance. In the EHR model, as $\omega \to 0$, then $\mathrm{Im}\left(Z_\mathrm{w}\right) \to 0$, and therefore the curve is forced to deviate from the trend found in the single-frequency mode matching method. This is not the case for the multipole model, which can follow the trend in the reactance found using the single-frequency mode matching.

In general, the differences between the impedance models and the single-frequency mode matching occur at low frequencies, which are usually out of the range of interest. There is a good agreement overall above 1000 Hz, including the frequency of maximum attenuation in the test rig. Any impedance model can be used in the multiple-frequency mode matching without any significant difference, specially above 1500 Hz, even at Mach 0.25.

Figure 4.8 shows the results for downstream acoustic source. Overall, the level of agreement is very similar to the upstream condi-

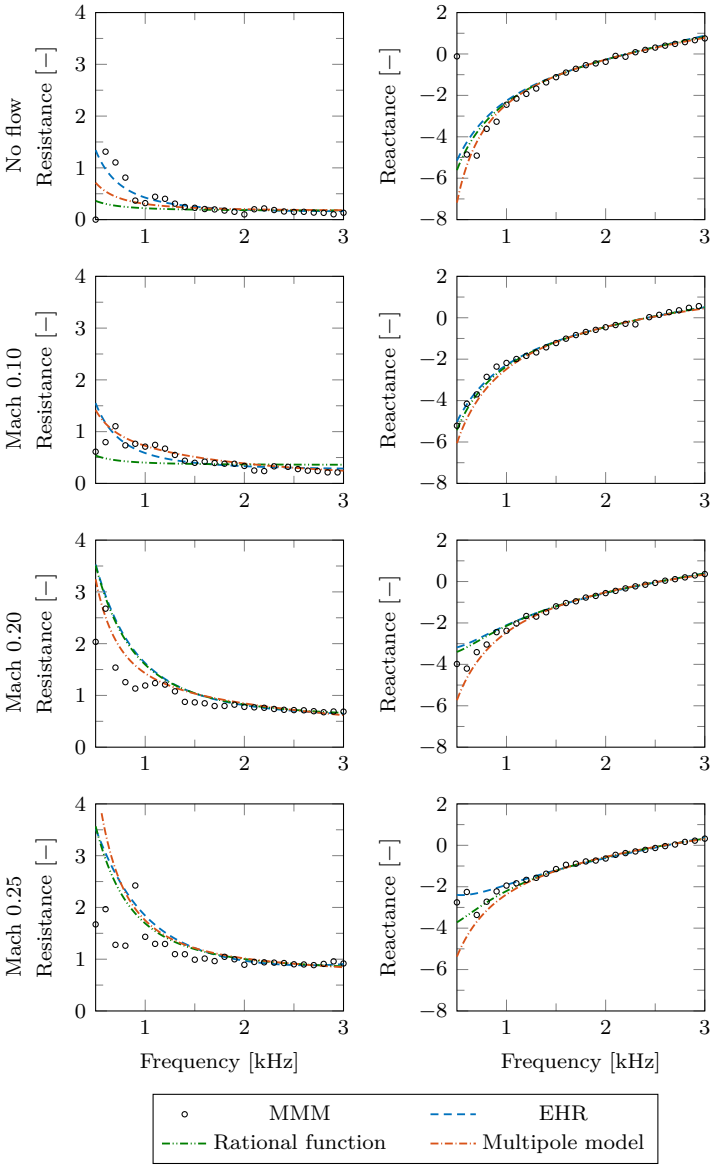

Figure 4.7 – Impedance eduction result for liner A and upstream acoustic source using the mode matching method and the modified technique.

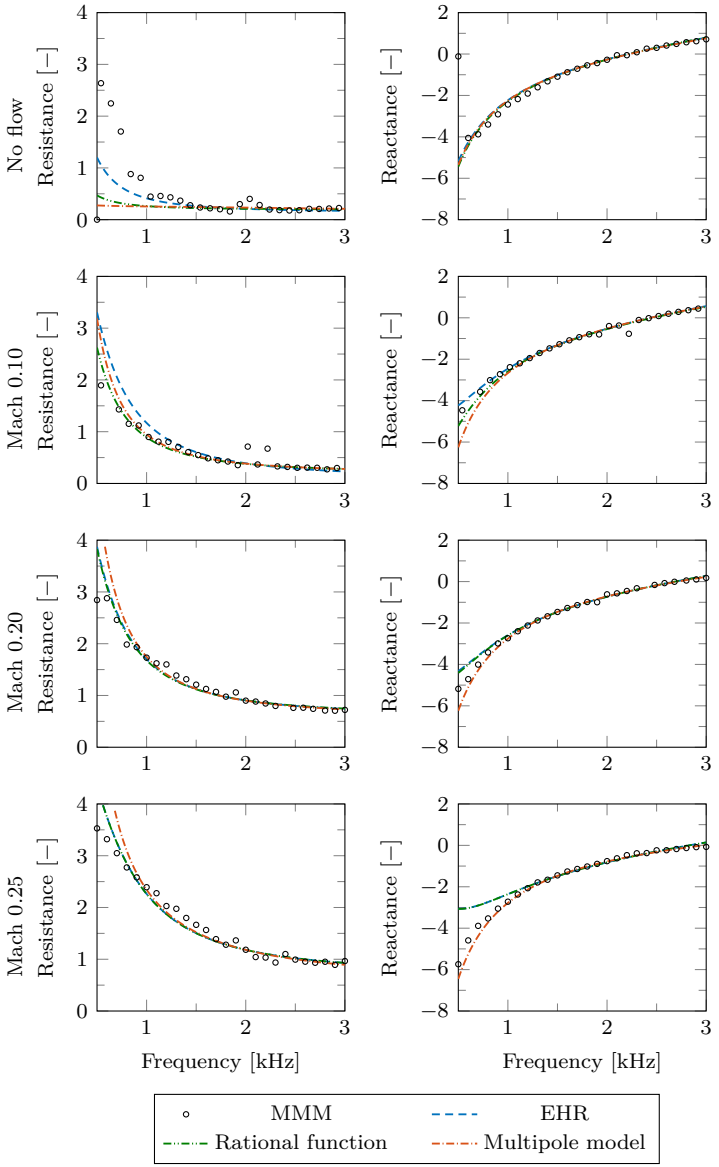

Figure 4.8 – Impedance eduction result for liner A and downstream acoustic source using the mode matching method and the modified technique.

tion. However, the instabilities in the results obtained with the single-frequency method may occur in different frequencies. At no flow condition, the single-frequency mode matching method overpredicts the resistance at low frequencies when compared to the multiple-frequency mode matching method, independent of the impedance model chosen. This is expected to be due to the low liner attenuation at this frequency range.

At Mach 0.10, the multiple-frequency mode matching method improves the results around 1900 Hz and 2300 Hz as some scattering can be seen in the single-frequency mode matching. This frequency range is close to the liner resonance frequency i.e. the frequency when the liner has the highest attenuation, as previously mentioned. In this frequency range the sound wave amplitude after the liner is considerable lower and may be close to the flow noise, resulting in a low signal-to-noise ratio. This situation is aggravated for upstream propagating wave (downstream acoustic source) as the propagation velocity relative to the liner is lower than in the downstream propagating wave case, thus acoustic dissipation is higher.

At Mach 0.20 there is a very good agreement over all frequencies, while at Mach 0.25 the reactance at low frequency shows the same behaviour as in the upstream acoustic source situation, which could be a limitation of the EHR and rational function models, although the resistance is well predicted.

The single-frequency mode matching results for liner B, as seen in Figures 4.9 and 4.10, highlight the advantages of including an impedance model in the optimization routine. In several frequencies over all Mach numbers the impedance found is clearly not consistent with the trend and cannot represent a physical behaviour of the liner.

For the upstream acoustic source (Figure 4.9), at no flow condition a good agreement can be seen for the reactance, whereas the resistance is underpredicted at low frequency in the multiple-frequency mode matching when compared to the single-frequency mode matching method. At Mach 0.10 both curves show the same trend. Some substantial scattering can be seen at Mach 0.20 along the whole frequency range, but the multiple-frequency mode matching results in a smooth curve as a clear example of the advantage of this method. At Mach 0.25 the reactance shows the same behaviour as seen for liner A, and both methods show different results at low frequencies due to the mathematical approach of each model.

In the downstream acoustic source condition, a very similar analysis to liner A can be carried out. At no flow condition, a good agreement

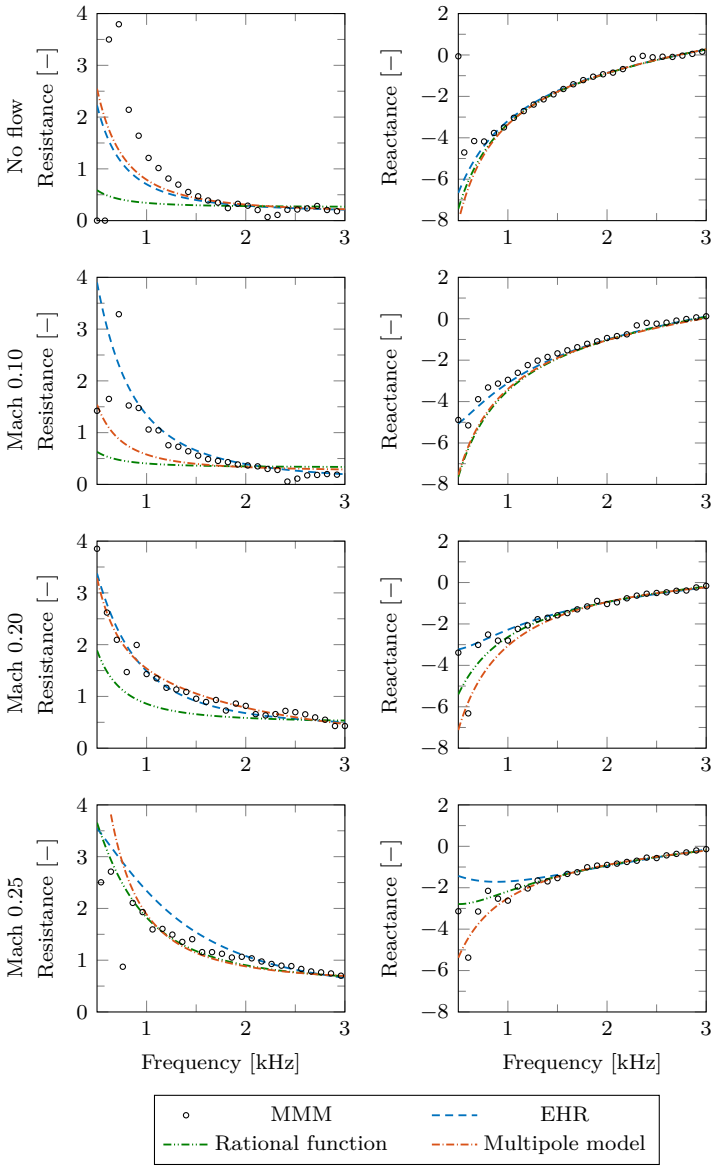

Figure 4.9 – Impedance eduction result for liner B and upstream acoustic source using the mode matching method and the modified technique.

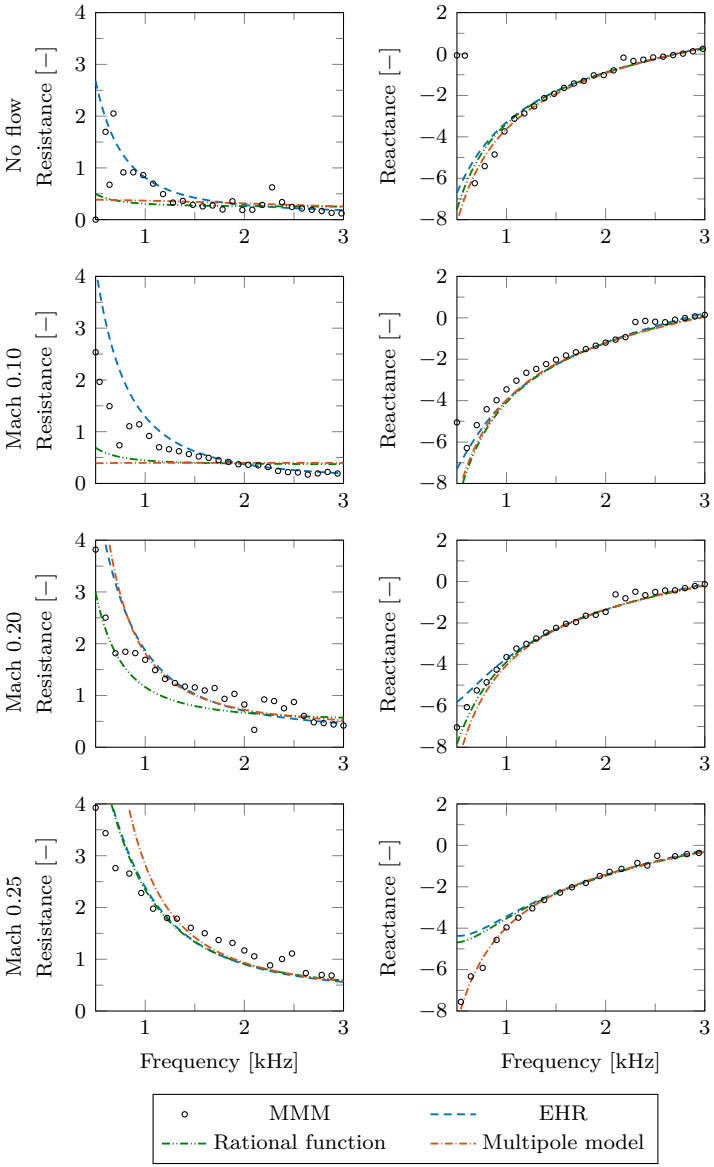

Figure 4.10 – Impedance eduction result for liner B and downstream acoustic source using the mode matching method and the modified technique.

is seen between both methods. Some deviations from the trend around 2300 Hz are seen in the single-frequency mode matching, whereas the multiple-frequency mode matching provides smooth impedance curves. At Mach 0.10 and 0.20 a good agreement is seen overall, which allows to correct the impedance found in the single-frequency mode matching between 2000 Hz and 2500 Hz. Likewise liner A this is the frequency range around the liner resonance frequency, therefore experimental data is not entirely reliable at these frequencies. This reinforces the advantage of using the multiple-frequency mode matching to find the correct impedance. At Mach 0.25 the reactance at low frequency shows again different behaviours on both methods.

4.3 Alternative boundary conditions

In this section, the effect of boundary conditions on the impedance results are investigated. One of the main issues lies on assumptions such as the Ingard-Myers boundary condition [28, 29] and uniform flow profile. Most of the impedance eduction techniques make use of the Ingard-Myers boundary condition. However, different boundary conditions can be applied in the presence of uniform flow[3], such as the proposal of Brambley [31], Rienstra and Darau [32] and Renou and Aurégan [45]. If the flow profile is known, the Pridmore-Brown equation can be solved to yield an exact solution at the lined wall.

The Ingard-Myers boundary condition was the first attempt to handle grazing flow effects by collapsing the boundary layer. However, over the past years, this assumption has shown to lead to time domain instabilities [72] and differences between the measured impedance using downstream and upstream propagating waves [13, 45, 73]. The first issue is related to numerical simulations, whereas the latter has several implications, such as erroneous calibration of predictive models and incorrect impedance used in aeroacoustic simulations. One could argue that such numerical models also use the Ingard-Myers boundary condition, and therefore the errors from experimental and numerical data would be mutually cancelled. However, this analysis is outside the scope of this work. Some attempts have been made to improve this boundary condition. Rienstra [32] and Brambley [31] included a small but finite boundary layer thickness in the mathematical formulation, whereas Renou and Aurégan [45] introduced a factor in the classical

[3] In other words, the propagation medium is uniform. Any boundary layer effects are included in the boundary condition.

Ingard-Myers boundary condition. Such representations have improved experimental results [45, 73] and model accuracy when compared to an exact solution of the boundary layer [74].

The aim of this section is to compare the more recent boundary conditions, such as the proposal of Brambley [31], to the Ingard-Myers boundary condition, in the context of impedance eduction techniques, more specifically in the MMM [42]. The modified Ingard-Myers boundary condition, as proposed by Renou and Aurégan [45], makes use of upstream and downstream results. However, differences between both results may be inherent to the liner behaviour in the presence of flow [52], and thus this approach is not considered here. Rienstra and Darau boundary condition [32] is asymptotically equivalent to Brambley's and thus it has been excluded from this analysis. The exact solution by means of the Pridmore-Brown equation is also investigated, but applied to the SFM, based on Jing's approach [44].

4.3.1 Ingard-Myers boundary condition

The Ingard-Myers boundary condition [29] collapses the boundary layer by assuming acoustic displacement continuity across a vortex sheet over the liner surface, such that at $x = 0$

$$-u = \frac{1}{i\omega Z}\left(i\omega + U\frac{\partial}{\partial z}\right)p. \tag{4.12}$$

Introducing Equation 4.12 into Euler equation in x-direction leads to

$$\frac{\partial p}{\partial x} = -\rho\left(i\omega + U\frac{\partial}{\partial z}\right)u. \tag{4.13}$$

Assuming a pressure field as given by Equation 2.13 and applying the hard wall boundary condition given by

$$\left.\frac{\partial p}{\partial x}\right|_{x=b} = 0, \tag{4.14}$$

the following relation is found

$$k_x \tan\left(k_x b\right) = \frac{i}{kZ}\left(k - Mk_z\right)^2, \tag{4.15}$$

where Z is the normalized wall impedance. The complete derivation is given in Appendix A.

4.3.2 Brambley boundary condition

Brambley [31] proposed an alternative boundary condition by introducing a small but finite boundary layer δ. Using an asymptotic expansion and retaining the leading order terms the following equation is derived [31]:

$$-v\left[Z-\frac{i}{k}\left(k-Mk_z\right)^2\delta I_0\right]=\left[\frac{k-Mk_z}{k}-Z\frac{\delta I_1 k_z^2}{i\left(k-Mk_z\right)}\right]p, \quad (4.16)$$

where the coefficients δI_0 and δI_1 are given by

$$\delta I_0=\int_0^\delta 1-\frac{\left(k-M_0(x)k_z\right)^2}{\left(k-Mk_z\right)^2}dx, \quad (4.17)$$

$$\delta I_1=\int_0^\delta 1-\frac{\left(k-Mk_z\right)^2}{\left(k-M_0(x)k_z\right)^2}dx. \quad (4.18)$$

The former may be interpreted as a correction to the impedance as seen by the acoustic field in the presence of a uniform velocity profile, turning into an "effective" impedance. The latter is responsible for the wellposedness of the boundary condition. In both equations it was assumed a constant density across the boundary layer. Repeating the procedure shown for the Ingard-Myers boundary condition, the following relation is derived

$$k_x\tan\left(k_x b\right)=\frac{i\left(k-Mk_z\right)^2-kZ\delta I_1 k_z^2}{kZ-i\left(k-Mk_z\right)^2\delta I_0}. \quad (4.19)$$

Notice that, if $\delta I_0=\delta I_1=0$, the Ingard-Myers boundary condition is recovered. Assuming a constant density and a linear velocity profile in the boundary layer,

$$\delta I_0=\frac{\delta Mk_z\left(2Mk_z-3k\right)}{3\left(Mk_z-k\right)^2}, \qquad \delta I_1=\delta M\frac{k_z}{k} \quad (4.20)$$

Gabard has shown a small effect on changing the boundary layer profile, i.e. quadratic, power law, etc, on the absorption coefficient of the sur-

face, as long the displacement thickness remains constant [74], and thus the linear profile was chosen here for the sake of simplicity. A boundary layer thickness of 25 % relative to half of the duct height was chosen, representing the strongly sheared flow in the test rig. Although relatively thick, $k\delta$ is small for most of the frequency range under analysis, which is a basic assumption in Brambley's derivation.

4.3.3 Exact solution for the impedance boundary condition with flow

The previous boundary conditions are based on uniform flow assumption. However, test rigs are usually of small duct cross section, and therefore the flow is strongly sheared. A better approach is to include the flow profile in the governing equation. In this case, the Pridmore-Brown equation for bi-dimensional rectangular ducts can be considered and is given by [54]

$$\frac{d^2p}{dx^2} + \frac{2k_z}{k - M(x)k_z}\frac{dM}{dx}\frac{dp}{dx} + \left[(k - M(x)k_z)^2 - k_z^2\right]p = 0, \qquad (4.21)$$

where the flow profile $M(x)$ can be selected based on curve fitting to experimental data. This formulation is relatively easy to include in the SFM and the following procedure was proposed by Jing [44]. Once the axial wave number is known by means of Prony's method, the Pridmore-Brown equation can be numerically integrated. Firstly, it is rewritten as a pair of first order differential equations,

$$\begin{cases} \dfrac{dF}{dX} = G \\ \dfrac{dG}{dX} = -\dfrac{2k_z}{k - M(X)k_z}\dfrac{dM}{dX}G - \left[(k - M(X)k_z)^2 - k_z^2\right]F \end{cases} \qquad (4.22)$$

where $X = x/b$, F is the non-dimensional acoustic pressure and G is proportional to the acoustic particle velocity. The boundary conditions are given as follows. At the hard wall, the acoustic particle velocity is zero, thus $G(1) = 0$, whereas the pressure is an arbitrary constant, for instance $F(1) = 1$. At the lined wall, the no-slip boundary condition is applied,

$$G(0) = \frac{ik}{Z}F(0) \qquad (4.23)$$

Equation 4.22 is numerically integrated by means of a fourth-order Runge-Kutta scheme, and thus the unknown impedance can be found.

The implementation is discussed in detail in Chapter 6.

4.3.4 Results and discussion

This section is divided into two parts. The first shows the results for the MMM using the Ingard-Myers boundary condition [28, 29] and Brambley boundary condition [31]. Results for both downstream and upstream propagating waves are shown since there is a noticeable difference between the results. The second part is dedicated to the SFM using the classical Ingard-Myers boundary condition [28, 29] and the exact solution given by the Pridmore-Brown equation [54]. Again, both downstream and upstream propagating waves are analysed.

4.3.4.1 Mode matching method

Figure 4.11 shows the results. In general, the attenuation from 0.5 kHz to 1.0 kHz is very low, and the MMM finds difficulty to correctly estimate the liner impedance. This is aggravated for downstream propagating waves, when the attenuation is even lower, and high flow velocities, e.g. $M = 0.28$. Therefore, the results are very unstable in this frequency range. Nevertheless, some conclusions may be drawn from the comparison between boundary conditions, even at low frequencies.

Regarding the effect of the boundary conditions, Figure 4.11 shows some interesting trends. At $M = 0.10$, both the resistance and reactance are very similar regardless the boundary condition and the wave orientation. As flow velocity increases, and assuming the Ingard-Myers boundary condition, the resistance becomes significantly higher for the upstream propagating wave when compared to the downstream propagating wave. A difference between both cases is also seen in the reactance, the upstream result being lower than the downstream result. When the Brambley boundary condition is applied, the difference between the curves is reduced, but discrepancies can still be observed.

The reactance is related to the cell cavity, so it is expected a minor effect of propagation direction. In other words, the wave orientation should not affect the reactance, at least in the frequency range here considered. On the other side, the resistance shows a slight difference between both cases, although the Brambley boundary condition shows an improvement by reducing the difference between downstream

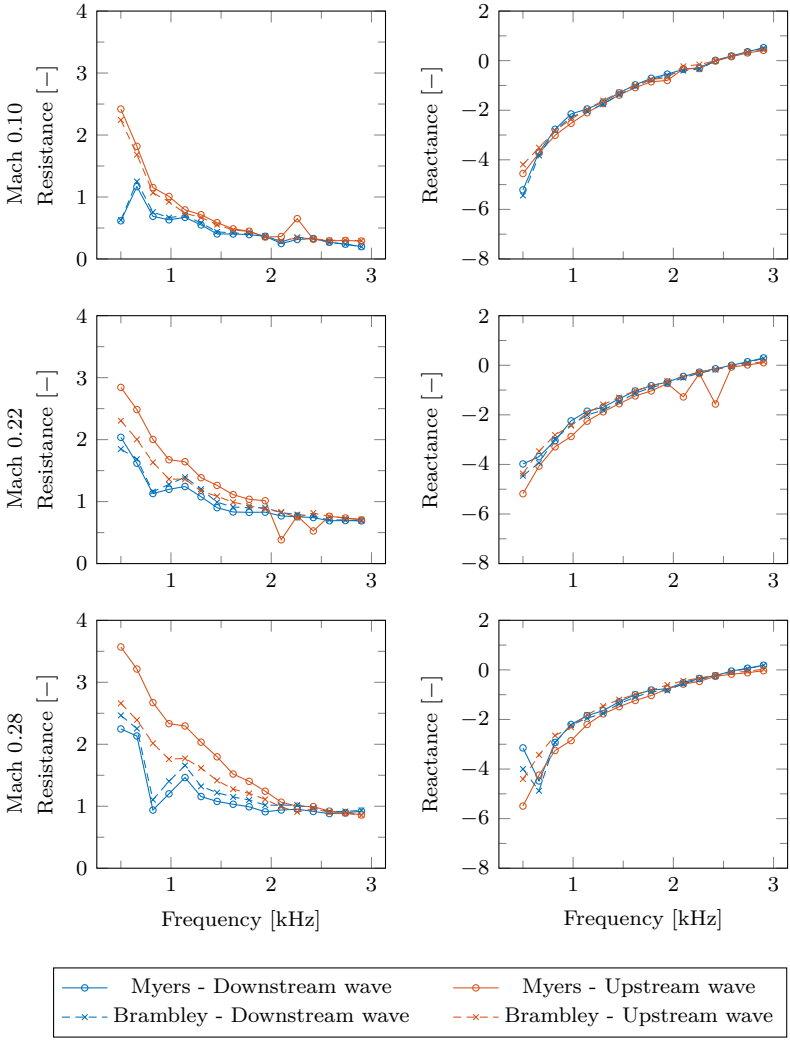

Figure 4.11 – Impedance eduction result for liner A at different flow velocities using the mode matching method and uniform flow assumption with Ingard-Myers and Brambley boundary conditions.

and upstream results. Since the acoustic wave is subject to vortex shedding and turbulence generated at the perforated plate, the resistance may be different for upstream and downstream propagating waves.

In contrast to liner A, where a good signal-to-noise ratio was achieved for most of the frequency range, liner B has a very high attenuation between 2.2 kHz and 2.7 kHz, such that the microphones after the liner (or before, depending on the source location) are measuring flow-induced noise rather than an attenuated sound wave. As a consequence, the results shown in Figure 4.12 are oscillating around this frequency. Nevertheless, the same trends from liner A are observed, i.e. the Brambley boundary condition reduces the difference between upstream/downstream educed resistances. However, both results are also similar when applying the Ingard-Myers boundary condition, such that the dissipation mechanism may be similar for upstream and downstream propagating waves when considering this liner geometry.

Regarding the reactance, a collapse of the curves is also not achieved when applying the Brambley boundary condition, even though the difference is reduced. A possible reason for this is the large hole diameter of test sample B compared to its plate thickness ($\tau/d = 0.4$), such that the air in the honeycomb cell is affected by turbulence and vortex shedding generated at the hole, thus affecting the reactance.

In general, the educed impedance is affected by the boundary condition chosen in the acoustic field modelling. Brambley boundary condition is more representative of the actual flow profile in the test rig when compared to the Ingard-Myers boundary condition. However, differences can still be observed regarding upstream and downstream propagating waves in the educed impedance. It is expected that a fully resolved flow profile by means of the Pridmore-Brown equation may increase the accuracy of the impedance eduction result.

4.3.4.2 Straightforward method

Figure 4.13 shows the results for the SFM considering uniform flow assumption with Ingard-Myers boundary condition and shear flow assumption. Under the assumption of uniform flow, the educed impedance from upstream and downstream measurements shows a significant difference, specially in the frequency range from 1.0 kHz to 1.5 kHz and high flow velocities, i.e. $M \geq 0.20$.

By considering the flow profile, a better agreement between upstream and downstream curves is obtained, mainly for the reactance

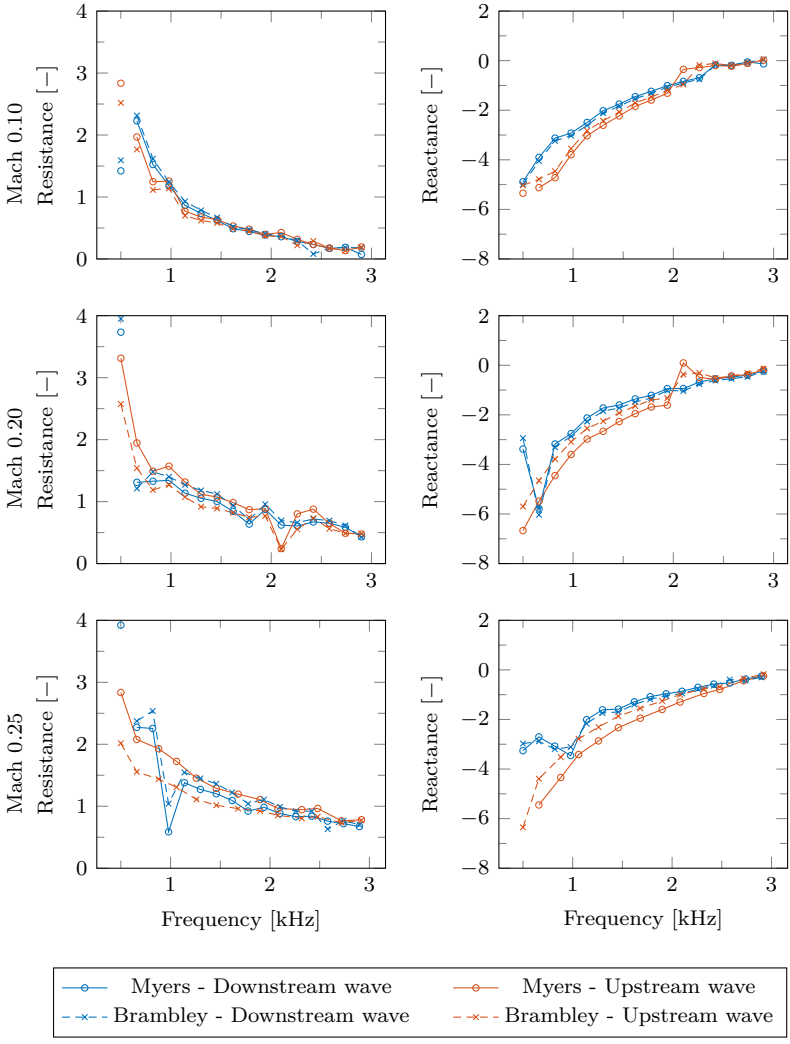

Figure 4.12 – Impedance eduction result for liner B at different flow velocities using the mode matching method and uniform flow assumption with Ingard-Myers and Brambley boundary conditions.

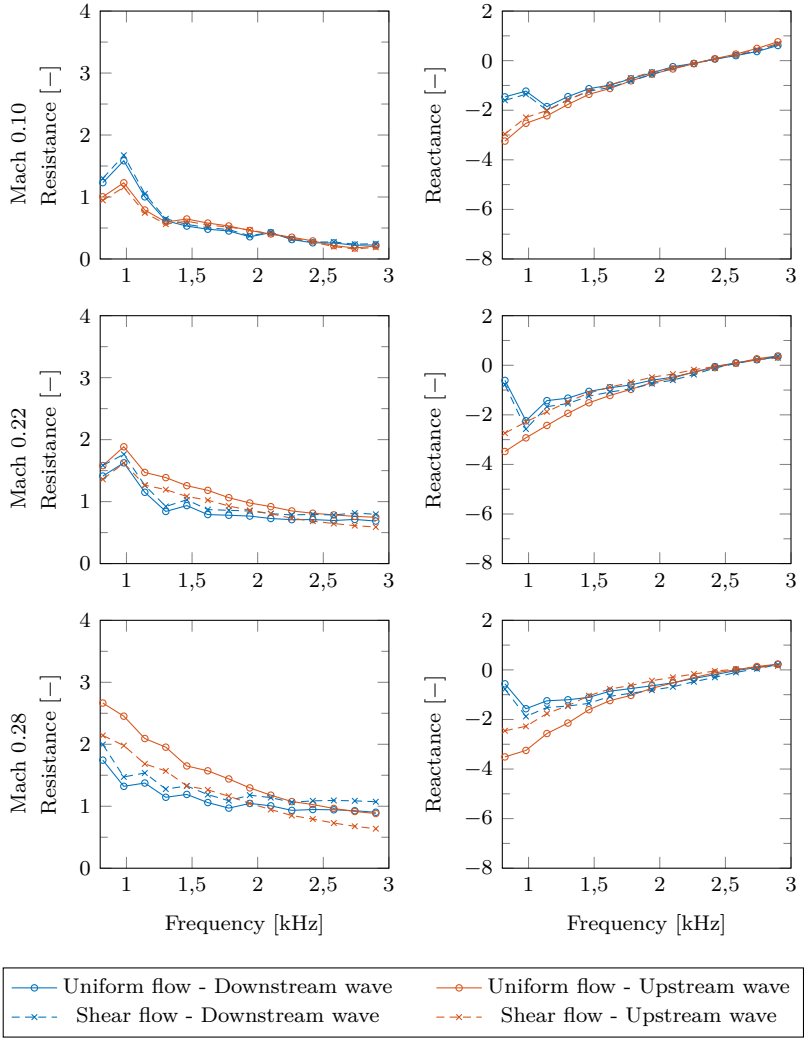

Figure 4.13 – Impedance eduction result for liner A at different flow velocities using the straightforward method with uniform and shear flow assumptions.

(although some differences are still present). An interesting trend is observed for the resistance. The downstream results are almost constant in the frequency range under analysis, but the upstream results show a decrease with frequency, regardless the flow profile assumption. Once more, this behaviour may be related to the underlying physics of the liner, and not to flaws in the impedance eduction technique. Therefore, a collapse of the curves may not be achievable.

As stated in the previous section, liner B shows a very high attenuation, an just as the MMM results, the SFM results are also affected due to flow-induced noise measurements. As a consequence, the number of microphones used in the post-processing is reduced, and unexpected oscillations in the curves from Figure 4.14 are observed, which could be related to spurious results from Prony's method.

Regarding the modifications in the impedance eduction, the resistance is slightly affected by the shear flow assumption, but the biggest difference is seen for the reactance, where the upstream and downstream curves are closer. Once again, the remaining difference may be related to the flow field inside the hole, which, as a result of the small ratio between hole diameter and plate thickness, affects the air in the honeycomb cell, and consequently the liner reactance.

The final conclusion is that a fully resolved flow profile is not sufficient to collapse the upstream/downstream impedance curves. Of course, the Pridmore-Brown equation is limited to its main assumptions, for instance by neglecting viscous and thermal effects, which may play an important role in acoustic dissipation at the hole internal walls. Also, turbulent mixing may be necessary to fully represent the acoustic propagating in the test rig. Finally, a locally reacting impedance may not be a feasible representation of the acoustic liner, such that extended reaction models should be investigated.

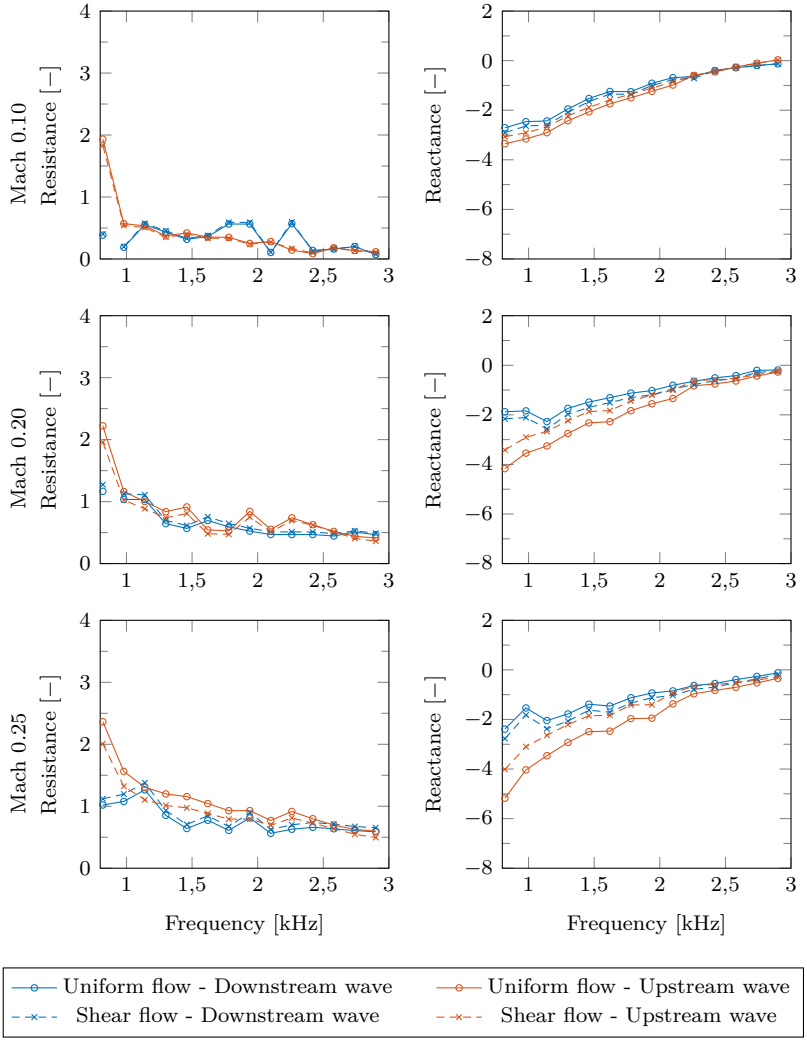

Figure 4.14 – Impedance eduction result for liner B at different flow velocities using the straightforward method with uniform and shear flow assumptions.

5 OPTIMAL IMPEDANCE IN CIRCULAR DUCTS

Once the liner impedance can be related to the liner geometry by means of predictive models or experimental characterization, one may wonder which impedance gives the maximum attenuation in lined ducts. This is particularly important in aero-engines due to space restrictions, although the concept may be extended to other applications, such as ventilation systems for instance.

Of course, this is not a trivial task due to: (i) duct geometry and (ii) presence of flow. As it will be seen, for each pair of modes (mn) propagating in a lined duct, there is a locally reacting wall impedance Z which will give the maximum modal decay rate, the so-called optimal impedance.

Cremer [75] was the first to demonstrate how to calculate the optimal impedance for the least attenuated mode[1] in a rectangular duct in the absence of flow. At the optimal impedance, for a given azimuthal order m, two different modes of radial order n coalesce.

However, it depends on the nature of the acoustic source, and there is no guarantee that the least attenuated mode is in fact the one with highest acoustic energy content. Aero-engines are a classical example of this behaviour, justifying a more elaborated study. Based on these arguments, Tester [76] expanded the analysis to higher order modes in rectangular ducts and uniform flow effects as well. In the case of circular ducts, the derivation of the optimal impedance is shown only for the plane wave mode $(0, 1)$, and no special consideration is given regarding the presence of uniform flow.

In this chapter, the optimal impedance in circular ducts is expanded to higher order modes and the presence of uniform flow. The last section is dedicated to examples of optimal impedance in a typical modern turbofan aero-engine.

It is convenient to first introduce the following non-dimensional variables:

$$\varpi = ak, \tag{5.1}$$

$$\alpha = ak_r, \tag{5.2}$$

$$\kappa = ak_z, \tag{5.3}$$

[1] In other words, the least attenuated mode is the one with lowest $\Im(k_z^{(mn)})$. In general, modal decay rate grows with mode order, such that the first modes are the dominant ones, and therefore they carry more acoustic energy.

where a is the duct radius. Notice that, in this convention, ϖ is the Helmholtz number.

5.1 In the absence of flow

In a circular duct with a locally reacting wall impedance $Z(\omega)$, the wave numbers are eigenvalues of the equation:

$$\frac{J_m(\alpha)}{\alpha J'_m(\alpha)} = \frac{iZ}{\varpi}. \tag{5.4}$$

Tester [76] demonstrated how to calculate the optimal impedance for $m = 0$. However, higher order modes are present in aero-engines, and therefore this derivation has to include any m-th mode order. Following Cremer's definition [75], the optimal impedance occurs at the ramification point of this equation, such that

$$\frac{d}{d\alpha}\left(\frac{J_m(\alpha)}{\alpha J'_m(\alpha)}\right) = 0. \tag{5.5}$$

which leads to [77]

$$J'_m(\alpha)^2 + \left(1 - \frac{m^2}{\alpha^2}\right) J_m(\alpha)^2 = 0. \tag{5.6}$$

A full derivation is given in Appendix B, and only the final expression is shown here for the sake of brevity. This equation admits multiple solutions, each α representing an optimal radial wave number for a given azimuthal order m. In other words, for each α, two different modes of radial order n coalesce. Usually, the first two radial modes have the highest acoustic energy content, but the analysis can be extended to any pair of modes. In order to clearly define which modes coalesce, the auxiliary radial mode order υ is introduced. Thus, $n\upsilon = 12$ indicates that first and second radial modes coalesce, and so on.

As a mathematical exercise, for $m = 0$, Equation 5.6 returns

$$J_1(\alpha)^2 = -J_0(\alpha)^2, \tag{5.7}$$

or

$$J_1(\alpha) = iJ_0(\alpha), \tag{5.8}$$

which recovers Eq. (50) from Tester [76]. Therefore, the optimal im-

pedance is given by

$$Z_{\text{opt}}^{(mn\upsilon)} = -i\varpi \frac{J_m(\alpha_{mn\upsilon})}{\alpha_{mn\upsilon} J'_m(\alpha_{mn\upsilon})}. \tag{5.9}$$

Notice that the optimal impedance is not only function of the mode order (mn), but also of the wave frequency k and duct radius a. Thus, a more convenient form of writing the optimal impedance is

$$Z_{\text{opt}}^{(mn\upsilon)} = \varpi K^{(mn\upsilon)}, \tag{5.10}$$

where $K^{(mn\upsilon)}$ is a constant value given by

$$K^{(mn\upsilon)} = -i \frac{J_m(\alpha_{mn\upsilon})}{\alpha_{mn\upsilon} J'_m(\alpha_{mn\upsilon})}, \tag{5.11}$$

and summarized in Table 5.1. As the mode order m increases, $K^{(mn\upsilon)}$ gets smaller, and the difference between consecutive azimuthal mode orders is less perceptible. The results are shown for m from 0 to 10, and at some specific values, for instance $m = 16$, 24 and 30, which could be related to the number of blades in a turbofan aero-engine, and therefore the rotor-locked acoustic mode.

It is interesting to note the impact of the optimal impedance in the axial wave number. As seen in Equation 5.4, there are an infinite number of radial wave numbers, related to the axial wave number by

$$\kappa_{\pm}^{(mn)} = \pm\sqrt{\varpi^2 - \alpha_{mn}^2}, \tag{5.12}$$

where the indexes + and − indicate right- and left-running modes, respectively. In the case of $Z \to \infty$ (rigid wall), the axial wave numbers κ are purely real or imaginary. The former means that the acoustic mode propagates along the duct, whereas the latter indicates that the acoustic mode decay exponentially along the duct[2]. Figure 5.1 illustrates this situation. For the case of $\varpi = 5$ and $m = 0$, the first two radial modes propagate (cut-on modes) and their wave numbers are located along the real axis. The other modes are evanescent (cut-off modes) and their wave numbers are located along to the imaginary axis. Therefore, at a sufficiently distance large from the source, only the first two modes compose the acoustic field.

Now consider a wall with resistance $\Re(Z) = 2$. This value is still above the optimal resistance for any pair of modes when $m = 0$ and

[2]Also called evanescent modes.

Table 5.1 – Optimal constant $K^{(mnv)}$.

Mode order	$nv = 12$	$nv = 13$
$m = 0$	$0.2833 - i0.1216$	$0.1515 - i0.0397$
$m = 1$	$0.2049 - i0.0705$	$0.1245 - i0.0284$
$m = 2$	$0.1663 - i0.0513$	$0.1076 - i0.0225$
$m = 3$	$0.1424 - i0.0411$	$0.0957 - i0.0188$
$m = 4$	$0.1259 - i0.0347$	$0.0868 - i0.0162$
$m = 5$	$0.1136 - i0.0302$	$0.0798 - i0.0144$
$m = 6$	$0.1040 - i0.0269$	$0.0741 - i0.0129$
$m = 7$	$0.0963 - i0.0243$	$0.0694 - i0.0118$
$m = 8$	$0.0899 - i0.0223$	$0.0654 - i0.0109$
$m = 9$	$0.0845 - i0.0206$	$0.0620 - i0.0101$
$m = 10$	$0.0799 - i0.0192$	$0.0590 - i0.0095$
$\vdots$	$\vdots$	$\vdots$
$m = 16$	$0.0615 - i0.0140$	$0.0466 - i0.0070$
$\vdots$	$\vdots$	$\vdots$
$m = 24$	$0.0485 - i0.0106$	$0.0374 - i0.0053$
$\vdots$	$\vdots$	$\vdots$
$m = 30$	$0.0424 - i0.0091$	$0.0330 - i0.0046$

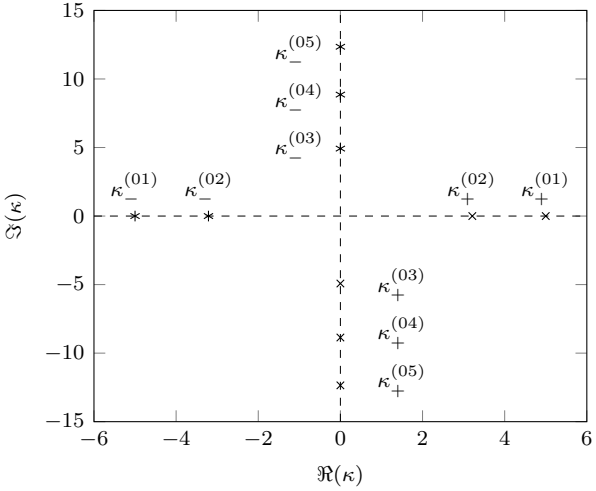

Figure 5.1 – Wave numbers κ at $m = 0$, $\varpi = 5$ and hard wall condition for different radial orders n.

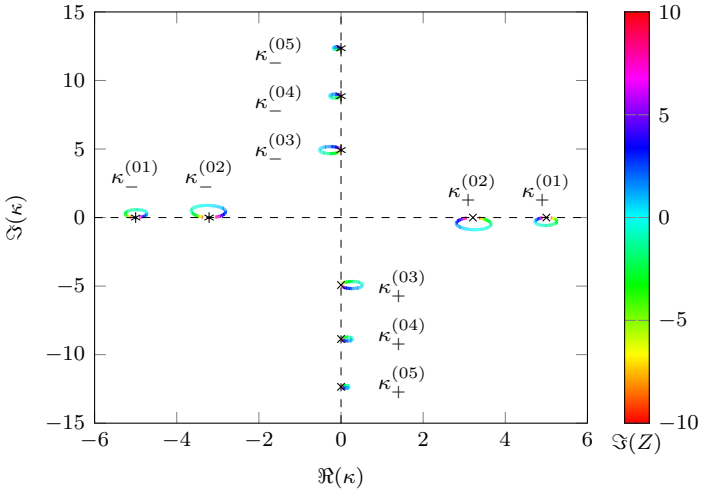

Figure 5.2 – Wave numbers κ at $m = 0$, $\varpi = 5$ and $\Re(Z) = 2$ for different radial orders n.

$\varpi = 5$,

$$\Re(Z_{\text{opt}}^{(012)}) = \Re\left(\varpi K^{(012)}\right) = 1.4165. \tag{5.13}$$

The presence of a wall impedance results in complex eigenvalues in Equation 5.4, so that the wave numbers are launched in the complex plane, as seen in Figure 5.2. At $\Im(Z) \to -\infty$ and $+\infty$ the wave numbers return to their rigid wall values.

If resistance is below the optimal impedance for the mode (01) (e.g. $\Re(Z) = 1$), then the analysis is not so straightforward. As the reactance increases, the axial wave number $\kappa^{(01)}$ is launched into the complex plane. Figure 5.3 shows that, at some value of reactance, the axial wave number returns close to the real axis as $\kappa^{(02)}$, The same occurs with $\kappa^{(02)}$ (when $\Im(Z) \to -\infty$), that returns as $\kappa^{(01)}$ at $\Im(Z) \to +\infty$. When both real and imaginary parts of the axial wave number are high, the acoustic mode is considered a surface wave, whose maximum value is located at the wall and decay exponentially within the radial direction [78].

The behaviour of the wave numbers $\kappa^{(01)}$ and $\kappa^{(02)}$ are very different when $\Re(Z) = 2$ and $\Re(Z) = 1$, so at some resistance value their paths touch each other, as seen in Figure 5.4. This happens

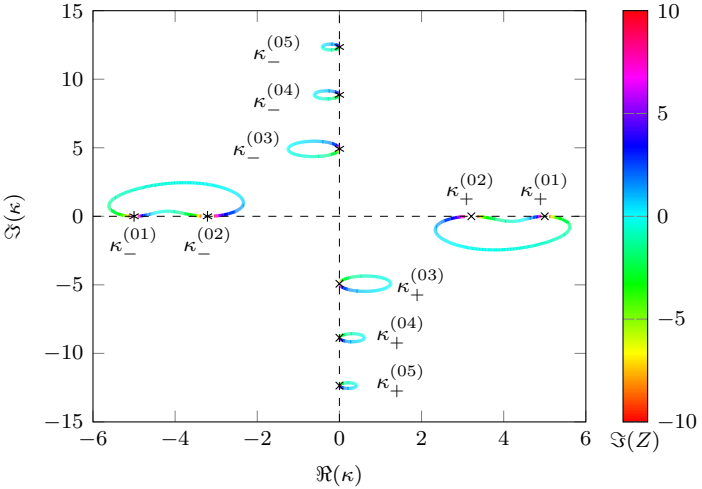

Figure 5.3 – Wave numbers κ at $m = 0$, $\varpi = 5$ and $\Re(Z) = 1$ for different radial orders n.

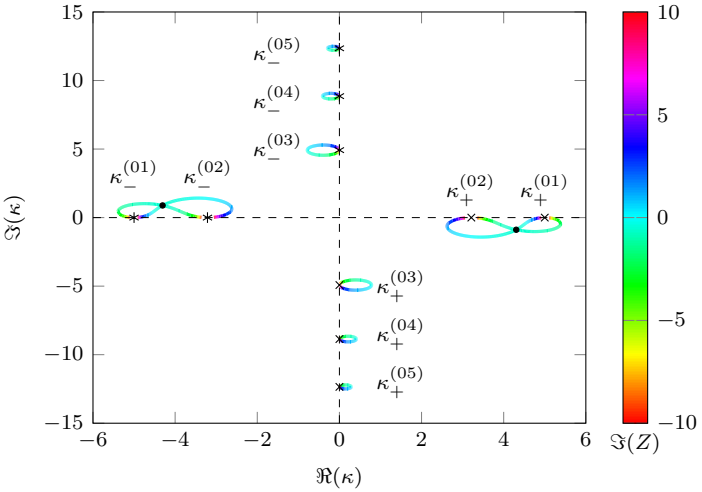

Figure 5.4 – Wave numbers κ at $m = 0$, $\varpi = 5$ and $\Re(Z) = 1.4165$ for different radial orders n.

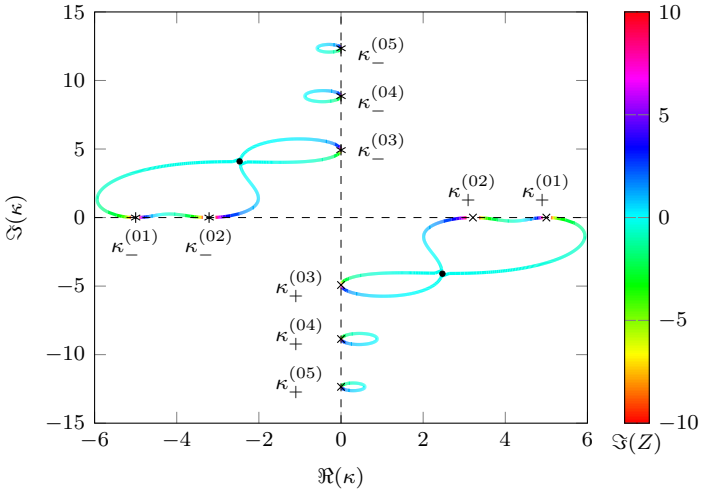

Figure 5.5 – Wave numbers κ at $m = 0$, $\varpi = 5$ and $\Re(Z) = 0.7575$ for different radial orders n.

exactly at the optimal impedance, in this case $Z = 1.4165 - i0.6048$. At this point, there is no distinction between the wave numbers from modes $(0, 1)$ and $(0, 2)$. In a certain way, it is the optimal impedance for a pair of modes. Figure 5.5 complements this analysis, since the resistance is optimal for modes $(0, 1)$ and $(0, 3)$, and the trajectories of $\kappa^{(01)}$ and $\kappa^{(03)}$ meet at $\Im(Z) = -0.1986$. At higher azimuthal orders $m > 0$ the analysis is qualitatively the same, and hence it will not be shown here. In Section 5.3 some examples of optimal impedance for typical turbofan aero-engines are given, and therefore higher order modes are analysed. The next step is to include an uniform mean flow.

5.2 In the presence of mean flow

The optimal impedance found in the previous section is of little interest for aeronautical applications if not corrected to include the presence of flow. In this case, uniform flow is assumed together with the Ingard-Myers boundary condition [28, 29]. First, the Lorentz or

Prandtl-Glauert type transformation is introduced,

$$\beta = \sqrt{1 - M^2}, \tag{5.14}$$

$$\Omega = \frac{\varpi}{\beta}, \tag{5.15}$$

$$\gamma = \alpha \frac{\beta}{\varpi}, \tag{5.16}$$

$$\varphi^{\pm} = \pm\sqrt{1 - \gamma^2}, \tag{5.17}$$

where + indicates right-running modes and − indicates left-running modes. The sign choice of the reduced wave number $\varphi^{\pm}$ plays a major role [78] and more details are given in Appendix B. The wave numbers are now the eigenvalues of the following equation [78]:

$$(1 - M\varphi)^2 J_m(\alpha) = iZ\beta^3 \gamma J'_m(\alpha). \tag{5.18}$$

Tester [79] shows that, for rectangular ducts, the transversal wave number at the optimal impedance is approximately constant for any Mach number. Therefore, assuming that the optimal k_r remains constant for any flow velocity in a circular duct, the optimal impedance with uniform flow is given by the optimal impedance without flow corrected by a factor of $(1 + M)^2$, so

$$Z^{(mnv)}_{\text{opt},M} = \frac{Z^{(mnv)}_{\text{opt}}}{(1 + M)^2}, \tag{5.19}$$

where M takes positive values when the acoustic wave propagates downstream, and negative values when the acoustic wave propagates upstream. Notice that, in the first case, the flow reduces the absolute impedance value, whereas the latter increases it. Equation 5.19 must be used together with Equation 5.10 to calculate the optimal impedance in the presence of a mean flow.

Unfortunately, Equation 5.19 is not valid for circular ducts. To illustrate that, the following case is considered: $m = 1$, $M = 0.5$, $\varpi = 5$ and downstream propagating wave. The optimal resistance in the absence of flow is

$$\Re(Z^{(112)}_{\text{opt}}) = \Re\left(\varpi K^{(112)}\right) = 1.0245, \tag{5.20}$$

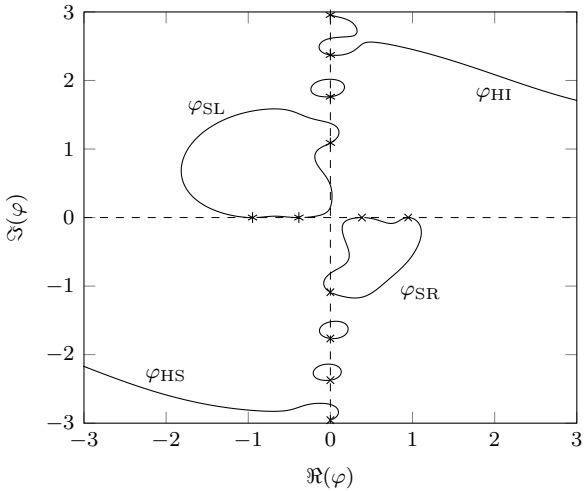

Figure 5.6 – Reduced axial wave numbers σ at $m = 1$, $\varpi = 5$ and $\Re(Z) = 0.4553$.

and, in the presence of flow,

$$\Re(Z^{(112)}_{\mathrm{opt},M}) = \frac{\Re(Z^{(112)}_{\mathrm{opt}})}{(1+M)^2} = 0.4553, \tag{5.21}$$

The reduced wave number behaviour is shown in Figure 5.6. There is no point of optimal impedance in the right-running modes, as seen in Figure 5.4. In fact, the three first modes have their indexes switched when the reactance goes from $+\infty$ to $-\infty$, and therefore, this value of resistance is below the optimal one. It is interesting to see two modes being launched into infinity in the upper and lower complex planes. According to Rienstra [78], these modes are classified as hydrodynamic modes (as they only exist with flow), and can be subdivided into stable and unstable modes, respectively HS and HI in Figure 5.6. The modes that temporarily change position with a neighbour by being launched into the complex plane are called acoustic surface waves, and can be divided into right- and left-running surface wave, respectively SR and SL in Figure 5.6. The behaviour and properties of these modes are of little interest in the context of optimal impedance in turbofan aero-engines and will not be further investigated.

In order to obtain the optimal impedance in circular ducts in the presence of uniform flow, the derivative to α of Equation 5.18 must vanish, so that

$$\frac{d}{d\alpha}\left[(1-M\varphi)^2\frac{J_m(\alpha)}{\alpha J'_m(\alpha)}\right]=0. \tag{5.22}$$

Once again, the full derivation is available in Appendix B. The final expression is given by

$$\frac{2M}{\varphi\Omega^2}\frac{J_m(\alpha)}{J'_m(\alpha)}+\frac{(1-M\varphi)}{\alpha J'_m(\alpha)^2}\left[J'_m(\alpha)^2+\left(1-\frac{m^2}{\alpha^2}\right)J_m(\alpha)^2\right]=0. \tag{5.23}$$

In fact, if $M=0$, Equation 5.6 is recovered. The optimal α_{mnv} is function not only of the Mach number, but also the source frequency ϖ, which is implicit in φ and Ω. To generate a list such as Table 5.1 is not a straightforward task, so that Equation 5.23 has to be solved for each case. Substituting Equation 5.23 into Equation 5.18, the optimum impedance with flow is given by

$$Z_{\text{opt}}^{(mnv)}=\frac{(1-M\varphi)^2J_m(\alpha)}{i\beta^3\gamma J'_m(\alpha)}. \tag{5.24}$$

For the previous example ($m=1$, $\varpi=5$ and $M=0.5$), it results in the following optimal impedance:

$$Z_{\text{opt},M=0.5}^{(112)}=0.7380+i0.0570. \tag{5.25}$$

In Figure 5.7, it is very clear that the new optimal impedance correctly predicts the point where the first and second mode coalesce in the presence of flow. The same analysis can be carried out for left-running modes. In this case, the optimal impedance is given by

$$Z_{\text{opt},M=-0.5}^{(112)}=3.0737-i1.7957, \tag{5.26}$$

and Figure 5.8 shows that it is indeed the correct optimal impedance.

The inclusion of boundary layer effects, and consequently acoustic refraction, may affect the radial wave numbers and lead to a different optimal impedance. Such situation should be relevant in ducts of small diameter, but not in aero-engines, where the boundary layer thickness is small compared to the inlet diameter. However, as shown in Chapter 6, even a small boundary layer thickness can affect the sound attenuation (e.g. less than 1 %), such that the optimal impedance for uniform flows is no longer the optimal impedance for sheared flows.

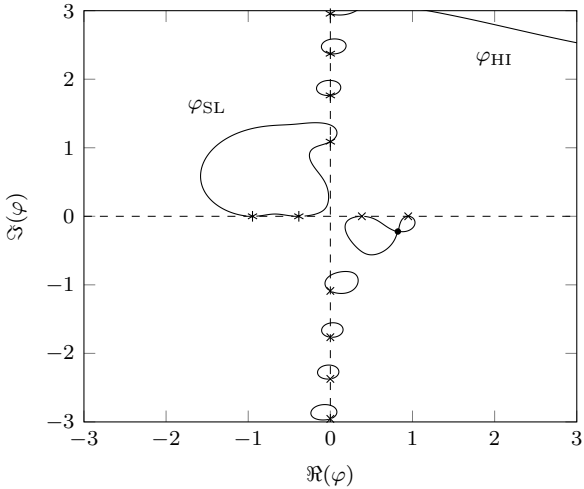

Figure 5.7 – Reduced axial wave numbers φ at $m = 1$, $\varpi = 5$, $M = 0.5$ and $\Re(Z) = 0.7380$.

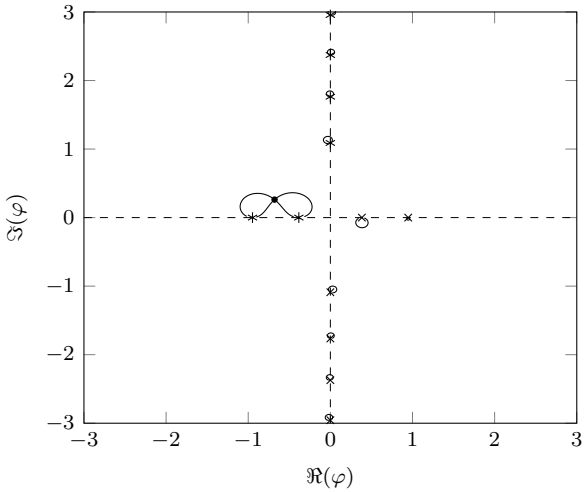

Figure 5.8 – Reduced axial wave numbers φ at $m = 1$, $\varpi = 5$, $M = 0.5$ and $\Re(Z) = 3.0737$.

Finally, this analysis considers ducts of infinite lined length, while turbofan aero-engines have a duct length/radius ratio around 1, as well a finite lined length. As a consequence, the maximum sound attenuation can be obtained by a combination of liner attenuation and reflections at the hard-soft wall transition, as well at the duct opening. In the following chapter, the sound attenuation prediction is also based on the theory of an infinite lined duct, but it provides an estimative of the attenuation of the optimal impedance.

5.3 Aero-engine applications

The examples given in the previous section are not fully representative of typical turbofan aero-engines. During approach, the engine is at a low power configuration, such that the fan blade tips are at subsonic speed. The dominant components are given by the rotor-stator interaction and predicted by Tyler and Sofrin rule [80]. However, at cut-back and sideline, which represent take-off and climb, the fan blade tips are at supersonic speed, and the dominant component is the rotor-alone tone with azimuthal order given by the number of blades.

According to McAlpine [81], a typical modern high-bypass ratio has geometry and operating conditions as listed in Table 5.2 and Table 5.3. Particular emphasis is given to cut-back and sideline conditions, when fan noise is most critical. Also, the first radial mode order is the one with highest acoustic energy content [81], so the auxiliary mode index υ is omitted since the interest lies on this particular mode.

Table 5.2 – Geometry of a typical modern turbofan engine [81].

Number of fan blades	B	24
Duct radius	b	1.0 m
Duct length	L_d	1.1 m
Liner length	L	0.8 m

Table 5.3 – Operating conditions of a typical modern turbofan engine [81].

Fan speed	M	BPF	ka
Cut-back	-0.4	1440 Hz	26.6
Sideline	-0.5	1680 Hz	31.0

According to Equation 5.23, the optimal impedance for cut-back and sideline conditions at the aero-engine inlet are

$$Z^{(24,1)}_{\text{opt,cut-back}} = 1.9664 - i1.1640 \tag{5.27}$$

and

$$Z^{(24,1)}_{\text{opt,sideline}} = 4.1562 - i1.3373. \tag{5.28}$$

Figures 5.9 and 5.10 show that these impedances are indeed the optimal values. In his paper, McAlpine [81] argues that, at cut-back condition, the mode (24,1) is near cut-off[3], and then it should be well absorbed by the liner. In fact, at the optimal impedance, $\Im(\varphi)$ is relatively high, and since $\Delta\text{SPL} \propto \Im(\varphi)$ (this relation is explored in details in the next chapter), sound attenuation is also high. In practical terms, the modal energy may be smaller than other components, so the fan noise becomes essentially broadband.

At sideline condition, mode (24,1) is well cut-on[4], and therefore should be less absorbed by the liner. At the optimal impedance, $\Im(\varphi)$ is much closer to the real axis than at cut-back condition. The outcome is a lower sound attenuation, as predicted by McAlpine [81]. It is important then to optimize the liner impedance for this condition, since any variation in the tone level is well captured by the EPNL metric.

It must be noted that the optimal impedance here derived is based on uniform flow assumption. In the case of shear flow, the axial wave numbers are affected, and it is very likely that the optimal impedance is affected as well. In the next chapter, sound attenuation prediction for shear flow shows that, indeed, the optimal impedance changes for different boundary layer thickness. The values of optimal impedance given by Equations 5.27 and 5.28 are nevertheless a first estimative in the project of acoustic liners for turbofan aero-engines.

[3]If the mode is cut-off in a rigid-walled duct, the axial wave number is purely imaginary. In the presence of a lined wall, the axial wave number is complex. So, it may have a small real part, but still a relatively high imaginary part, thus the mode is "near" cut-off.

[4]Opposite to near cut-off. The imaginary part of the axial wave number is relatively small in the presence of a lined wall.

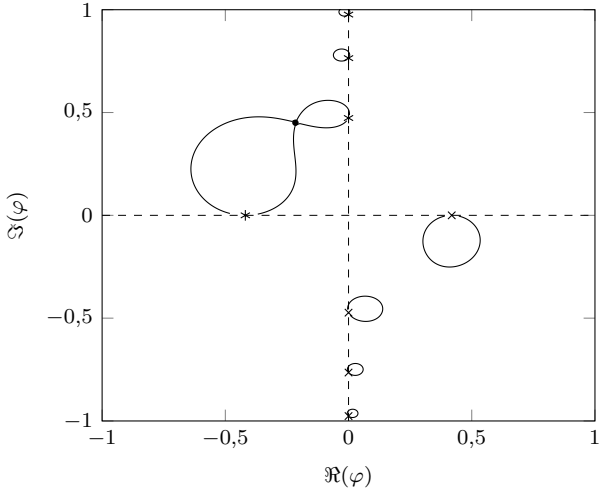

Figure 5.9 – Reduced axial wave numbers φ at $m = 24$, $\varpi = 26.6$, $M = 0.4$ (cut-back condition) and $\Re(Z) = 1.9664$.

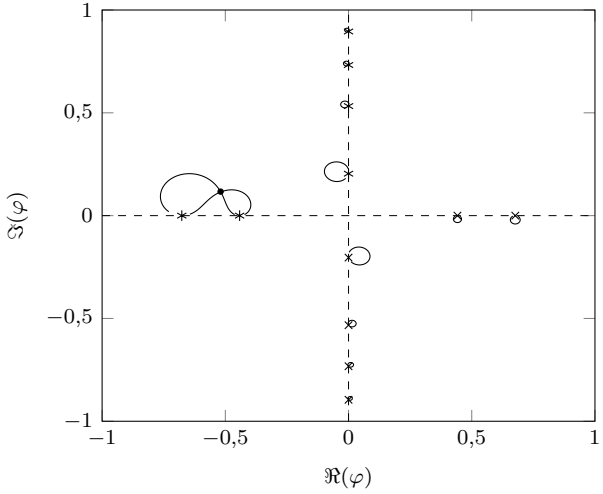

Figure 5.10 – Reduced axial wave numbers φ at $m = 24$, $\varpi = 31.0$, $M = 0.5$ (sideline condition) and $\Re(Z) = 4.1562$.

6 SOUND ATTENUATION PREDICTION

The optimal impedance from Chapter 5 can be linked to the corresponding liner by means of semi-empirical models (Chapter 3) or experimental results (Chapter 4). However, the previous chapters are of minor importance if sound attenuation in aero-engines cannot be predicted. This chapter is concerned with the effects of uniform and shear flow assumptions on the sound attenuation prediction for a given wall impedance and liner length. It is worth noting that the equations presented here are based on infinite wave guides i.e. ducts of infinite extension with neither reflections at the end nor wall impedance discontinuities.

First, the calculation of attenuation is presented. It is shown that sound attenuation is a function of liner length and axial wave number, so the procedure to calculate the eigenvalues in the presence of uniform and shear flow is described. Secondly, an impedance model is chosen. Since liner impedance is function of the Mach number, it makes sense to include a flow-sensitive model (such as Guess model), in order to evaluate the results when comparing cut-back and sideline conditions[1]. Thirdly, effects of flow velocity and boundary layer thickness are analysed for low-order modes. Finally, the investigation is extended to typical aero-engine geometry and operating conditions.

6.1 Calculation of attenuation

From here on, attenuation is defined as the reduction in SPL over a specified length of a lined duct, typically the liner length. As previously stated, under the assumption of no reflections at the end, attenuation is given effectively by the amplitude change on transmitted modes. Hence, it can be calculated for each mode individually or in terms of total attenuation. For instance, the total reduction in acoustic energy, assuming equal amplitude per mode, is given by [82]

$$\Delta L_W = 10 \log_{10} \left(\sum_{m=0}^{\infty} \sum_{n=1}^{\infty} E_{mn}(0) \Big/ \sum_{m=0}^{\infty} \sum_{n=1}^{\infty} E_{mn}(L) \right), \qquad (6.1)$$

[1] Liner geometry is the same in both cases, so the impedance has to be correctly predicted for different Mach numbers.

where $E_{mn}(0)$ and $E_{mn}(L)$ are the mean modal acoustic energy flow at inlet and outlet, respectively, and L_W is the sound power level (PWL). The derivation of these variables is rather complicated and the reading of Ko's work [82, 83] is recommended. On the other hand, a relatively simple expression may be derived for modal SPL reduction, which is defined as

$$\Delta L_p^{(mn)} = 20 \log_{10} \left(\frac{\bar{P}(x, y, L)}{\bar{P}(x, y, 0)} \right), \tag{6.2}$$

where $\bar{P}$ is the root-mean-squared acoustic pressure. It further simplifies to [84]

$$\Delta L_p^{(mn)} = 8.68 L |\Im(k_z^{(mn)})|, \tag{6.3}$$

In other words, the attenuation on z-direction is only function of the imaginary part of axial wave number and liner length. Note that $\Im(k_z)$ can assume either positive or negative values depending on the direction of propagation. As seen in Chapter 5, k_z is solution of the eigenvalue equation, and thus Equation 6.3 is valid for each mode (mn).

6.1.1 Uniform flow

The eigenvalue equation in the presence of uniform flow and a lined wall assuming Ingard-Myers boundary condition [28, 29] is given by

$$\frac{ik}{Z} \left(1 - \frac{k_z^{(mn)}}{k} M \right)^2 = k_r^{(n)} \frac{J'_m(ak_r^{(n)})}{J_m(ak_r^{(n)})}, \tag{6.4}$$

or, by using the dimensionless variables from Chapter 5,

$$\frac{i\varpi}{Z} \left(1 - \frac{\kappa}{\varpi} M \right)^2 = \alpha \frac{J'_m(\alpha)}{J_m(\alpha)}, \tag{6.5}$$

Note that Equation 6.5 is equivalent to Equation 5.18. Also, the dispersion relation is now given by

$$\kappa = \frac{-\varpi M \pm \sqrt{\varpi^2 - \beta^2 \alpha^2}}{\beta^2}. \tag{6.6}$$

If $M = 0$, Equation 5.12 is recovered. In this work, Equation 6.5 is solved with Matlab `fsolve` function. Since each mode (mn) has its solution, it is important to provide an appropriate initial guess. The idea is to start from a well-known value i.e. radial wave numbers in the

hard wall and no flow case, given by the roots of

$$J'_m(\alpha) = 0. \tag{6.7}$$

Then, Equation 6.5 is solved for a new Mach number $M = \Delta M$ by using the previous κ as initial guess. This process is repeated in steps of ΔM until the desired Mach number is achieved, and consequently, the correct value of κ is found.

6.1.2 Shear flow

In the presence of shear flow, it is not possible to obtain an explicit solution for the eigenvalue equation. Therefore, the amplitude of the pressure disturbance assuming harmonic excitation is given by the Pridmore-Brown equation [54] as,

$$\frac{d^2P}{dr^2} + \left[\frac{1}{r} + \frac{2k_z}{k - Mk_z}\frac{dM}{dr}\right]\frac{dP}{dr} + \left[(k - Mk_z)^2 - k_z^2 - \frac{m^2}{r^2}\right]P = 0, \tag{6.8}$$

or, in terms of a non-dimensional duct radius $R = r/a$,

$$\begin{aligned}\frac{d^2P}{dR^2} + &\left[\frac{1}{R} + \frac{2k_z}{k - Mk_z}\frac{dM}{dR}\right]\frac{dP}{dR} \\ &+ \left\{(ka)^2\left[\left(1 - M\frac{k_z}{k}\right)^2 - \left(\frac{k_z}{k}\right)^2\right] - \frac{m^2}{R^2}\right\}P = 0,\end{aligned} \tag{6.9}$$

Any flow profile can be chosen e.g. parabola, power law, etc. If the flow is not fully developed, the equation may be split in two parts: (i) the boundary layer region, given by Equation 6.9 and (ii) the uniform flow region, where $dM/dr = 0$, hence

$$\frac{d^2P}{dr^2} + \frac{1}{r}\frac{dP}{dr} + \left[(k - Mk_z)^2 - k_z^2 - \frac{m^2}{r^2}\right]P = 0, \tag{6.10}$$

whose eigenvalue equation was given in the previous section. At the interface, continuity of pressure and acoustic particle velocity must be ensured.

The procedure to numerically integrate this equation is described

as follows. First, Equation 6.9 is rewritten as

$$\frac{d^2P}{dR^2} + f_1(R)\frac{dP}{dR} + f_2(R)P = 0, \tag{6.11}$$

and split into a pair of first order ordinary differential equations,

$$\begin{cases} \dfrac{dP}{dR} = G, \\ \dfrac{dG}{dR} = -f_1(R)G - f_2(R)P. \end{cases} \tag{6.12}$$

The auxiliary functions $f_1(R)$ and $f_2(R)$ are given by

$$f_1(R) = \frac{1}{R} + \frac{2k_z}{k - Mk_z}\frac{dM}{dR}, \tag{6.13}$$

$$f_2(R) = (ka)^2\left[\left(1 - M\frac{k_z}{k}\right)^2 - \left(\frac{k_z}{k}\right)^2\right] - \frac{m^2}{R^2}. \tag{6.14}$$

Equation 6.12 can be numerically integrated using the fourth-order Runge-Kutta scheme [85], such as the `bvp4c` solver in Matlab. Still, it is not a straightforward task. If a hard wall boundary condition is applied, the axial wave number is purely real. However, in the case of a soft wall, the pressure profile is complex, as well the axial wave number. Thus, the pair of ordinary differential equations has to be further divided into real and imaginary parts. Following Mungur and Gladwell procedure [85], the pressure disturbance can be written as

$$P = P_1 + iP_2, \tag{6.15}$$

and

$$\frac{d^2P}{dR^2} + (g_1 + ig_2)\frac{dP}{dR} + (g_3 + ig_4)P = 0, \tag{6.16}$$

such that

$$P_1 = \Re(P), \tag{6.17}$$

$$P_2 = \Im(P), \tag{6.18}$$

$$g_1 = \Re\left(\frac{1}{R} + \frac{2k_z}{k - Mk_z}\frac{dM}{dR}\right), \tag{6.19}$$

$$g_2 = \Im\left(\frac{1}{R} + \frac{2k_z}{k - Mk_z}\frac{dM}{dR}\right), \tag{6.20}$$

$$g_3 = \Re\left((ka)^2\left[\left(1 - M\frac{k_z}{k}\right)^2 - \left(\frac{k_z}{k}\right)^2\right] - \frac{m^2}{R^2}\right), \tag{6.21}$$

$$g_4 = \Im\left((ka)^2\left[\left(1 - M\frac{k_z}{k}\right)^2 - \left(\frac{k_z}{k}\right)^2\right] - \frac{m^2}{R^2}\right). \tag{6.22}$$

Equation 6.16 can also be separated into real and imaginary parts, so that

$$\begin{cases} P_1'' + g_1 P_1' - g_2 P_2' + g_3 P_1 - g_4 P_2 = 0, \\ P_2'' + g_2 P_1' + g_1 P_2' + g_3 P_2 + g_4 P_1 = 0. \end{cases} \tag{6.23}$$

The next step is to rewrite each line as a first order ordinary differential equation. So, if the following auxiliary variables are defined,

$$\begin{cases} P_1' = P_3, \\ P_2' = P_4, \end{cases} \tag{6.24}$$

then

$$\begin{cases} P_3' = -g_3 P_1 + g_4 P_2 - g_1 P_3 + g_2 P_4 \\ P_4' = -g_4 P_1 - g_3 P_2 - g_2 P_3 - g_1 P_4 \end{cases} \tag{6.25}$$

These equations may be written in matrix form,

$$\begin{Bmatrix} P_1 \\ P_2 \\ P_3 \\ P_4 \end{Bmatrix}' = \begin{bmatrix} 0 & 0 & 1 & 0 \\ 0 & 0 & 0 & 1 \\ -g_3 & g_4 & -g_1 & g_2 \\ -g_4 & -g_3 & -g_2 & -g_1 \end{bmatrix} \begin{Bmatrix} P_1 \\ P_2 \\ P_3 \\ P_4 \end{Bmatrix}, \tag{6.26}$$

or also

$$\mathbf{Q}\mathbf{p} = \mathbf{p}'. \tag{6.27}$$

The boundary conditions still have to be applied. At a distance η of

the duct centreline[2], where $\eta \ll 1$, the acoustic pressure may be set to an arbitrary constant. If $m = 0$,

$$\begin{cases} P_1(\eta) = 1, \\ P_2(\eta) = 0, \\ P_3(\eta) = 0, \\ P_4(\eta) = 0. \end{cases} \tag{6.28}$$

If $m > 0$, then, according to Eversman [84],

$$\begin{cases} P_1(\eta) = \eta^m, \\ P_2(\eta) = 0. \\ P_3(\eta) = m\eta^{m-1}, \\ P_4(\eta) = 0. \end{cases} \tag{6.29}$$

At the lined wall, the flow has zero velocity, such that the impedance boundary condition is given simply by

$$\begin{cases} P_3(1) = -\Re\left(\dfrac{ika}{Z}P(1)\right) \\ P_4(1) = -\Im\left(\dfrac{ika}{Z}P(1)\right) \end{cases} \tag{6.30}$$

6.2 Impedance model

As seen in the previous section, the Pridmore-Brown equation is solved for a given impedance Z and wave frequency ω. It makes sense to use an impedance model, as discussed in Chapter 3, since it relates liner geometry and operating condition to its impedance. Experimental results are limited to the measured velocities i.e. $M \approx 0.3$ in this work, and usually the curves are non-smooth, which is not a liner physical behaviour. The impedance models from Chapter 4 are applied to eduction techniques, so no explicit relation is given between liner geometry/operating conditions and impedance models. From here on, only predictive semi-empirical models are considered, more specifically

[2]Due to the singular nature of the differential equation at $r = 0$, the equation must be evaluated at a value close do the duct centreline.

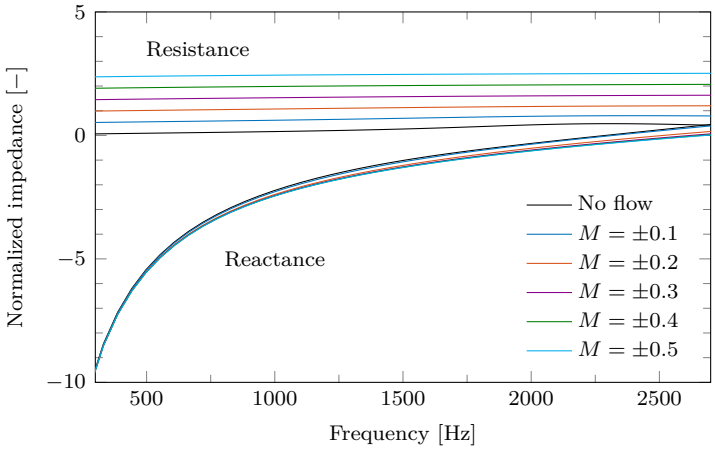

Figure 6.1 – Impedance prediction for liner A based on a modified Guess model. The impedance is independent of flow direction.

a slightly modified Guess model, given by

$$\theta = \frac{\sqrt{8\nu\omega}}{\sigma c}\left(1+\frac{\tau}{d}\right) + \frac{\pi^2}{2\sigma}\left(\frac{fd}{c}\right)^2 + \frac{(1-\sigma^2)}{\sigma}0.24M + \frac{(1-\sigma^2)}{\sigma}\frac{|u|}{c}, \tag{6.31}$$

$$\chi = \frac{\sqrt{8\nu\omega}}{\sigma c}\left(1+\frac{\tau}{d}\right) + \frac{\omega(\tau+\delta)}{\sigma c} - \cot\left(\frac{\omega l}{c}\right). \tag{6.32}$$

It can be noticed that the grazing flow term had the constant modified from 0.3 to 0.24 as an attempt to better predict the resistance from low-POA liners. The geometry from liner A is here considered, as given in Table 2.1. The impedance prediction is shown in Figure 6.1 for different flow velocities. No distinction is made between upstream and downstream results, so the impedance is independent of flow direction.

On the following, the effect of different flow velocities and boundary layer thickness are analysed. In this work, the impedance is function of the Mach number, mainly the resistive part, while in other works [82–84], the resistance is held constant, independent of flow velocity. This is a valid assumption for SDOF liners covered with wire mesh, which is not the case for liner A. Therefore, the trends observed in previous works [82–84] are to some extent different from the following figures.

6.3 On the effect of flow velocity

As a first approach, an almost uniform flow is assumed, and the effect of flow velocity for both upstream and downstream propagating waves is considered. The boundary layer thickness is arbitrarily chosen as 0.1 % of the duct radius and the boundary layer profile is assumed linear. Although it is not an actual representation of the boundary layer, it has been observed that the impact of the boundary layer profile is limited provided the displacement thickness remains constant [30, 74, 86]. Other parameters necessary to the solution of the Pridmore-Brown equation are defined as follows: duct radius $a = 0.1\,\mathrm{m}$, liner length $L = 0.1\,\mathrm{m}$ and azimuthal order $m = 0$. As can be seen, it is not representative of typical aero-engines, nevertheless useful for understanding different behaviours in attenuation results.

The results from Figure 6.2a represent the inlet of an aero-engine i.e. upstream propagating waves. Up to $M = -0.2$, the fundamental mode (01) is not always the least attenuated mode in the frequency range here considered. At frequencies between 1.5 kHz and 1.75 kHz, the first higher-order mode (02) becomes the least attenuated mode. As seen in Chapter 5, the appearance of surface waves becomes critical at low resistances, which is the case at low Mach numbers and explains the high attenuation of the first mode after 1.5 kHz. So, one must consider that, if the modal energy is similar for each mode, the total attenuation is dominated by the least attenuated mode. As flow velocity increases from $M = -0.3$ up to $M = -0.5$, the frequency of maximum attenuation is shifted to lower frequencies. It must be noted, differently from Ko [82, 83] and Eversman [84], the maximum attenuation is approximately constant due to the fact that here the resistance increases with Mach number.

The case considered in Figure 6.2b is equivalent to exhaust flow. Although it is not in the scope of this work, fan noise is also present at exhaust (see Figure 1.2 for instance) and is an important noise source. Thus, it is interesting to investigate the effect of flow velocity on downstream propagating waves, despite a hollow duct is here considered, and not an annular section as in the bypass region. Only at no flow and $M = +0.1$ conditions the least attenuated mode changes from first mode to second mode. As flow velocity increases, liner attenuation is reduced and the frequency of maximum attenuation shifts to higher frequencies. At $M = +0.4$ and $M = +0.5$, the attenuation curve is almost flat and no peak is observed.

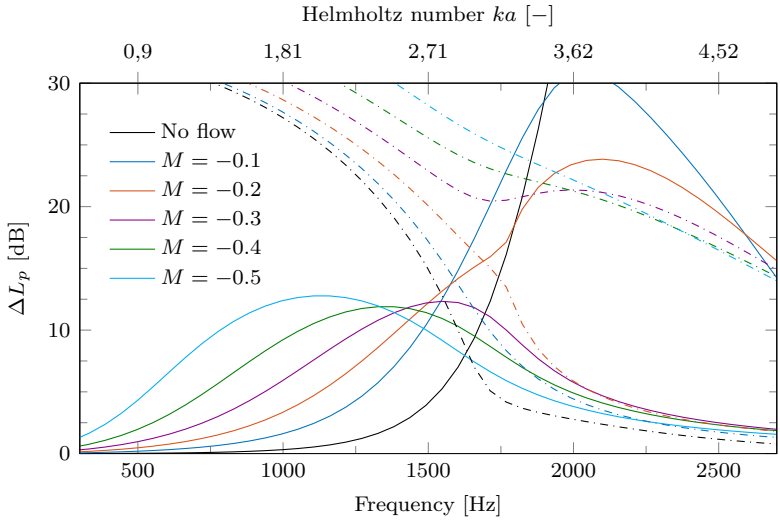

(a) Inlet flow

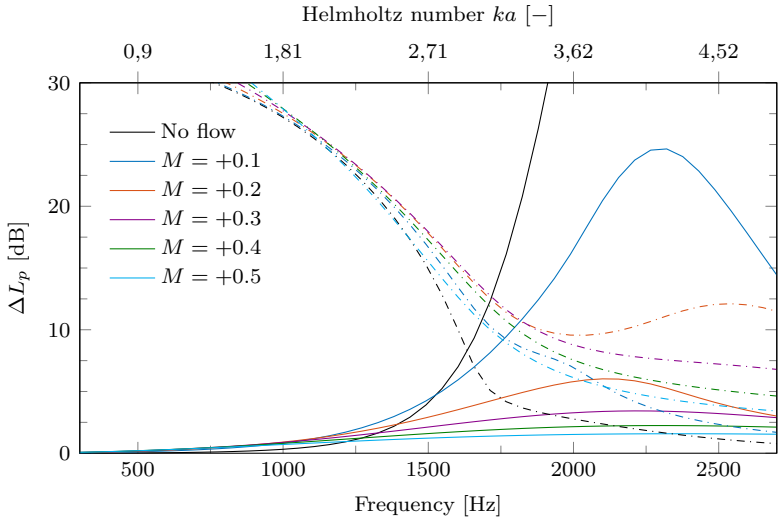

(b) Exhaust flow

Figure 6.2 – Sound attenuation prediction for different flow velocities, $\delta = 0.1\,\%$, $a = 0.1\,\mathrm{m}$, $L = 0.1\,\mathrm{m}$ and $m = 0$. The impedance is given by a modified Guess model for liner A. Solid lines (——) represent the first mode attenuation, whereas dash dotted lines (-·-·-) represent the second mode attenuation.

6.4 On the effect of boundary layer thickness

Boundary layer thickness plays a major role not only in impedance eduction techniques, but also in sound attenuation prediction. The flow velocity gradient refracts acoustic energy closer to the walls (downstream propagation) and duct centreline (upstream propagation) [54]. Thus, the overall trend is to over- and under-predict liner attenuation at inlet and exhaust flows, respectively. In order to quantify this difference, the effect of boundary layer thickness is here investigated at high flow velocities, namely $M = 0.5$ (which is similar to cut-back and sideline conditions).

As can be seen in Figure 6.3a, at the inlet, liner attenuation is very sensitive to boundary layer thickness. In the presence of a very thin boundary layer, sound attenuation reaches a peak of 13 dB around 1.1 kHz. As boundary layer thickness increases up to 10 %, maximum attenuation is reduced to 6 dB at 1.25 kHz. As expected, the acoustic wave is refracted away from the wall, reducing liner efficacy. The second radial mode is also sensitive to boundary layer thickness, however the least attenuated mode is the first radial mode in all the frequency range under analysis.

For exhaust flows, Figure 6.3b shows that liner attenuation is almost insensitive to boundary layer thickness. Only at $\delta = 10\,\%$ a noticeable change in seen, although attenuation increases less than 1 dB in the high frequency range. It must be noted that, in the bypass duct, the duct radius is considerably smaller, and the boundary layer is thicker than the intake flow. Therefore, care must be taken when concluding exhaust attenuation is not affected by shear flow.

6.5 Aero-engine applications

The previous section gave some insight on several effects i.e. flow velocity and boundary layer thickness, that can affect liner attenuation. However, it was limited to azimuthal order $m = 0$ and small duct radius. Unfortunately, this is not representative of an aero-engine. The purpose of this section is to investigate the effects of boundary layer thickness and impedance on (i) sideline and (ii) cutback conditions. The aero-engine geometry is the same from Chapter 5 i.e. it follows the values from Table 5.2. From here on, the azimuthal order of interest is $m = 24$ and flow velocity is fixed at $M = -0.4$ and -0.5 for cutback and sideline conditions, respectively. The impedance model

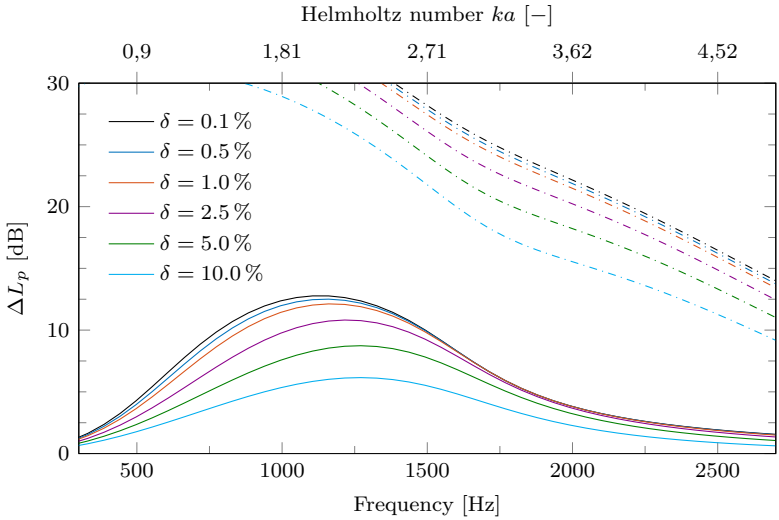

(a) Inlet flow

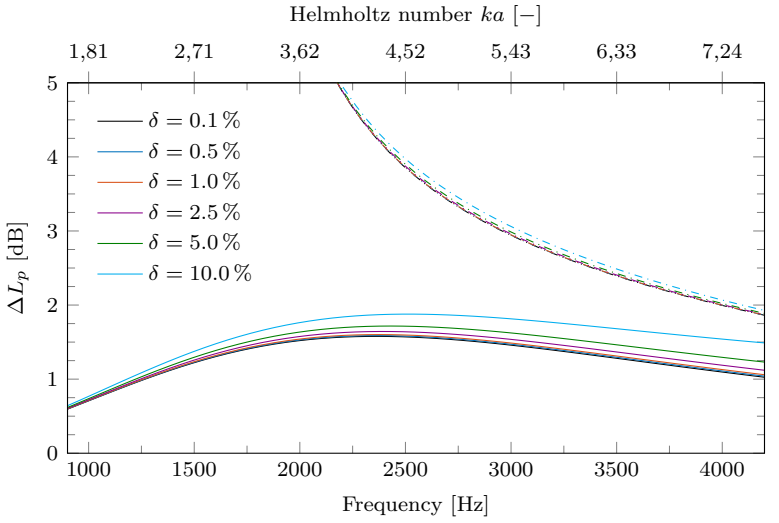

(b) Exhaust flow

Figure 6.3 – Sound attenuation prediction at $M = \pm 0.5$ and different boundary layer thickness, $a = 0.1\,\mathrm{m}$, $L = 0.1\,\mathrm{m}$ and $m = 0$. The impedance is given by a modified Guess model for liner A. Solid lines (——) represent the first mode attenuation, whereas dash dotted lines (- · - · -) represent the second mode attenuation.

also follows Figure 6.1 as a reference impedance. On the following, boundary layer thickness is first investigated. Then, the effect of liner impedance on sound attenuation is also analysed for different boundary layer thickness.

Figure 6.4a shows the results for sideline condition. At low frequencies, all radial modes are cut-off for $m = 24$, which explains the high attenuation. As frequencies increases, the first radial mode becomes cut-on[3] and the liner is responsible for sound attenuation. Effectively, the interest lies on the BPF, which corresponds to 1680 Hz. In this case, the first radial mode is the least attenuated mode for any boundary layer thickness and less than 15 dB. However, differently from the previous analysis, as boundary layer increases, sound attenuation is not necessarily reduced.

Even though cutback condition is similar to sideline condition, the conclusions are not the same. In fact, different trends can be seen in Figure 6.4b. First, at frequencies close to 1500 Hz, the second radial mode becomes the least attenuated mode up to a boundary layer thickness of 1 %. However, as boundary layer thickness increases, the first radial mode is the least attenuated mode for all the frequency range under analysis. Secondly, at this condition, the BPF corresponds to 1440 Hz. It can be seen that sound attenuation is greatly affected by boundary layer thickness, starting at 100 dB for a very thin boundary layer, and ending at 40 dB for a thickness of $\delta = 10\,\%$. Thirdly, liner impedance is $Z \simeq 2 - i1.4$, close to optimum impedance, as seen in Chapter 5, which also explains liner efficacy at this condition.

Although these figures give an overview of the liner attenuation on the frequency domain, the interest lies on the BPFs. Therefore, the frequency is held constant at 1440 Hz and 1680 Hz on the following analysis. In order to better understand the effects of boundary layer thickness on sound attenuation of the first radial mode, Figures 6.5a and 6.5b are presented. Notice that a parametric study regarding liner impedance was also performed by considering different values of the resistance θ, however focus is given to results with liner A.

For the sideline condition, maximum attenuation occurs around $\delta = 0.5\,\%$. This behaviour cannot be fully explained by refraction effects. Similar results were found by Gabard [30], who concluded that boundary layer effects are more complex than changing the propagation of sound before it interacts with the liner. For cutback condition, there is a reduction of liner attenuation as boundary layer thickness

[3]In presence of a rigid wall, the cut-on frequencies are well-known. However, in the presence of a soft wall, it is difficult to define the cut-on frequency.

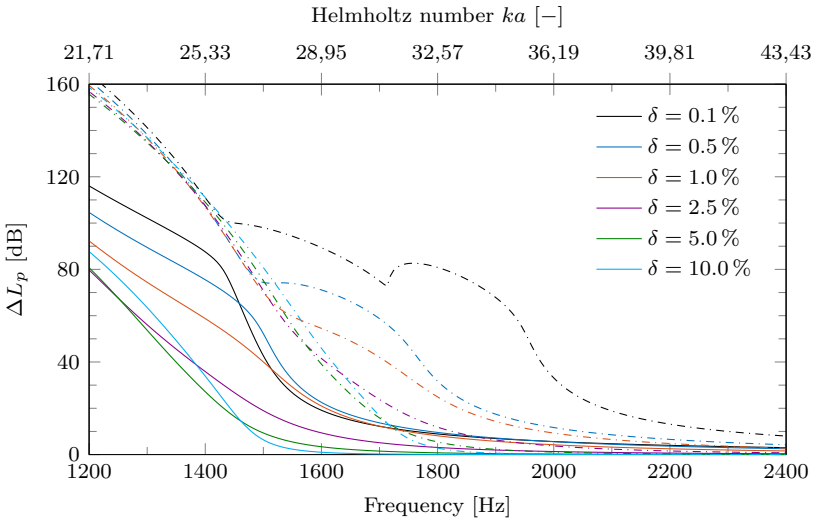

(a) Sideline condition

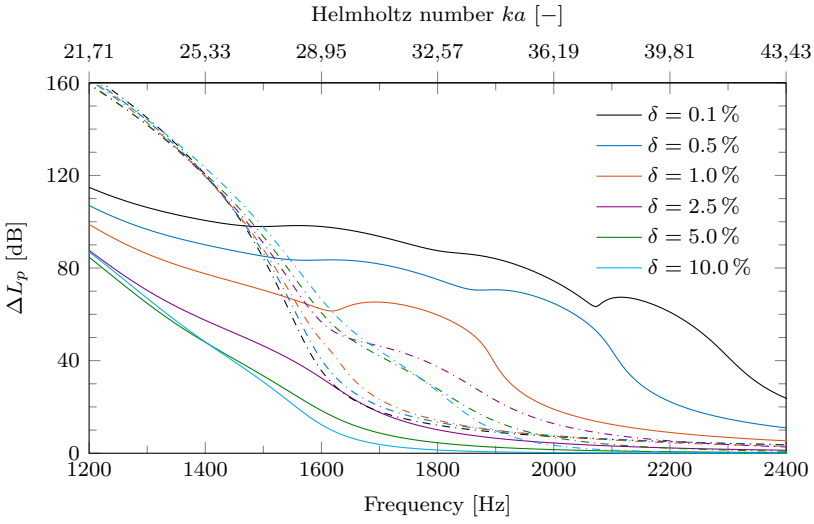

(b) Cutback condition

Figure 6.4 – Sound attenuation prediction for sideline (a) and cutback (b) conditions at $M = -0.5$ and -0.4, respectively. The impedance is given by a modified Guess model for liner A. Solid lines (——) represent first radial mode attenuation, whereas dash dotted lines (- · - · -) represent second radial mode attenuation.

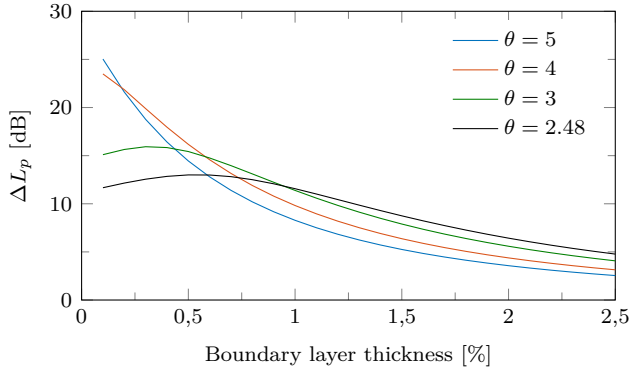

(a) Sideline condition, $ka = 31.0$, $M = -0.5$

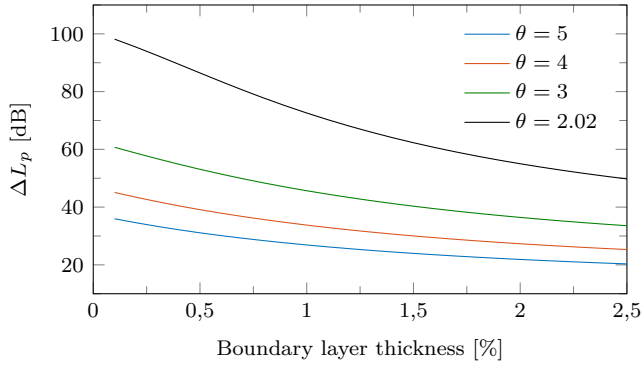

(b) Cutback condition, $ka = 26.6$, $M = -0.4$

Figure 6.5 – Sound attenuation prediction for sideline (a) and cutback (b) conditions as function of boundary layer thickness. Aero-engine geometry is given by $a = 1.0\,\text{m}$, $L = 0.8\,\text{m}$ and $m = 24$. The impedance is given by a modified Guess model for liner A.

increases. When compared to sideline condition, attenuation is high for two reasons: (i) the liner impedance is close to optimum impedance and (ii) mode $(24, 1)$ is nearly cut-off at this condition. Even in the presence of a very thick boundary layer (e.g. $\delta = 10\,\%$) modal attenuation remains around 40 dB. One must keep in mind that it does not mean a reduction of 40 dB in fan noise. Energy content from other modes must be taken into account, which may result into a more broadband noise spectrum.

Finally, the effect of liner impedance on sound attenuation is investigated. Also plotted in Figures 6.5a and 6.5b are liner attenuation prediction for several resistances, namely different perforated plate geometries. The reactance prediction for liner A is given by $\chi = -1.34$ and $\chi = -0.98$ for cutback and sideline conditions, respectively. These values are close to the optimal reactance from Chapter 5, as seen in Table 6.1.

Figure 6.5a shows that, for very thin boundary layers, attenuation is high for resistances close to 4 and 5, as expected. However, as boundary layer thickness increases, the resistance that gives the maximum attenuation decreases. In fact, from $\delta = 1\%$, liner A provides more attenuation than the optimal liner assuming uniform flow. However, this is not a straightforward analysis. For lower resistances, this trend is also valid, but the first radial mode might not be the least attenuated mode, and the overall sound attenuation is not improved. For cutback condition, the trend is very clear. As resistance increases (moving away from the optimal resistance), sound attenuation decreases.

In overall terms, a correct prediction of sound attenuation depends on the boundary layer thickness. According to Gabard [30], a good estimation of the boundary layer thickness is 2 % in the engine intake. In this case, results have shown that the optimal impedance for uniform flows no longer provides the greatest sound reduction in the presence of boundary layer. In fact, sound reduction is closer to realistic values, for instance 40 dB at cutback and 10 dB at sideline,

Table 6.1 – Comparison between optimal impedance values and impedance from liner A at cutback and sideline conditions.

	Optimal impedance	Liner A
Cutback	$1.97 - i1.16$	$2.02 - i1.34$
Sideline	$4.16 - i1.34$	$2.48 - i0.98$

according to McAlpine and Wright [81].

Finally, a new question arises: how much is sound attenuated at the optimal impedance for sheared flows? In order to answer it, the sideline condition is considered, and the resistance and the reactance are varied, resulting in the contour plots from Figure 6.6 (considering only the least attenuated mode). As can be seen, the optimal impedance for uniform flow is correctly located at the point of maximum attenuation. However, in the presence of shear flow with a boundary layer thickness of 1 %, the optimal impedance is completely different. Also affected is the maximum attenuation, which is reduced to a value around 28 dB. This analysis can be extended to different boundary layer thickness, which would lead to different values of maximum attenuation and optimal impedance.

Alternatively, the optimal impedance in uniform flows from Chapter 5 could be extended to include Brambley boundary condition. It has been shown that this boundary condition is able to follow the trends found when solving the Pridmore-Brown equation [30, 74]. Therefore, in order to provide a better first guess, boundary layer thickness is included in the optimal impedance analysis. From that, further refinements are made using the Pridmore-Brown equation.

It must be noted that previous section is based on an infinitely long lined duct with a constant boundary layer thickness. The overall picture changes for aero-engines. First, noise reduction in the far-field could benefit from reflections at the end of the duct and hard/soft wall transition. Secondly, duct radius is not constant, and neither Mach number inside the duct nor boundary layer thickness. Thirdly, besides Mach number, SPL also varies along the lined wall, and so does liner impedance. Thus, the previous analysis provides a meaningful insight into liner performance at different conditions, but the optimal liner may be only achieved by means of numerical simulations and experimental validation.

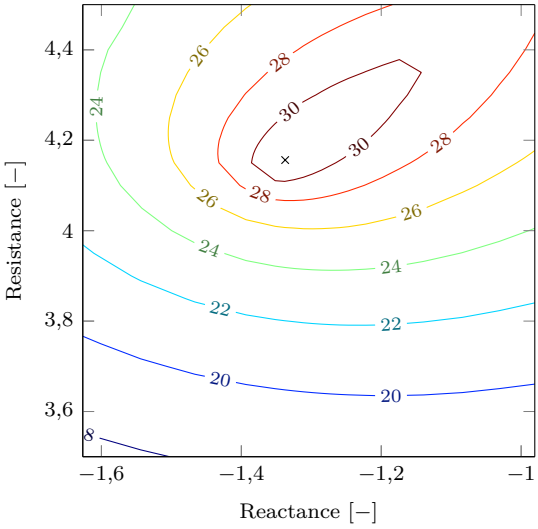

(a) Uniform flow

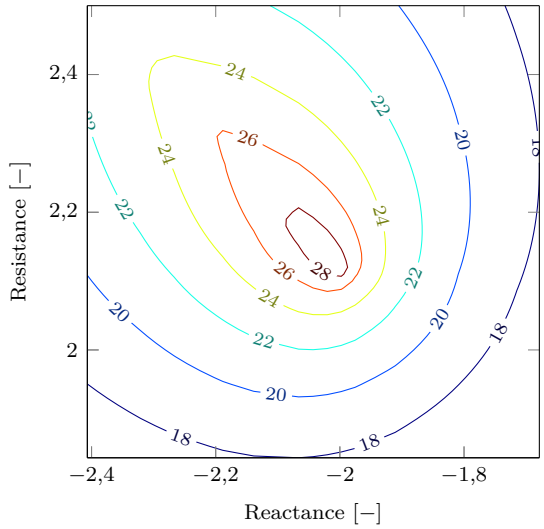

(b) Shear flow, $\delta = 1\,\%$

Figure 6.6 – Sound attenuation prediction for sideline condition regarding different impedances considering uniform flow and shear flow with $\delta = 1\,\%$. The cross (×) represents the optimal impedance for uniform flow.

7 CONCLUSIONS AND FUTURE WORK

Acoustic liners remain a key technology in noise reduction of turbofan aero-engines. However, due to the complex environment to which they are exposed, it remains a challenge to correctly predict sound attenuation in different conditions. In this work, predictive models and experimental techniques were investigated. Both approaches are an attempt to translate liner geometry into acoustic impedance. Then, the concept of optimal impedance was further developed and, and examples were given for a typical aero-engine. Finally, a parametric study of sound attenuation prediction was performed. Special care was given for boundary layer thickness effects. On the following, the main conclusions from each chapter are summarized.

Chapter 3 reviews some of the predictive models available in the literature. The comparison with experimental results show that most of the models fail to accurately predict liner impedance, specially the resistance. Kooi and Sarin model closely follows most of the experimental results. Guess and Elnady and Bodén models over-predicted the resistance, whereas Motsinger and Kraft model under-predicted the resistance for most of the frequency range under analysis. In general, the reactance is well predicted by the models. The major sources of error are the non-linear effects i.e. grazing flow and high SPL, which constantly under- or over-predict liner impedance, mainly the resistive part. Other effects, such as viscous and radiation effects, are almost negligible at typical operating conditions of turbofan aero-engines.

Chapter 4 presents typical results from the impedance eduction techniques available at LVA/UFSC, more specifically the mode matching and straightforward methods. At certain frequencies, liner attenuation is too high, and effectively flow-noise is being measured. Since mode matching method is performed at each frequency individually, liner impedance at these frequencies remains unknown. Therefore, impedance models which obey reality, passivity and causality conditions are included in the mode matching method, leading to a multiple-frequency optimization routine. Results have shown that most of the experimental curves are improved. However, at certain conditions, the impedance model is not able to follow the trend from experimental results.

Another discussion arises from differences between upstream and downstream results for the educed impedances. In order to investigate whether theses differences are inherent to liner physics or flaws in educ-

tion techniques, alternative approaches regarding boundary conditions are analysed. In the mode matching technique, results using Brambley boundary condition are compared to Ingard-Myers boundary condition, whereas in the straightforward technique an exact solution based on the Pridmore-Brown equation is compared to uniform flow assumption with Ingard-Myers boundary condition. In general, when boundary layer thickness is considered, impedance results from upstream and downstream measurements are closer, but not in full agreement. Further investigations are necessary to explain these differences.

Chapter 5 builds up the theory of optimal impedance in lined ducts. It is shown that the optimal impedance prediction for rectangular ducts in the presence of flow is not valid for circular ducts, and an appropriate equation is derived. The effect of optimal impedance on axial wave numbers is graphically explained. Finally, examples of optimal values are given for different conditions in a typical aero-engine geometry. Special care is given to sideline and cutback conditions, where rotor-alone tones are the dominating modes. The optimal impedance and liner impedance curve have opposite trends i.e. it is not possible to satisfy both optimal impedances with a single liner geometry. For instance, the optimal reactance decreases from sideline to cutback condition, whereas liner reactance increases.

Chapter 6 focus on prediction of sound attenuation in the presence of shear flow. Effects of flow velocity and boundary layer thickness are first investigated. Inlet flows are more sensitive to boundary layer thickness than exhaust flows, and the frequency and level of maximum attenuation depend on both flow velocity and boundary layer thickness. As liner impedance is also function of Mach number, the trend is not the same as usually presented in previous works. Finally, liner attenuation is analysed for a typical aero-engine geometry and operating conditions. It is shown that the optimal impedance in uniform flows is not valid in shared flows. Also, liner attenuation does not always follow the expected trend regarding refraction effects. The analysis is limited to straight ducts with constant boundary layer thickness, which is not the case in aero-engines, but should provide a first estimative of liner attenuation.

Overall, all chapters encompass the main tools for the project of acoustic liners. The optimal impedance in lined ducts can be rapidly estimated with equations from Chapter 5. Predictive models from Chapter 3 provide liner geometry, and experimental techniques from Chapter 4 assess liner impedance. Attenuation prediction from Chapter 6 gives the final result. Finally, it would be expected that such a

process would be iterative, with experimental data corroborating analytical models or being used to improve the next iteration.

7.1 Suggestions for future work

None of the semi-empirical models here presented have satisfactorily predicted the experimental results. Possible causes are (i) small number of test samples when the models were developed and adjusted, (ii) oversimplification of the non-linear terms, (iii) small valid range of the models and (iv) possible flow direction effects on liner impedance. Further research should better understand how grazing flow and high SPL affect the impedance at the hole, such that liner impedance can be correctly predicted for a given geometry and operating conditions. Some physical dissipation mechanisms may include acoustic-flow coupling at the holes and viscothermal effects the at the walls.

The impedance models from Chapter 4 seem to better follow experimental results than predictive models from Chapter 3. Thus, if the model parameters can be associated with liner geometry and operating conditions, a better semi-empirical model may be obtained.

The multiple-frequency mode matching could be extended to include shear flow effects by means of Brambley boundary condition. Therefore, a better agreement between the models and experimental results can be expected.

Differences between upstream and downstream results in the impedance eduction techniques must be further investigated. A numerical analysis of an array of Helmholtz resonators could explain if the incoming wave in sensitive to the direction of vortex shedding in the case of grazing incidence.

The eigenvalue equation for optimal impedance here presented was based on uniform flow assumption with Ingard-Myers boundary condition. A similar approach is to include boundary layer effects by means of the Brambley boundary condition, which has shown to provide better results when compared to solution of the Pridmore-Brown equation. Thus, a better estimate of the optimal impedance might be achieved, mainly for inlet flows.

Sound attenuation prediction is highly affected by the presence of boundary layer, specially at engine intake. Different reference geometries can be studied to check whether trends found in this work are still valid. Ultimately, numerical simulations and experimental data can further validate this analysis.

Most of the mathematical formulation in this work is valid for infinitely long straight ducts. In order to better represent typical turbofan aero-engines, effects of slowly varying duct radius and impedance transition should be investigated. Also, viscous effects and turbulent mixing have been neglected in this work, but they can also play a role in sound attenuation, and consequently in liner optimization.

REFERENCES

[1] SMITH, M. J. **Aircraft Noise**. [S.l.]: Cambridge University Press, 2004.

[2] ICAO. **International Civil Aviation Organisation, Volume 1: Aircraft noise, em Annex 16 to the Convention on International Civil Aviation: Environmental Protection, Procedures for the Noise Certification of Aircraft. 5th ed., July 2008.** [S.l.].

[3] KAPLAN, B.; NICKE, E.; VOSS, C. Design of a highly efficient low-noise fan for ultra-high bypass engines. In: AMERICAN SOCIETY OF MECHANICAL ENGINEERS. **ASME Turbo Expo 2006: Power for Land, Sea, and Air**. [S.l.], 2006. p. 185–194.

[4] BATARD, H. Development of the quiet aircraft - industrial needs in terms of aircraft noise and main achievements in europe. **Forum Acusticum**, Budapest, 2005.

[5] MOTSINGER, R.; KRAFT, R. Design and performance of duct acoustic treatment. In: **Aeroacoustics of Flight Vehicles: Theory and Practice. Volume 2: Noise Control**. [S.l.: s.n.], 1991.

[6] BIELAK, G.; PREMO, J.; HERSH, A. **Advanced turbofan duct liner concepts**. [S.l.]: National Aeronautics and Space Administration, Langley Research Center, 1999.

[7] JONES, M. G. et al. Effects of liner geometry on acoustic impedance. In: **8th AIAA/CEAS Aeroacoustics Conference and Exhibit**. Breckejridge, Colorado: No. AIAA 2002-2446, June 17–19 2002.

[8] KABRAL, R.; BODéN, H.; ELNADY, T. Determination of liner impedance under high temperature and grazing flow conditions. In: **20th AIAA/CEAS Aeroacoustics Conference**. Atlanta, GA: No. AIAA 2014-2956, 16–20 June 2014.

[9] AURéGAN, Y.; STARBINSKI, R.; PAGNEAUX, V. Influence of grazing flow and dissipation on the acoustic boundary condition

at a lined wall. **Journal of the Acoustic Society of America**, v. 109, n. 1, p. 59–64, 2001.

[10] MURRAY, P. B.; FERRANTE, P.; SCOFANO, A. Manufacturing process and boundary layer influences on perforate liner impedance. In: **11th AIAA/CEAS Aeroacoustics Conference (26th AIAA Aeroacoustics Conference)**. Monterey, California: No. AIAA 2005-2849, May 23–25 2005.

[11] JONES, M. G.; WATSON, W. R.; NARK, D. M. Effects of flow profile on educed acoustic liner impedance. In: **16th AIAA/CEAS Aeroacoustics Conference**. Stockholm, Sweden: No. AIAA 2010-3763, June 7–9 2010.

[12] SPILLERE, A. M. N. et al. Cross-validation of a new grazing flow liner test rig using multiple impedance eduction techniques. In: **The 22nd International Congress on Sound and Vibration**. Florence, Italy: [s.n.], 12–16 July 2015.

[13] BODéN, H. et al. On the effect of flow direction on impedance eduction results. In: **22nd AIAA/CEAS Aeroacoustics Conference**. Lyon, France: No. AIAA 2016-2727, May 30 – June 1 2016.

[14] KOOI, J. W.; SARIN, S. L. An experimental study of the acoustic impedance of Helmholtz resonator arrays under a turbulent boundary layer. In: **7th Aeroacoustics Conference**. Palo Alto, CA: [s.n.], October 5–7 1981.

[15] GOLDMAN, A.; PANTON, R. Measurement of the acoustic impedance of an orifice under a turbulent boundary layer. **Journal of the Acoustical Society of America**, v. 60, n. 6, p. 1397–1404, 1976.

[16] MURRAY, P.; ASTLEY, R. J. Development of a single degree of freedom perforate impedance model under grazing flow and high spl. In: **18th AIAA/CEAS Aeroacoustics Conference (33rd AIAA Aeroacoustics Conference)**. Colorado Springs, CO: No. AIAA 2012-2294, 04–06 June 2012.

[17] ZHANG, Q.; BODONY, D. J. Numerical investigation of a honeycomb liner grazed by laminar and turbulent boundary layers. **Journal of Fluid Mechanics**, v. 792, p. 936–980, 2016.

[18] ZHAO, H.; SUR, X. Active control of wall acoustic impedance. **AIAA Journal**, v. 37, n. 7, p. 825–831, 1999.

[19] LIU, F. et al. A multiple degree of freedom electromechanical helmholtz resonator. **The Journal of the Acoustical Society of America**, v. 122, n. 1, p. 291–301, 2007.

[20] GUESS, A. W. Calculation of perforated plate liner parameters from specified acoustic resistance and reactance. **Journal of Sound and Vibration**, v. 40, n. 1, p. 119–137, 1975.

[21] ELNADY, T.; BODéN, H. On semi-empirical liner impedance modeling with grazing flow. In: **9th AIAA/CEAS Aeroacoustics Conference and Exhibit**. Hilton Head, South California: No. AIAA 2003-3304, 12–14 May 2003.

[22] DREVON, E. Measurement methods and devices applied to A380 nacelle double degree-of-freedom acoustic liner development. In: **10th AIAA/CEAS Aeroacoustics Conference**. Manchester, Great Britain: No. AIAA 2004-2907, 2004.

[23] EATON, J. A. The influence of drainage slots on locally reacting acoustic panels. In: **5th AIAA/CEAS Aeroacoustics Conference and Exhibit**. Bellevue, WA: No. AIAA 99-1949, May 10 – May 12 1999.

[24] MURRAY, P. B.; FERRANTE, P.; SCOFANO, A. The influence of aircraft nacelle acoustic panel drainage slots on duct attenuation. In: **13th AIAA/CEAS Aeroacoustics Conference (28th AIAA Aeroacoustics Conference)**. Rome, Italy: No. AIAA 2007-3548, May 21 – May 23 2007.

[25] SUN, X. et al. A new model for the prediction of turbofan noise with the effect of locally and non-locally reacting liners. **Journal of Sound and Vibration**, v. 316, n. 1–5, p. 50 – 68, 2008.

[26] BUSSE-GERSTENGARBE, S. et al. Acoustic investigation of a specially manufactured non-locally reacting liner for aircraft application. In: **16th AIAA/CEAS Aeroacoustics Conference**. Stockholm, Sweden: No. AIAA 2010-3830, June 7–9 2010.

[27] BATTLES, Z.; TREFETHEN, L. N. An extension of matlab to continuous functions and operators. **SIAM J. Sci. Comput.**, v. 25, n. 5, p. 1743–1770, 2004.

[28] INGARD, U. Influence of fluid motion past a plane boundary on sound reflection, absorption, and transmission. **Journal of the Acoustical Society of America**, v. 31, p. 1035–1036, 1959.

[29] MYERS, M. K. On the acoustic boundary condition in the presence of flow. **Journal of Sound and Vibration**, v. 71, n. 3, p. 429–434, 1980.

[30] GABARD, G. Boundary layer effects on liners for aircraft engines. **Journal of Sound and Vibration**, v. 381, p. 30 – 47, 2016.

[31] BRAMBLEY, E. Well-posed boundary condition for acoustic liners in straight ducts with flow. **AIAA Journal**, v. 49, n. 6, p. 1272–1282, 2011.

[32] RIENSTRA, S. W.; DARAU, M. Boundary-layer thickness effects of the hydrodynamic instability along an impedance wall. **Journal of Fluid Mechanics**, v. 671, p. 559–573, 2011.

[33] DEAN, P. D. An in situ method of wall acoustic impedance measurement in flow ducts. **Journal of Sound and Vibration**, v. 34, n. 1, p. 97 – IN6, 1974.

[34] JONES, M. G.; PARROTT, T. L.; WATSON, W. R. Comparison of acoustic impedance eduction techniques for locally-reacting liners. In: **9th AIAA/CEAS Aeroacoustics Conference and Exhibit**. Hilton Head, South Carolina: No. AIAA 2003-3306, May 12–14 2003. p. 1837–1847.

[35] JONES, M. G.; WATSON, W. R.; PARROTT, T. L. Benchmark data for evaluation of aeroacoustic propagation codes with grazing flow. In: **11th AIAA/CEAS Aeroacoustics Conference (26th AIAA Aeroacoustics Conference)**. Monterey, California: No. AIAA 2005-2853, May 23–25 2005.

[36] WATSON, W. R.; JONES, M. G. Validation of a new procedure for impedance eduction in flow. In: **16th AIAA/CEAS Aeroacoustics Conference**. Stockholm, Sweden: No. AIAA 2010-3764, June 7–9 2010.

[37] PRIMUS, J.; PIOT, E.; SIMON, F. An adjoint-based method for liner impedance eduction: Validation and numerical investigation. **Journal of Sound and Vibration**, v. 332, n. 1, p. 58 – 75, 2013.

[38] ROECK, W. D.; DESMET, W. Indirect acoustic impedance determination in flow ducts using a two-port formulation. In: **15th AIAA/CEAS Aeroacoustics Conference (30th AIAA Aeroacoustics Conference)**. Miami, Florida: No. AIAA 2009-3302, 11–13 May 2009.

[39] SANTANA, L. D. et al. Two-port indirect acoustic impedance eduction in presence of grazing flows. In: **17th AIAA/CEAS Aeroacoustics Conference (32nd AIAA Aeroacoustics Conference)**. Portland, Oregon: No. AIAA 2011-2868, 05–08 June 2011.

[40] AURéGAN, Y.; LEROUX, M.; PAGNEAUX, V. Measurement of liner impedance with flow by an inverse method. In: **10th AIAA/CEAS Aeroacoustics Conference**. [S.l.]: No. AIAA 2004-2838, 10–12 May 2004.

[41] ELNADY, T. et al. Validation of an inverse analytical technique to educe liner impedance with grazing flow. In: **12th AIAA/CEAS Aeroacoustics Conference and Exhibit**. Cambridge, Massachusetts: No. AIAA 2006-2643, May 8–10 2006.

[42] ELNADY, T.; BODéN, H.; ELHADIDI, B. Validation of an inverse semi-analytical technique to educe liner impedance. **AIAA Journal**, v. 47, n. 2, p. 2836–2844, 2009.

[43] JING, X.; PENG, S.; SUN, X. A straightforward method for wall impedance eduction in a flow duct. **The Journal of the Acoustical Society of America**, v. 124, n. 1, p. 227–234, 2008.

[44] JING, X. et al. Investigation of straightforward impedance eduction in the presence of shear flow. **Journal of Sound and Vibration**, v. 335, p. 89 – 104, 2015.

[45] RENOU, Y.; AURéGAN, Y. Failure of the ingard–myers boundary condition for a lined duct: An experimental investigation. **The Journal of the Acoustical Society of America**, v. 130, n. 1, p. 52–60, 2011.

[46] ALOMAR, A.; AURéGAN, Y. Liner impedance determination from piv acoustic measurements. In: **Euronoise 2015**. Maastricht, Netherlands: [s.n.], May 31 – June 3 2015.

[47] HEUWINKEL, C. et al. Characterization of a perforated liner by acoustic and optical measurements. In: **16th AIAA/CEAS**

Aeroacoustics Conference. Stockholm, Sweden: No. AIAA 2010-3765, June 7–9 2010.

[48] MARX, D. et al. Sound amplification in a lined duct with flow: PIV measurements. **The Journal of the Acoustical Society of America**, v. 123, n. 5, p. 3130–3130, 2008.

[49] MARX, D. et al. PIV and LDV evidence of hydrodynamic instability over a liner in a duct with flow. **Journal of Sound and Vibration**, v. 329, n. 18, p. 3798 – 3812, 2010.

[50] MEDEIROS, A. A.; CORDIOLI, J. A. Evaluation of three impedance eduction methods for acoustic liners under grazing flow. In: **Euronoise 2015**. Maastricht, Netherlands: [s.n.], May 31 – June 3 2015.

[51] ÅBOM, M. Measurement of the scattering-matrix of acoustical two-ports. **Mechanical Systems and Signal Processing**, v. 5, n. 2, p. 89 – 104, 1991.

[52] DAI, X.; AURéGAN, Y. Acoustic of a perforated liner with grazing flow: Floquet-bloch periodical approach versus impedance continuous approach. **The Journal of the Acoustical Society of America**, v. 140, n. 3, p. 2047–2055, 2016.

[53] LEVENBERG, K. A method for the solution of certain non-linear problems in least squares. **Quarterly of applied mathematics**, JSTOR, v. 2, n. 2, p. 164–168, 1944.

[54] PRIDMORE-BROWN, D. C. Sound propagation in a fluid flowing through an attenuating duct. **Journal of Fluid Mechanics**, v. 4, p. 393–406, 1958.

[55] KINSLER, L. E.; FREY, A. R. **Fundamentals of Acoustics**. [S.l.]: New York: John Wiley and Sons, 1950.

[56] INGARD, U. On the theory and design of acoustic resonators. **Journal of the Acoustical Society of America**, v. 25, p. 1037–1062, 1953.

[57] MORSE, P. M.; INGARD, K. U. **Theoretical Acoustics**. [S.l.]: New York: McGraw Hill Book Company, 1968.

[58] RICE, E. J. **A Model for the Acoustic Impedance of Perforated Plate Liner with Multiple Frequency Excitation**. [S.l.], 1971.

[59] INGARD, U. Absorption characteristics of non-linear acoustic resonators. **Journal of the Acoustical Society of America**, v. 44, p. 1155–1156, 1968.

[60] FEDER, E.; DEAN, L. W. **Analytical and experimental studies for predicting noise attenuation in acoustically treated ducts for turbofan engines**. [S.l.], 1969.

[61] ELNADY, T. **Modelling and characterization of perforates in lined ducts and mufflers (Paper III)**. Tese (Doutorado) — Department of Aeronautical and Vehicle Enginnering, KTH, Stockholm, Sweden, 2004.

[62] KIRBY, R.; CUMMINGS, A. The impedance of perforated plates subjected to grazing gas flow and backed by porous media. **The Journal of the Acoustical Society of America**, v. 217, n. 4, p. 619–636, 1998.

[63] MEDEIROS, A. A. **On the modelling and characterization of acoustic liners under grazing flow**. Dissertação (Mestrado em Engenharia Mecânica).

[64] RIENSTRA, S. W. Impedance models in time domain, including the extended helmholtz resonator model. In: **12th AIAA/CEAS Aeroacoustics Conference and Exhibit**. Cambridge, Massachusetts: No. AIAA 2006-2686, May 8–10 2006.

[65] ÖZYÖRÜK, Y.; LONG, L. N. A time-domain implementation of surface acoustic impedance condition with and without flow. **Journal of Computational Acoustics**, World Scientific, v. 5, n. 03, p. 277–296, 1997.

[66] LI, X.; LI, X.; TAM, C. K. W. Improved multipole broadband time-domain impedance boundary condition. **AIAA journal**, v. 50, n. 4, p. 980–984, 2012.

[67] ÖZYÖRÜK, Y.; LONG, L. N.; JONES, M. G. Time-domain numerical simulation of a flow-impedance tube. **Journal of Computational Physics**, Elsevier, v. 146, n. 1, p. 29–57, 1998.

[68] RICHTER, C. et al. Comparison of time-domain impedance boundary conditions for lined duct flows. **AIAA journal**, v. 45, n. 6, p. 1333–1345, 2007.

[69] TAM, C. K.; AURIAULT, L. Time-domain impedance boundary conditions for computational aeroacoustics. **AIAA journal**, v. 34, n. 5, p. 917–923, 1996.

[70] REYMEN, Y.; BAELMANS, M.; DESMET, W. Efficient implementation of tam and auriault's time-domain impedance boundary condition. **AIAA journal**, v. 46, n. 9, p. 2368–2376, 2008.

[71] TROIAN, R. et al. Broadband liner impedance eduction for multimodal acoustic propagation in the presence of a mean flow. **Journal of Sound and Vibration**, Elsevier, v. 392, p. 200–216, 2016.

[72] BRAMBLEY, E. J. Fundamental problems with the model of uniform flow over acoustic linings. **Journal of Sound and Vibration**, v. 322, n. 4-5, p. 1026–1037, 2009.

[73] WATSON, W. R.; JONES, M. G. Evaluation of wall boundary conditions for impedance eduction using a dual-source method. In: **18th AIAA/CEAS Aeroacoustics Conference and Exhibit**. Colorado Springs, CO: No. AIAA 2012-2199, June 4–6 2012.

[74] GABARD, G. A comparison of impedance boundary conditions for flow acoustics. **Journal of Sound and Vibration**, v. 332, n. 4, p. 714–724, 2013.

[75] CREMER, L. Theorie der Luftschall-Dämpfung im Rechteckkanal mit schluckender Wand und das sich dabei ergebende höchste Dämpfungsmass. **Acta Acustica united with Acustica**, v. 3, n. 2, p. 249–263, 1953.

[76] TESTER, B. J. The optimization of modal sound attenuation in ducts, in the absence of mean flow. **Journal of Sound and Vibration**, v. 27, n. 4, p. 477–513, 1973.

[77] RIENSTRA, S. W. Fundamentals of duct acoustics. Von Karman Institute Lecture Notes. 2015. Disponível em: <http://www.win.tue.nl/~sjoerdr/papers/VKI_Rienstra.pdf>.

[78] RIENSTRA, S. W. A classification of duct modes based on surface waves. **Wave Motion**, v. 37, n. 2, p. 119–135, 2003.

[79] TESTER, B. J. The propagation and attenuation of sound in lined ducts containing uniform or plug flow. **Journal of Sound and Vibration**, v. 28, n. 2, p. 151–203, 1973.

[80] TYLER, J. M.; SOFRIN, T. G. Axial flow compressor noise studies. In: **SAE Technical Paper**. [S.l.]: SAE International, 1962.

[81] MCALPINE, A.; WRIGHT, M. Acoustic scattering by a spliced turbofan inlet duct liner at supersonic fan speeds. **Journal of Sound and Vibration**, v. 292, n. 3–5, p. 911 – 934, 2006.

[82] KO, S.-H. Sound attenuation in acoustically lined circular ducts in the presence of uniform flow and shear flow. **Journal of Sound and Vibration**, v. 22, n. 2, p. 193–210, 1972.

[83] KO, S.-H. Sound Attenuation in Lined Rectangular Ducts with Flow and Its Application to the Reduction of Aircraft Engine Noise. **The Journal of the Acoustical Society of America**, v. 50, n. 6, 1971.

[84] EVERSMAN, W. Effect of boundary layer on the transmission and attenuation of sound in an acoustically treated circular duct. **The Journal of the Acoustical Society of America**, v. 49, n. 5A, p. 1372–1380, 1971.

[85] MUNGUR, P.; GLADWELL, G. Acoustic wave propagation in a sheared fluid contained in a duct. **Journal of Sound and Vibration**, v. 9, n. 1, p. 28 – 48, 1969.

[86] NAYFEH, A.; KAISER, J.; SHAKER, B. Effect of mean-velocity profile shapes on sound transmission through two-dimensional ducts. **Journal of Sound and Vibration**, v. 34, n. 3, p. 413 – 423, 1974.

APPENDIX A – Derivation of the eigenvalue equation for lined rectangular ducts in the presence of mean flow

This appendix shows how to find the classical eigenvalue equation for lined ducts in the presence of a mean flow. The equation is derived regarding two boundary conditions: (i) Ingard-Myers [28, 29] and (ii) Brambley [31]. The coordinate system follows the reference geometry in Chapter 2.

A.1 Ingard-Myers boundary condition

The Ingard-Myers boundary condition is given by

$$-u = \frac{1}{i\omega Z}\left(\frac{\partial}{\partial t} + U\frac{\partial}{\partial z}\right)p. \tag{A.1}$$

By assuming time dependence of $e^{i\omega t}$,

$$-u = \frac{1}{i\omega Z}\left(i\omega + U\frac{\partial}{\partial z}\right)p. \tag{A.2}$$

The Euler equation normal to the surface at $x = 0$ is given by

$$\rho\left(\frac{\partial}{\partial t} + U\frac{\partial}{\partial z}\right)u = -\frac{\partial p}{\partial x}. \tag{A.3}$$

Once again, by assuming time dependence of $e^{i\omega t}$, the equation is simplified to

$$\rho\left(i\omega + U\frac{\partial}{\partial z}\right)u = -\frac{\partial p}{\partial x}. \tag{A.4}$$

Substituting Equation A.2 into Equation A.4,

$$\frac{\partial p}{\partial x} = \frac{\rho}{i\omega Z}\left(i\omega + U\frac{\partial}{\partial z}\right)^2 p. \tag{A.5}$$

which can also be written as

$$\frac{\partial p}{\partial x} = \frac{Z_0}{ikZ}\left(ik + M\frac{\partial}{\partial z}\right)^2 p. \tag{A.6}$$

where $Z_0 = \rho_0 c_0$ is the characteristic impedance. The acoustic field can be written as a sum of Q modes of amplitude $a^{(q)}$ and mode shape $\psi^{(q)}(x, y)$, given by (considering only right-running modes)

$$p(x, y, z) = \sum_{q=1}^{Q} A^{(q)} \psi^{(q)}(x, y) e^{-ik_z^{(q)} z}. \tag{A.7}$$

By means of the separation of variable, the acoustic pressure of each modes can be written as

$$p^{(q)} = \left(A_m^{(q)} e^{ik_x^{(q)} x} + B_m^{(q)} e^{-ik_x^{(q)} x} \right) \left(A_n^{(q)} e^{ik_y^{(q)} y} + B_n^{(q)} e^{-ik_y^{(q)} y} \right) e^{-ik_z^{(q)} z}, \tag{A.8}$$

where $A_m^{(q)}$, $A_n^{(q)}$, $B_m^{(q)}$ and $B_n^{(q)}$ are arbitrary constants determined by the boundary conditions. In the following the mode index (q) is omitted. The spatial derivative in x is

$$\begin{aligned} \frac{\partial p}{\partial x} &= \left(ik_x A_m e^{ik_x x} - ik_x B_m e^{-ik_x x} \right) \left(A_n e^{ik_y y} + B_n e^{-ik_y y} \right) e^{-ik_z z} \\ &= ik_x \frac{A_m e^{ik_x x} - B_m e^{-ik_x x}}{A_m e^{ik_x x} + B_m e^{-ik_x x}} p, \end{aligned} \tag{A.9}$$

and the spatial derivative in z,

$$\begin{aligned} \frac{\partial p}{\partial z} &= -ik_z \left(A_m e^{ik_x x} + B_m e^{-ik_x x} \right) \left(A_n e^{ik_y y} + B_n e^{-ik_y y} \right) e^{-ik_z z} \\ &= -ik_z p. \end{aligned} \tag{A.10}$$

Substituting back into Equation A.6,

$$ik_x \frac{A_m e^{ik_x x} - B_m e^{-ik_x x}}{A_m e^{ik_x x} + B_m e^{-ik_x x}} \not{p} = \frac{Z_0}{ikZ} \left(ik - iMk_z \right)^2 \not{p} \tag{A.11}$$

Since this equation is evaluated at $x = 0$,

$$ik_x \frac{A_m - B_m}{A_m + B_m} = \frac{Z_0}{ikZ} \left(ik - iMk_z \right)^2 \tag{A.12}$$

The arbitrary constants still have to be determined from a second boundary condition. The hard wall condition at $x = b$ gives

$$\left.\frac{\partial p}{\partial x}\right|_{x=b} = 0, \tag{A.13}$$

and thus

$$B_m = A_m e^{2ik_x b}, \tag{A.14}$$

which results in

$$\begin{aligned}\frac{Z_0}{ikZ}\left(ik - iMk_z\right)^2 &= ik_x \frac{\cancel{A_m}\left(1 - e^{2ik_x b}\right)}{\cancel{A_m}\left(1 + e^{2ik_x b}\right)} \\ &= ik_x \frac{\left(e^{-ik_x b} - e^{ik_x b}\right)\cancel{e^{ik_x b}}}{\left(e^{ik_x b} + e^{-ik_x b}\right)\cancel{e^{ik_x b}}}.\end{aligned} \tag{A.15}$$

Since the following property is known,

$$\tan\left(x\right) = \frac{i\left(e^{-ix} - e^{ix}\right)}{e^{ix} + e^{-ix}}, \tag{A.16}$$

the classical eigenvalue equation which relates the axial and transverse wave numbers k_z and k_x, respectively, for a given normalized wall impedance Z and flow velocity M is

$$\boxed{k_x \tan\left(k_x b\right) = \frac{i}{kZ}\left(k - Mk_z\right)^2} \tag{A.17}$$

A.2 Brambley boundary condition

The Brambley boundary condition [31] is given by

$$-u\left[Z - \frac{i}{k}\left(k - Mk_z\right)^2 \delta I_0\right] = \left[\frac{k - Mk_z}{k} - \frac{Z\delta I_1 k_z^2}{i\left(k - Mk_z\right)}\right] p \tag{A.18}$$

where the coefficients δI_0 and δI_1 are defined as

$$\delta I_0 = \int_0^\delta 1 - \frac{\left(k - M(x)k_z\right)^2}{\left(k - Mk_z\right)^2} dx \tag{A.19}$$

$$\delta I_1 = \int_0^\delta 1 - \frac{\left(k - Mk_z\right)^2}{\left(k - M(x)k_z\right)^2} dx \tag{A.20}$$

Notice that, in this case, Z is the normalized impedance. Introducing into the normalized Euler equation

$$\left(ik + M\frac{\partial}{\partial z}\right)u = -\frac{\partial p}{\partial x} \tag{A.21}$$

results into

$$\frac{\partial p}{\partial x} = p\left(ik - iMk_z\right)\frac{\dfrac{k - Mk_z}{k} - \dfrac{Z\delta I_1 k_z^2}{i\left(k - Mk_z\right)}}{Z - \dfrac{i}{k}\left(k - Mk_z\right)^2\delta I_0} \tag{A.22}$$

After some manipulation,

$$\frac{\partial p}{\partial x} = p\left[\frac{i(k - Mk_z)^2 - kZ\delta I_1 k_z^2}{kZ - i(k - Mk_z)^2\delta I_0}\right] \tag{A.23}$$

As previously shown, the spatial derivative in x is given by

$$\frac{\partial p}{\partial x} = ik_x\frac{A_m e^{ik_x x} - B_m e^{-ik_x x}}{A_m e^{ik_x x} + B_m e^{-ik_x x}}p, \tag{A.24}$$

thus

$$ik_x\frac{A_m e^{ik_x x} - B_m e^{-ik_x x}}{A_m e^{ik_x x} + B_m e^{-ik_x x}} = \frac{i(k - Mk_z)^2 - kZ\delta I_1 k_z^2}{kZ - i\left(k - Mk_z\right)^2\delta I_0} \tag{A.25}$$

Repeating the same procedure from Ingard-Myers boundary condition, the following relation may be derived

$$\boxed{k_x\tan\left(k_x b\right) = \frac{i\left(k - Mk_z\right)^2 - kZ\delta I_1 k_z^2}{kZ - i\left(k - Mk_z\right)^2\delta I_0},} \tag{A.26}$$

Notice that, if $\delta = 0$, then $\delta I_0 = \delta I_1 = 0$ and the Ingard-Myers boundary condition is recovered.

APPENDIX B – Derivation of the expressions for optimal impedance in circular ducts

In this appendix, the expressions for optimum impedance in circular ducts in the absence and presence of mean flow are shown. The no-flow case can be seen as an special case of the expression with mean flow and is first introduced. The following recurrence relations for Bessel functions of the first kind are employed:

$$2J'_m(x) = J_{m-1}(x) - J_{m+1}(x) \tag{B.1}$$

and

$$2\frac{m}{x}J_m(x) = J_{m-1}(x) + J_{m+1}(x). \tag{B.2}$$

B.1 In the absence of mean flow

In a circular duct with a locally reacting wall impedance $Z(\omega)$, the wave numbers are eigenvalues of the equation

$$\frac{J_m(\alpha)}{\alpha J'_m(\alpha)} = \frac{iZ}{\varpi}. \tag{B.3}$$

By following the definition of Cremer's optimum impedance [75], the derivative to α must vanish, which yields

$$\frac{d}{d\alpha}\left(\frac{J_m(\alpha)}{\alpha J'_m(\alpha)}\right) = 0, \tag{B.4}$$

so that

$$\frac{d}{d\alpha}\left(\frac{J_m(\alpha)}{\alpha J'_m(\alpha)}\right) = \frac{\left[J'_m(\alpha)\alpha J'_m(\alpha)\right] - J_m(\alpha)\left[\alpha J'_m(\alpha)\right]'}{\left[\alpha J'_m(\alpha)\right]^2} \tag{B.5}$$

$$= \frac{\alpha J'_m(\alpha)^2 - J_m(\alpha)\left[\alpha J''_m(\alpha) + J'_m(\alpha)\right]}{\left[\alpha J'_m(\alpha)\right]^2} \tag{B.6}$$

$$= \frac{\alpha J'_m(\alpha)^2 - \alpha J_m(\alpha)J''_m(\alpha) - J_m(\alpha)J'_m(\alpha)}{\left[\alpha J'_m(\alpha)\right]^2} \tag{B.7}$$

The second derivative of the Bessel function can be written as (based on Equation B.1)

$$2J''_m(\alpha) = J'_{m-1}(\alpha) - J'_{m+1}(\alpha), \tag{B.8}$$

and therefore

$$\frac{\alpha J'_m(\alpha)^2 + Q}{\left[\alpha J'_m(\alpha)\right]^2} = 0, \tag{B.9}$$

where Q is an auxiliary variable,

$$Q = -\alpha J_m(\alpha)\left[\frac{J'_{m-1}(\alpha) - J'_{m+1}(\alpha)}{2}\right] - J_m(\alpha)J'_m(\alpha). \tag{B.10}$$

For now only Q will be further simplified. Hence,

$$\begin{aligned} Q = -\frac{\alpha J_m(\alpha)}{2}&\left[\frac{J_{m-2}(\alpha) - J_m(\alpha) - J_m(\alpha) + J_{m+2}(\alpha)}{2}\right] \\ &- J_m(\alpha)\left[\frac{J_{m-1}(\alpha) - J_{m+1}(\alpha)}{2}\right]. \end{aligned} \tag{B.11}$$

In order to group the Bessel functions into the same order, Equation B.2 is used, for instance,

$$J_{m-2}(\alpha) = 2\frac{m-1}{\alpha}J_{m-1}(\alpha) - J_m(\alpha), \tag{B.12}$$

$$J_{m+2}(\alpha) = 2\frac{m+1}{\alpha}J_{m+1}(\alpha) - J_m(\alpha). \tag{B.13}$$

Thus,

$$\begin{aligned} Q = -\frac{\alpha J_m(\alpha)}{4}&\left[2\frac{m-1}{\alpha}J_{m-1}(\alpha) - 4J_m(\alpha) + 2\frac{m+1}{\alpha}J_{m+1}(\alpha)\right] \\ &+ \frac{1}{2}J_m(\alpha)\left[J_{m+1}(\alpha) - J_{m-1}(\alpha)\right]. \end{aligned} \tag{B.14}$$

$$\begin{aligned} Q = -\frac{\alpha J_m(\alpha)}{4}&\left[\frac{2m}{\alpha}\left[J_{m-1}(\alpha) + J_{m+1}(\alpha)\right] + \frac{2}{\alpha}\left[J_{m+1}(\alpha) - J_{m-1}(\alpha)\right]\right] \\ &+ \alpha J_m(\alpha)^2 + \frac{1}{2}J_m(\alpha)\left[J_{m+1}(\alpha) - J_{m-1}(\alpha)\right]. \end{aligned} \tag{B.15}$$

By using Equation B.2 again, this expression is further simplified to

$$\begin{aligned} Q = -\frac{\alpha J_m(\alpha)}{4}\left[\frac{2m}{\alpha}\frac{2m}{\alpha}J_m(\alpha) + \frac{2}{\alpha}\left[J_{m+1}(\alpha) - J_{m-1}(\alpha)\right]\right] \\ + \alpha J_m(\alpha)^2 + \frac{1}{2}J_m(\alpha)\left[J_{m+1}(\alpha) - J_{m-1}(\alpha)\right], \end{aligned} \tag{B.16}$$

which yields

$$\begin{aligned} Q = -\alpha\frac{m^2}{\alpha^2}J_m(\alpha)^2 - \frac{1}{2}J_m(\alpha)\left[J_{m+1}(\alpha) - J_{m-1}(\alpha)\right] \\ + \alpha J_m(\alpha)^2 + \frac{1}{2}J_m(\alpha)\left[J_{m+1}(\alpha) - J_{m-1}(\alpha)\right], \end{aligned} \tag{B.17}$$

and finally

$$Q = -\alpha\frac{m^2}{\alpha^2}J_m(\alpha)^2 + \alpha J_m(\alpha)^2 \tag{B.18}$$

Back into Equation B.9,

$$\frac{\alpha J'_m(\alpha)^2 - \alpha\frac{m^2}{\alpha^2}J_m(\alpha)^2 + \alpha J_m(\alpha)^2}{\left[\alpha J'_m(\alpha)\right]^2} = 0, \tag{B.19}$$

$$\frac{\alpha}{\left[\alpha J'_m(\alpha)\right]^2}\left[J'_m(\alpha)^2 - \frac{m^2}{\alpha^2}J_m(\alpha)^2 + J_m(\alpha)^2\right] = 0. \tag{B.20}$$

The nontrivial solutions are given by the right term, which can be rewritten as

$$\boxed{J'_m(\alpha)^2 + \left(1 - \frac{m^2}{\alpha^2}\right)J_m(\alpha)^2 = 0.} \tag{B.21}$$

Equation B.21 can be solved for each m and admits multiple solutions (although we are usually interested on the first modes). The *fsolve* Matlab routine is employed to solve the aforementioned equation using the hard-wall values i.e. α_{mn} which is solution to $J'_m(\alpha_{mn}) = 0$, as initial guesses. The optimum impedance is found by substituting α back into Equation B.3, i.e.

$$\boxed{Z_{\text{opt}}^{(mn)} = -i\varpi\frac{J_m(\alpha_{mn})}{\alpha_{mn}J'_m(\alpha_{mn})}} \tag{B.22}$$

B.2 In the presence of mean flow

In the presence of mean flow, the eigenvalue problem is given by

$$(1 - M\varphi)^2 J_m(\alpha) = iZ\beta^3 \gamma J'_m(\alpha), \tag{B.23}$$

where the Lorentz or Prandtl-Glauert type transformation was introduced (mode orders are omitted),

$$\beta = \sqrt{1 - M^2}, \tag{B.24}$$

$$\Omega = \frac{\varpi}{\beta}, \tag{B.25}$$

$$\gamma = \alpha \frac{\beta}{\varpi}, \tag{B.26}$$

$$\varphi^{\pm} = \pm\sqrt{1 - \gamma^2}, \tag{B.27}$$

where + indicates right-running modes and − indicates left-running modes. φ is called the reduced axial wave number [78]. Equation B.27 plays an important role, and the sign choice is made such that $\forall\gamma \in \mathbb{C} : \Im(\varphi) < 0$. Therefore, Equation B.27 can be rewritten with help of the sign function, such that

$$\varphi^{\pm}(\gamma) = \pm\left[\operatorname{sgn}\left(\Im\left(\sqrt{1-\gamma^2}\right)\right)\sqrt{1-\gamma^2}\right]. \tag{B.28}$$

Back to Equation B.23, it can be rearranged into

$$(1 - M\varphi)^2 \frac{J_m(\alpha)}{\alpha J'_m(\alpha)} = \frac{iZ\beta^4}{\varpi} \tag{B.29}$$

Once again, the derivative to α must vanish, so that

$$\frac{d}{d\alpha}\left[(1 - M\varphi)^2 \frac{J_m(\alpha)}{\alpha J'_m(\alpha)}\right] = 0. \tag{B.30}$$

Since φ is also function of α, this expressions results in

$$\begin{aligned}\frac{d}{d\alpha}\left[(1 - M\varphi)^2 \frac{J_m(\alpha)}{\alpha J'_m(\alpha)}\right] = {} & \frac{J_m(\alpha)}{\alpha J'_m(\alpha)} \frac{d}{d\alpha}\left[(1 - M\varphi)^2\right] \\ & + (1 - M\varphi)^2 \frac{d}{d\alpha}\left[\frac{J_m(\alpha)}{\alpha J'_m(\alpha)}\right].\end{aligned} \tag{B.31}$$

The last derivative is the same from the previous section,

$$\frac{d}{d\alpha}\left[\frac{J_m(\alpha)}{\alpha J'_m(\alpha)}\right] = \frac{\alpha}{\left[\alpha J'_m(\alpha)\right]^2}\left[J'_m(\alpha)^2 + \left(1 - \frac{m^2}{\alpha^2}\right) J_m(\alpha)^2\right]. \quad \text{(B.32)}$$

The first derivative in Equation B.31 results into

$$\frac{d}{d\alpha}\left[(1 - M\varphi)^2\right] = 2(1 - M\varphi)\frac{d}{d\alpha}(1 - M\varphi) \quad \text{(B.33)}$$

$$= 2(1 - M\varphi)\left(-M\frac{d\varphi}{d\alpha}\right) \quad \text{(B.34)}$$

We can derive φ as follow:

$$\varphi(\alpha) = \sqrt{1 - \gamma^2} \quad \text{(B.35)}$$

$$= \left(1 - \frac{\alpha^2\beta^2}{\varpi^2}\right)^{1/2}, \quad \text{(B.36)}$$

so that

$$\frac{d\varphi}{d\alpha} = \frac{1}{2}\left(1 - \frac{\alpha^2\beta^2}{\varpi^2}\right)^{-1/2}\left(-\frac{2\alpha\beta^2}{\varpi^2}\right) \quad \text{(B.37)}$$

$$= -\frac{\alpha}{\varphi\Omega^2}. \quad \text{(B.38)}$$

Substituting Equation B.38 and Equation B.32 into Equation B.31,

$$\begin{aligned}\frac{d}{d\alpha}\left[(1 - M\varphi)^2\frac{J_m(\alpha)}{\alpha J'_m(\alpha)}\right] &= \frac{J_m(\alpha)}{\alpha J'_m(\alpha)}2M(1 - M\varphi)\frac{\alpha}{\varphi\Omega^2} \\ &+(1 - M\varphi)^2\frac{\alpha}{\left[\alpha J'_m(\alpha)\right]^2}\left[J'_m(\alpha)^2 + \left(1 - \frac{m^2}{\alpha^2}\right) J_m(\alpha)^2\right],\end{aligned} \quad \text{(B.39)}$$

and by making further simplifications,

$$\boxed{\frac{2M}{\varphi\Omega^2}\frac{J_m(\alpha)}{J'_m(\alpha)} + \frac{(1 - M\varphi)}{\alpha J'_m(\alpha)^2}\left[J'_m(\alpha)^2 + \left(1 - \frac{m^2}{\alpha^2}\right) J_m(\alpha)^2\right] = 0.} \quad \text{(B.40)}$$

If $M = 0$, Equation B.21 is recovered. Differently from the no-flow case, the solution depends not only on the Mach number M, but also on the frequency ω. Therefore, it is not possible to solve only for given values of m, and make use of a frequency-free constant $K^{(mn)}$ (a list

such as Table 5.1 is not possible). Equation B.40 can be solved by means of the `fsolve` function in Matlab in the same way as the no-flow case, using the value of $\alpha^{(mn)}$ for the no-flow case as an initial guess. Substituting the solution of Equation B.40 into Equation B.23, the optimum impedance in the presence of flow is given by

$$\boxed{Z_{\text{opt}}^{(mn)} = \frac{(1 - M\varphi)^2 J_m(\alpha)}{i\beta^3 \gamma J'_m(\alpha)}.} \tag{B.41}$$